



HAL
open science

Application of the concept of Parity-Time symmetry to integrated optics

Vincent Brac de La Perrière Brac de La Perrière

► To cite this version:

Vincent Brac de La Perrière Brac de La Perrière. Application of the concept of Parity-Time symmetry to integrated optics. Optics / Photonic. Université Paris Saclay (COMUE), 2019. English. NNT : 2019SACLS010 . tel-02090550

HAL Id: tel-02090550

<https://theses.hal.science/tel-02090550>

Submitted on 4 Apr 2019

HAL is a multi-disciplinary open access archive for the deposit and dissemination of scientific research documents, whether they are published or not. The documents may come from teaching and research institutions in France or abroad, or from public or private research centers.

L'archive ouverte pluridisciplinaire **HAL**, est destinée au dépôt et à la diffusion de documents scientifiques de niveau recherche, publiés ou non, émanant des établissements d'enseignement et de recherche français ou étrangers, des laboratoires publics ou privés.

Application du concept de symétrie Parité-Temps à l'optique intégrée

Thèse de doctorat de l'Université Paris-Saclay
préparée à l'Université Paris Sud



École doctorale n°572 Onde et Matière (EDOM)
Spécialité de doctorat: optique et photonique

Thèse présentée et soutenue à Palaiseau, le 18/02/2019, par

Vincent Brac de la Perrière

Composition du Jury :

Guillaume Huyet DR CNRS, Institut de Physique de Nice (UMR7010)	Président
Olivier Gauthier-Lafaye DR CNRS, Université de Toulouse, LAAS (UPR8001), Yann Boucher	Rapporteur
DR, ENIB, Laboratoire FOTON (UMR 6082) Arianna Filoramo	Rapporteur
CEA, DRF/IRAMIS//NIMBE/LICSEN Anatole Lupu	Examinatrice
DR CNRS, Université Paris Sud, C2N Abderrahim Ramdane	Directeur de thèse
DR CNRS, Université Paris Sud, C2N Henri Benisty	Co-Directeur de thèse
Prof. Institut d'Optique Graduate School	Invité

Acknowledgments

This PhD thesis is the result of three years of research at the Centre de Nanosciences et Nanotechnologies (C2N) now located at on the Paris-Saclay campus. This work could not have succeeded without the support of the people who have shared this experience with me. I would like to thank Anatole Lupu and Abderrahim Ramdane who assumed the direction of this thesis. The complementarity of their skills and their availability throughout this entire work have been crucial in this endeavor. I am very thankful to them for the autonomy and trust they shared with me.

Thank you to Kamel Mergem and Guy Aubin for their precious help, their tremendous knowledge in telecom photonics has been very much valuable.

I would like to thank F. Raineri, S. Guilet, C. Ulysse, C. Dupuis and A. Durnez for being good teachers and sharing their skill or technological achievements. The academic research can only go forward if we co-operate which they are always eager to do.

The C2N clean room staff must be thanked for the great work they do in developing process, know-how and technological skills as well as maintaining the clean room up and running. The experimental realizations presented in this manuscript were only possible because of the level of expertise they represent.

I would like to address special thanks to Quentin Gaimard (AKA "El Rosso") for his help and support. Thank you to all the Ph.D. students of the lab (the list is long) for the joy they brought to this journey.

Je tiens à remercier l'ensemble de la "MISS", doctorants et chercheurs, et plus particulièrement Valérie Fortuna et Elisabeth Delbecq pour leur encadrement. Je fais le rêve qu'un jour tous les élèves puissent avoir accès à de tels enseignements, et sortir de leur classe pour découvrir qu'ils peuvent apprendre par eux-même, et acquérir les outils pour développer leur propre conscience.

Merci à tous mes amis qui m'ont soutenu durant ces trois années. Je mesure la chance que j'ai de les avoir à mes côtés, et j'espère leur rendre ne serait-ce que le quart de ce qu'ils m'apportent.

Merci à ma famille, soutien infaillible, à mes soeurs Louise et Clémence et particulièrement, et à mes parents qui ont élevé 3 docteurs. Leur amour, leurs valeurs et leur éducation font notre fierté, puissions-nous être la leur en retour.

Et enfin merci à Laetitia pour toutes ces années, pour tous ces rires et ces aventures qui m'ont fait oublier le tumulte de Paris et l'exigence de la thèse.

Contents

Contents	i
Introduction	1
1 Distributed Feedback Lasers and Parity Time Symmetry	5
1.1 DFB Lasers in Telecommunication Optics	7
1.1.1 Coupled wave theory	8
1.2 Parity Time Symmetry in Optics	10
1.2.1 From Non Hermitian Hamiltonians to PTS Optics	11
1.2.2 Exceptional Point	12
1.2.3 PT symmetric Bragg grating	12
1.3 Objectives of this work	13
1.4 Références	15
2 Implementation of PT-symmetry in practical devices	19
2.1 Simulation of Bragg reflectors using Abelès formulation	21
2.2 Modal behavior inside DFB laser structures	21
2.2.1 Case of a conventional 3rd order index-coupled DFB laser	22
2.2.2 Effect of facet phase on IC DFB lasers emission characteristics	25
2.2.3 Case of a conventional gain-coupled DFB laser	26
2.2.4 Effect of facet phase on GC DFB lasers emission characteristics	27
2.2.5 Case of complex-coupled DFB laser	28
2.2.6 Asymmetric response of DFB lasers and effects of facet reflections	30
2.2.7 Conclusion and objectives of this work	33
2.3 Design of a Parity-Time Symmetric coupler	34
2.3.1 Impact of the detuning due to fabrication constrains	34
2.3.2 Grating assisted directional coupler	37
2.4 Conclusion on the design of PTS GADC	39
2.5 Références	40
3 Design And Fabrication	43
3.1 Design of PTS DFB laser	45
3.1.1 Technical Choices	45
3.1.2 Simulation and Design	46
3.1.3 Sample layout	48
3.2 Fabrication of a PTS DFB laser	49
3.2.1 Electron beam lithography	51
3.2.2 ICP etching development	52
ICP etching mechanisms	52
Role of chemical species	53

ICP Parameters	54
3.2.3 Etching of InP corrugated grating	54
3.2.4 Development of the ICP etching process	56
Cl ₂ /Ar plasma	56
Cl ₂ :H ₂ :O ₂ plasma	57
Cl ₂ H ₂ :O ₂ :He plasma	59
HBr:O ₂ :He plasma	61
3.2.5 Etching of the index grating	63
3.2.6 Fabrication of the metallic grating, and back-end	64
3.3 Conclusions	66
3.4 Références	67
4 Investigation on Distributed Feedback lasers: performance and comparison	71
4.1 Sample layout	73
4.2 Light current characteristic	74
4.2.1 Performances of the Fabry-Perot	74
4.2.2 Overview	76
4.2.3 Performances of the complex-coupled DFB lasers	77
4.2.4 Conclusion on the emission power	80
4.3 Spectral Performance and Evolution	80
4.3.1 Comparison of the Conventional DFB Lasers	81
Index-Coupled DFB lasers	81
Gain-Coupled DFB lasers	82
4.3.2 Spectrum comparison of the CC DFB Lasers	84
4.3.3 Conclusion on the spectral performances	87
4.4 Conclusion	87
5 In-depth characterization of Complex-Coupled DFB lasers	89
5.1 Transmission and reflection response of the lasers	91
5.2 Evaluation of the laser losses characteristics	92
5.2.1 Principle	93
5.2.2 Distribution of losses from grating types	93
5.2.3 Index modulation amplitudes	94
Real part modulation	94
Imaginary part modulation	95
5.2.4 Evaluation of the coupling constant of index-coupled DFB lasers	96
5.2.5 Expression of non-reciprocal effects	97
5.3 Conclusion on external probing of DFB lasers	99
5.4 Effect of external feedback on semiconductor lasers	100
5.4.1 Modeling of laser emission under external optical feedback	100
5.4.2 Regimes of external feedback for long external cavities	100
5.4.3 Coherence collapse	101
5.4.4 Requirements for isolator-free operation	102
5.5 Experimental study of DFB lasers operation under external feedback	103
5.5.1 Experimental setup and configuration	103
5.5.2 Results and discussion	104
Index-Coupled DFB lasers	104
Gain-Coupled DFB lasers	104
Complex-Coupled DFB lasers	105
5.6 Conclusion on the resistance to external feedback	110

5.7 Conclusion of the chapter	111
5.8 Références	113
Conclusions and perspectives	117
A Abeles Matric model for the simulation of modes inside the laser cavity	121
A.1 Abeles Matrix Formalism	121
A.1.1 Application of Abeles matrix method to PT-symmetric structure . . .	123
A.1.2 Simulation of plane waves propagation through PT-symmetric stack of layers	125
B Emission characteristics of lasers operating at 1.55μm and 1.53μm	129
C Résumé long en français	133

Introduction

Controlling the electric permittivity along with the magnetic permeability has long been a major field of research in optics, especially in a magnetic perspective. With the design of artificial photonic materials, the precise control of the material parameters has led to the emergence of new functionalities in integrated optical devices. This class of application is very attractive for the use of artificial textured materials because of the several simultaneous constraints it embodies. Photonic crystals and metamaterials represent the best known examples of the tailoring of respectively the electric permittivity and the magnetic permeability, inducing exotic magnetic responses such as negative refractive index, negative permeability, photonic band-gap and zero refractive index.

However, in practice the design and engineering of optical systems usually rely on the tailoring of not only the refractive index but also the amount of gain or losses. In particular, the amount of losses has long been considered to only cause degraded performances of optical systems, and its use as a genuine tool in wave propagation remained unconsidered until recently. Currently, a novel trend in modern optics consisting in the engineering of losses, balanced with gain and refractive index manipulation is receiving considerable attention from the photonics research community. This topic, originating from the so called Parity-Time Symmetry (PT-symmetry) inspired from the recent work of Bender et al. in 1998 on the hermiticity of Hamiltonians, was found to be of great interest in several compartments of optics for the observation of intriguing light behavior. The transposition of PT-symmetry from quantum mechanics to optics based on the equivalence between Schrödinger equation and the classical wave equation in coupled systems, revealed the potential interest of losses as an additional tool for the expression of exotic and intriguing functionalities in photonic circuits, such as unidirectional light transport, coherent perfect absorption, or phase transition point to name but a few.

Despite the great interest brought by PT-symmetry and the potential tool it represents in the design of photonic devices, its development remained confined to well equipped optical laboratories with, to my knowledge, no full spread of any "killer" application.

In the meantime, the boom of optical telecommunications, brought by the growth of the internet traffic, Internet Of Things (IoT) or cloud data storage and computing, increased the need for efficient and robust coherent light sources to work as transmitter for optical fiber networks. Semiconductor lasers directly or externally modulated, the workhorse of the development of optical networks, quickly became subject of technological challenges, with the objective to improve their static and dynamic performances, in order to increase the data rate through the bandwidth. Distributed FeedBack (DFB) lasers are probably the best example of technological achievement resulting from the arrangement of material properties to pursue this avenue. Owing to their low cost, single-frequency operation, low power consumption and monolithic integration in photonic integrated circuits (PICs), DFB lasers have become a world standard equipment for data transmission in all communication networks.

This work represents a first attempt to apply the concept of PT-symmetry to practical devices, in particular to the design and fabrication of a laser-modulator system, and was carried out at the Centre de Nanosciences et Nanotechnologies (C2N) newly relocated in Palaiseau, France.

The main part of the work involved the design, fabrication and characterization of complex-coupled DFB lasers, and the investigation of potential expression of PT-symmetry effects arising from the specific association of a loss grating and an index grating. Conventional DFB lasers used in optical networks nowadays exploit either gain-coupling or index-coupling mechanisms, respectively involving a grating carrying a modulation of the material gain (loss) or of the material index of refraction, when complex-coupling mechanism involve both.

Investigations on the emission output power, spectrum, transmission characteristics and feedback resistance are discussed through this manuscript. A particular interest is brought to the study of the fabricated lasers performances depending on the nominal phase shift existing between the loss and index gratings, in order to discuss the advantages of combining gain and index coupling gratings, and witness asymmetric characteristics of the laser emission: indication of the potential expression of PT-symmetry.

The principal interest of applying the concept of PT-symmetry to DFB lasers, is to take advantages of the asymmetric coupling brought by such grating. Indeed, by implementing a PT-symmetric Bragg grating within the laser cavity, the coupled contra-propagative waves should be impacted by different coupling constant, one experiencing gain while the other experiences loss. This feature can be of great interest for the operation of DFB as the coupling of external reflections, harmful for the laser operation, could be attenuated inside the cavity, and hence one could avoid in particular loss of coherence.

The first chapter is an introduction to the working principle of DFB lasers technology together with the concept of Parity-Time symmetry. The comparison between classical and PT-symmetric Bragg grating is made and the objectives of this work are presented.

The second chapter presents the simulation principle and results, helping on the understanding of mode dynamics inside a DFB laser. The case of index, gain and complex-coupling mechanism is presented to provide an insight of the interaction of the real and imaginary parts of the material index with the existing modes inside the cavity. The second part of this chapter is dedicated to the proposal of a grating assisted PT-symmetric coupler, in response to the lack of technological tolerances allowed by the ideal PT-symmetric coupler case.

Chapter three reports the design, fabrication process and tools developed for the elaboration of complex-coupled DFB lasers. The particular development of ICP etching processes for the critical definition of dielectric grating is discussed.

The fourth chapter presents the emission characteristics of the fabricated lasers in terms of output power and spectrum. The single-frequency operation and its stability over a wide range of current is discussed, to compare the efficiency of the mode filtering inside the laser cavity. Emphasis is put on the investigation of the emission characteristics of the complex-coupled DFB laser depending on the nominal phase shift between dielectric and metallic gratings.

Chapter five presents the probing of the fabricated laser cavities by an external tunable laser. From this experiment, the cavity losses are measured and Bragg grating response

is investigated under sub-threshold injection current. The second part of this chapter relates the resistance of the fabricated lasers to external optical feedback, and a comparison is made based on the nominal phase shift between grating types.

Chapter 1

Distributed Feedback Lasers and Parity Time Symmetry

For very long distances, such as transatlantic networks, monochromatic sources are a great asset as the signal is altered all along its propagation, and optical sources require a pure single-frequency and narrow linewidth spectrum.

From the first pioneering work by Kogelnik and Shank in the early 70's [2, 3], DFB Lasers have found countless applications particularly in the realm of wavelength division multiplexed optical telecommunication systems (in the 1990s). The single frequency generation is achieved inside DFB lasers through the implementation of a Bragg grating, creating condition of a photonic band gap. Mode selectivity is then more efficient than in conventional Fabry-Perot cavities, where mode selectivity only results from interferences induced by the facet reflectivity.

The Bragg grating can be implemented either by a modulation of the refractive index of the laser, or by a modulation of the optical gain in the active region, or both. Hereafter, DFB lasers with only index modulation will be referred to as *index-coupled DFB lasers*, DFB lasers with only gain modulation will be referred to as *gain-coupled DFB lasers* and DFB lasers using both index and gain modulations will be referred to as *complex-coupled DFB lasers*.

The Bragg grating inside the laser cavity works as a wavelength-selective device to achieve stable narrow-linewidth laser operation. The interference pattern appearing from the grating will affect the modes traveling inside the cavity, and will work constructively for wavelength λ_B satisfying the following condition:

$$\Lambda = m \frac{\lambda_B}{2n_{eff}} \quad (1.1)$$

Where Λ is the grating period, n_{eff} the material effective index, and λ_B the Bragg wavelength. The photons that satisfy the Bragg condition will interact constructively, and therefore have a increased lifetime between each index interface. The population of photons in that mode growing, the stimulated emission rate will increase and enable the attenuation of Fabry-Pérot side modes because of its high radiative recombination efficiency.

1.1.1 Coupled wave theory

In the late 60's, Kogelnik and Shank proposed a coupled mode theory model to describe the interactions between propagating modes, and diffraction inside volume holograms[4]. They later found that this model could be used to describe the mode selection and mode dynamics in semiconductor lasers, and to define the characteristics required for a DFB to reach single mode operation [2, 3].

As previously stated, DFB lasers are characterized by their longitudinal periodic variation of the refractive index $n(z)$ and/or gain $g(z)$, within the laser medium. The index/gain perturbation is often written using the following formulation:

$$\begin{aligned} n(z) &= n_{eff} + n_1 \cos\left(\frac{2\pi}{\Lambda}(z - z_0)\right) \\ g(z) &= g + g_1 \cos\left(\frac{2\pi}{\Lambda}(z - z'_0)\right) \end{aligned} \quad (1.2)$$

It encapsulates the fact that the wave is guided in a given transverse mode (quasi-TE0 for instance) through the effective index, the phase index of the guided mode of an average translation-invariant structure along the diode axis, $\beta_0 = n\omega_0/c$.

$$\begin{aligned} R &= r_1 \exp(\Gamma z) + r_2 \exp(-\Gamma z) \\ S &= s_1 \exp(\Gamma z) + s_2 \exp(-\Gamma z) \end{aligned} \quad (1.8)$$

The complex propagation constant Γ is defined by the dispersion relation:

$$\Gamma^2 = \kappa^2 + j(\beta - \beta_B) \quad (1.9)$$

Where r_1, r_2, s_1 and s_2 can be determined from boundary conditions.

κ is here a key parameter, as it represents the coupling between S and R. The efficiency of the grating through its selectivity and strength, will be dependent on this parameter. Though κ is essential, as it drives the behavior of the DFB lasers, it can be difficult to compute it analytically when the transverse mode profiles are somehow convolved, or measure it experimentally. Indeed, its practical value will be fully determined from the local variation of the index and/or gain but also from the mode confinement, as the interaction from the mode and the grating will highly depend on this confinement.

As DFB lasers have brought much interest in the realm of photonics over the past 30 years, a lot of coupled mode analysis development can be found in the literature on this topic. Most of the theoretical and experimental work has been confined to the case of a modulation of either real or imaginary parts of the index (with some exceptions in the 90s), trying to understand and tailor the wavelength selectivity of the cavity grating. However, it became clear that the realization of an index grating would eventually impact the loss profile of the material, as well as a lossy grating would in return impact its index profile. The study of a complex-coupled grating thus became of great interest, but only with the specific case of in phase gain and index modulations[5, 6]. Complex-coupled gratings with variable grating phase then attracted attention of researchers [7, 8, 9, 10], as it could be considered as an additional tool to improve the performances of the spectral filtering inside the laser cavity. Interestingly, conclusions found on the effects of relative phase between index parts modulations mention non reciprocal propagation through the phase shifted gratings, representing a precursor outlook of a Parity-Time symmetric effect in photonics. With the later emergence of the concept of Parity-Time symmetry in optics, the peculiar case of a quarter phase shift between real and imaginary components of the material index became the object of intense investigations, as will be seen in the following section.

1.2 Parity Time Symmetry in Optics

With the substantial progress of lithography and other nanofabrication techniques over the past decades, the design and fabrication of nanostructures has become a strategic work field, with the miniaturization that we can witness nowadays. In photonics, thanks to judicious arrangement of structures and material combinations, a dream of the metamaterial vision became reality in the last decade, and now, all four quadrants of electromagnetic real valued responses (ϵ, μ) can be achieved. With the implementation of photonic crystals and metamaterials, a large array of exotic electromagnetic responses emerged, such as negative refractive index or negative magnetic permeability.

The work on the imaginary part of the index, however, has long remained a deserted field of research. If the avoidance of loss inside optical materials is highly desirable, Parity-Time symmetry demonstrated that losses could be considered as a powerful asset to bring tunability and exotic functions to integrated optical devices.

1.2.1 From Non Hermitian Hamiltonians to PTS Optics

In 1998 Carl M. Bender and Stefan Boettcher [11] found that it is not necessary for Hamiltonian to be Hermitian to have real eigenvalues, as long as they satisfy condition of Parity-Time Symmetry. Until that time it was considered that a condition for a Hamiltonian to have real spectra, and thus to have a physical observable, was for it to obey the Dirac Hermiticity, expressed as $H^\dagger=H$. Bender and Boettcher argued that even quantum systems with non-Hermitian Hamiltonians can have real spectrum if they possess the PT-symmetry. This condition stipulates that the Hamiltonian is invariant under the action of the Parity and Time operators. The action of P and T operators on the position vector x , momentum p and i defined by:

$$\mathcal{P} : x \rightarrow -x; p \rightarrow -p \quad (1.10a)$$

$$\mathcal{T} : x \rightarrow x; p \rightarrow -p; i \rightarrow -i \quad (1.10b)$$

The Parity-Time Symmetry (or PT Symmetry, PTS) thus appears to be a less restrictive condition than hermiticity for a Hamiltonians to have real spectra. An interesting corollary to this theory is that Hamiltonian with potential of the form $V(-x)=-V^*(x)$ will respect Parity Time Symmetry and thus have a capability to exhibit real spectra.

These findings, the origins if which lie in theoretical mathematics, had many unforeseen consequences particularly in modern optics. Because of the equivalence between the Schrödinger equation in quantum mechanics and the classical wave equation presented in table 1.1, optics has turned to be an ideal realm of application of the concepts of PT symmetry. The expression of the physical potential is then associated to the effective index, and will amount to the same condition: $n(x)=n^*(-x)$.

Schrödinger equation and potential	Coupled wave equation and potential
$j\hbar \frac{\partial}{\partial t} \Psi = \begin{pmatrix} r' + jr'' & s \\ s & r' - jr'' \end{pmatrix} \Psi$ $V(\hat{x}) = V^*(-\hat{x})$	$j \frac{\partial}{\partial z} \begin{pmatrix} a_1 \\ a_2 \end{pmatrix} = \begin{pmatrix} \beta + j\gamma & \kappa \\ \kappa & \beta - j\gamma \end{pmatrix} \begin{pmatrix} a_1 \\ a_2 \end{pmatrix}$ $n(x) = n^*(-x) \begin{cases} \text{Re}(n(x)) = \text{Re}(n(-x)) \\ \text{Im}(n(x)) = -\text{Im}(n(-x)) \end{cases}$

Table 1.1. Equivalence between Schrödinger equation and classical wave coupling equation

The matrix formalism of the coupled wave equation presented here is related to the coupling between to co-propagative waves, as would be the case in a directional coupler, which differs from the contra propagative formalism presented earlier to introduce the working principle of DFB lasers. The condition that arises from this analogy is that the real and imaginary parts of the index must be respectively even and odd functions of the position to satisfy the condition of PT symmetry. This situation is interestingly found in the association of two modulations: one of the intrinsic gain/loss, and one of the refractive index of the material, shifted of a quarter of their period. A schematic representation of this condition is presented figure 1.3.

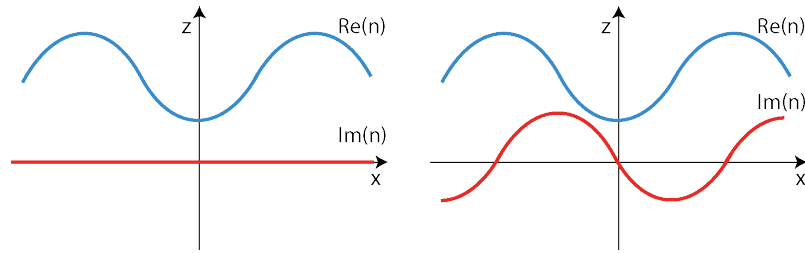


Fig. 1.3. Index profile of a conventional (a) coupled system, and of a PT symmetric (b) coupled system.

From this material topography, many theoretical devices were imagined and reported, some of which gave birth to experimental demonstrations. These achievements include optical phase transition from PT symmetry phase to PT broken phase [12, 13, 14, 15, 16, 17, 18], band merging effects [13, 15], unidirectional behavior [19, 20], PT coherent absorber [21, 22] or PT coherent absorber laser [23, 24, 21, 25]. The two best known examples of PT symmetric systems in modern optics are the PT symmetric directional coupler and the PT symmetric Bragg grating. In the case of the PTS directional coupler, the coupling between waves appear copropagatively whereas for the PTS Bragg grating the waves are coupled contrapropagatively. Both examples are interesting model systems to understand the physics of Parity Time symmetry in optics and will be detailed later.

1.2.2 Exceptional Point

An interesting characteristic associated with PT symmetric systems is the sudden change in their output due to a spontaneous breakdown of PT symmetry. Beyond this border, materialized by the presence of an exceptional point, the PT symmetric structure tips from an unbroken PT symmetric to broken PT symmetric domain. The optical behavior is drastically altered and interesting phenomena can be observed such as unidirectional attenuation/amplification or asymmetric guiding of directional coupler system. Theoretical findings about this exceptional point were first made by Bender et al. in 1999 [26], Klaiman et al. [12] and Makris et al. [13].

From these observations, it became clear that by working around this phase transition point, PT-symmetry approach was promising, e.g. for the realization of tunable optical devices. From the first experimental proposal by Ruschhaupt, Delgado and Muga [27], to El-Ganainy et al., who designed the theoretical framework of a directional coupler [28], a lot of work was soon devoted to the design of optical devices working around this exceptional point of Parity-Time symmetry [28, 13, 29].

1.2.3 PT symmetric Bragg grating

The principle of a conventional Bragg grating has been previously exposed, for the special case of DFB lasers. As for many types of photonic crystals, this structure most often integrates a modulation of either real or imaginary part of the material index, and therefore represents an interesting architecture for the implementation of Parity Time symmetry optics. Indeed, by bringing an additional shifted gain/loss modulation to a conventional refractive Bragg grating structure, the system can be turned into a PT symmetric potential, notably for a phase shift of $\pi/2$ between the gain and refractive index modulations, real and imaginary parts of the material index will have the form of respectively even and odd functions of the position (see Figure 1.4).

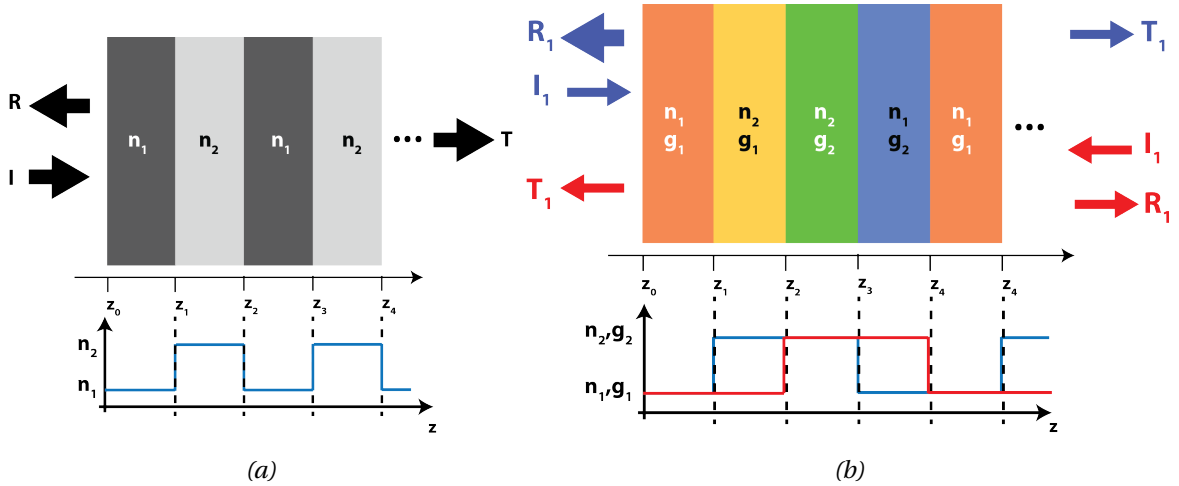


Fig. 1.4. Layout comparison of a conventional Bragg grating (a) and a PTS Bragg grating (b)

By designing the Parity-Time symmetric Bragg grating to work above the exceptional point, the eigenstates of the structure will be degenerate, and recent works proved the possibility of asymmetric light transport [19, 15, 30, 31]. In this case, the system is designed to work in the broken PT symmetric regime, in which the reflection from one hand will be amplified while being attenuated from the other. The transmission is not affected by the presence of the grating, its coefficient and phase thus remaining constant. In 2011 Lin et al. first reported the spontaneous PT-symmetry breaking inside such Bragg grating [19], demonstrating that such systems -when operating around PT-symmetric breaking point-, acts as a unidirectional invisible media.

The non-reciprocal light propagation characteristics of such PT symmetric Bragg grating has attracted a lot of interest, although few experimental achievements were reported, demonstrating differences in directional reflection and transmission. The work of Feng et al. is particularly interesting on this topic, as it represents pioneer experimental results of this index modulated structure in optical resonators systems [32], or linear Bragg reflectors[20]. It thus became clear that, as for conventional DFB lasers, the so called PTS Bragg grating could be used to design Parity-Time Symmetric DFB lasers. The concept of Parity-Time symmetry was then seen as a great asset to improve both wavelength selectivity and feedback resistance of conventional DFB lasers [33, 34], or even implement new functionalities [35]. The ambition of the work discussed in this manuscript is to contribute to the exploration of this approach, by applying the concept of Parity-Time symmetry to integrated optics, through the design and fabrication of PTS DFB lasers.

1.3 Objectives of this work

The work reported in this manuscript is a first attempt to fabricate and characterize DFB lasers involving a modulation of both real and imaginary parts of the material index. The aim here is to control the phase shift between these two modulation components in order to study potential effects induced on the laser operation. A specific phase shift is expected to impact the laser emission and give asymmetric properties such as enhanced feedback tolerance [33], reflected wave amplification [36, 30] or modal gain discrimination [36], due to Parity-Time Symmetry.

The next chapter is dedicated to the simulation of mode dynamics inside DFB lasers using Abeles matrix formalism, and the proposition of a design for an asymmetric directional coupler involving PT symmetry, compliant with fabrication tolerances.

1.4 Références

- [1] TeleGeography. <https://www.submarinecablemap.com/>. URL <https://www.submarinecablemap.com/>. 7
- [2] H. Kogelnik and C. V. Shank. Stimulated emission in a periodic structure. *Applied Physics Letters*, 18(4):152–154, 1971. doi: <http://dx.doi.org/10.1063/1.1653605>. URL <http://scitation.aip.org/content/aip/journal/apl/18/4/10.1063/1.1653605>. 8
- [3] H. Kogelnik and C. V. Shank. Coupled-wave theory of distributed feedback lasers. *Journal of Applied Physics*, 43(5):2327–2335, 1972. doi: <http://dx.doi.org/10.1063/1.1661499>. URL <http://scitation.aip.org/content/aip/journal/jap/43/5/10.1063/1.1661499>. 8
- [4] Herwig Kogelnik. Coupled wave theory for thick hologram gratings. *Bell System Technical Journal*, 48(9):2909–2947, 1969. ISSN 1538-7305. doi: 10.1002/j.1538-7305.1969.tb01198.x. URL <http://dx.doi.org/10.1002/j.1538-7305.1969.tb01198.x>. 8
- [5] W. Streifer, D. R. Scifres, and R. D. Burnham. Periodic corrugated dielectric waveguides. *Fiber and Integrated Optics*, 1:63–75, 1977. 10
- [6] E. Kapon, A. Hardy, and A. Katzir. The effect of complex coupling coefficients on distributed feedback lasers. *IEEE Journal of Quantum Electronics*, 18(1):66–71, Jan 1982. ISSN 0018-9197. doi: 10.1109/JQE.1982.1071364. 10
- [7] Muhammad Arif and Mohammad A. Karim. Analysis of a dephased complex-coupled distributed-feedback laser by the power-series method. *Appl. Opt.*, 39(6):954–961, Feb 2000. doi: 10.1364/AO.39.000954. URL <http://ao.osa.org/abstract.cfm?URI=ao-39-6-954>. 10
- [8] D. A. Cardimona, M. P. Sharma, V. Kovanis, and A. Gavrielides. Dephased index and gain coupling in distributed feedback lasers. *IEEE Journal of Quantum Electronics*, 31(1):60–66, Jan 1995. ISSN 0018-9197. doi: 10.1109/3.341708. 10
- [9] Y. Boucher. Non-reciprocal effects of complex-coupled distributed-feedback structures resulting from the phase difference between the coupling constants. *Optics Communications*, 136:410–414, February 1997. doi: 10.1016/S0030-4018(96)00719-5. 10
- [10] Thierry Fessant. Non-reciprocal emission with high single-mode operation in multisection complex-coupled distributed feedback cavities. *Optics Communications*, 152(1):189 – 197, 1998. ISSN 0030-4018. doi: [https://doi.org/10.1016/S0030-4018\(98\)00072-8](https://doi.org/10.1016/S0030-4018(98)00072-8). URL <http://www.sciencedirect.com/science/article/pii/S0030401898000728>. 10
- [11] Carl M. Bender and Stefan Boettcher. Real spectra in non-hermitian hamiltonians having pt symmetry. *Phys. Rev. Lett.*, 80:5243–5246, Jun 1998. doi: 10.1103/PhysRevLett.80.5243. URL <http://link.aps.org/doi/10.1103/PhysRevLett.80.5243>. 11

- [12] S. Klaiman, U. Günther, and N. Moiseyev. Visualization of Branch Points in PT-Symmetric Waveguides. *Physical Review Letters*, 101(8):080402, August 2008. doi: 10.1103/PhysRevLett.101.080402. [12](#)
- [13] K. G. Makris, R. El-Ganainy, D. N. Christodoulides, and Z. H. Musslimani. Beam dynamics in \mathcal{PT} symmetric optical lattices. *Phys. Rev. Lett.*, 100:103904, Mar 2008. doi: 10.1103/PhysRevLett.100.103904. URL <https://link.aps.org/doi/10.1103/PhysRevLett.100.103904>. [12](#)
- [14] Christian E. Rüter, Ramy El-Ganainy, Demetrios N. Christodoulides, Mordechai Segev, and Detlef Kip. Observation of parity–time symmetry in optics. *Nature Physics*, 6, 2010. [12](#)
- [15] Alois Regensburger, Christoph Bersch, M. Miri, Georgy Onishchukov, Demetrios N Christodoulides, and Ulf Peschel. Parity–time synthetic photonic lattices. *Nature*, 488:167–171, 2012. [12](#), [13](#)
- [16] S. Longhi. Bloch oscillations in complex crystals with PT symmetry. *ArXiv e-prints*, January 2010. [12](#)
- [17] Brian Baum, Hadiseh Alaeian, and Jennifer Dionne. A parity-time symmetric coherent plasmonic absorber-amplifier. *Journal of Applied Physics*, 117(6):063106, 2015. doi: 10.1063/1.4907871. URL <https://doi.org/10.1063/1.4907871>. [12](#)
- [18] A. Guo, G. J. Salamo, D. Duchesne, R. Morandotti, M. Volatier-Ravat, V. Aimez, G. A. Siviloglou, and D. N. Christodoulides. Observation of \mathcal{PT} -symmetry breaking in complex optical potentials. *Phys. Rev. Lett.*, 103:093902, Aug 2009. doi: 10.1103/PhysRevLett.103.093902. URL <https://link.aps.org/doi/10.1103/PhysRevLett.103.093902>. [12](#)
- [19] Zin Lin, Hamidreza Ramezani, Toni Eichelkraut, Tsampikos Kottos, Hui Cao, and Demetrios N. Christodoulides. Unidirectional invisibility induced by \mathcal{PT} -symmetric periodic structures. *Phys. Rev. Lett.*, 106:213901, May 2011. doi: 10.1103/PhysRevLett.106.213901. URL <http://link.aps.org/doi/10.1103/PhysRevLett.106.213901>. [12](#), [13](#)
- [20] Liang Feng, Ye-Long Xu, William dos Santos Fegadolli, Minghui Lu, José Edimar Barbosa Oliveira, Vilson R Almeida, Yan-Feng Chen, and Axel Scherer. Experimental demonstration of a unidirectional reflectionless parity-time metamaterial at optical frequencies. *Nature materials*, 12 2:108–13, 2013. [12](#), [13](#)
- [21] Y. D. Chong, Li Ge, Hui Cao, and A. D. Stone. Coherent perfect absorbers: Time-reversed lasers. *Phys. Rev. Lett.*, 105:053901, Jul 2010. doi: 10.1103/PhysRevLett.105.053901. URL <https://link.aps.org/doi/10.1103/PhysRevLett.105.053901>. [12](#)
- [22] Wenjie Wan, Yidong Chong, Li Ge, Heeso Noh, A. Douglas Stone, and Hui Cao. Time-reversed lasing and interferometric control of absorption. *Science*, 331(6019):889–892, 2011. ISSN 0036-8075. doi: 10.1126/science.1200735. URL <http://science.sciencemag.org/content/331/6019/889>. [12](#)
- [23] Stefano Longhi. Pt-symmetric laser absorber. *Physical Review. A*, 82(3), Sep 2010. doi: 10.1103/PHYSREVA.82.031801. [12](#)

- [24] Stefano Longhi and Liang Feng. Pt-symmetric microring laser-absorber. *Opt. Lett.*, 39(17):5026–5029, Sep 2014. doi: 10.1364/OL.39.005026. URL <http://ol.osa.org/abstract.cfm?URI=ol-39-17-5026>. 12
- [25] Y. D. Chong, L. Ge, and A. D. Stone. PT-Symmetry Breaking and Laser-Absorber Modes in Optical Scattering Systems. *Physical Review Letters*, 106(9):093902, March 2011. doi: 10.1103/PhysRevLett.106.093902. 12
- [26] Carl M. Bender, Stefan Boettcher, and Peter N. Meisinger. Pt-symmetric quantum mechanics. *Journal of Mathematical Physics*, 40(5):2201–2229, 1999. doi: 10.1063/1.532860. URL <https://doi.org/10.1063/1.532860>. 12
- [27] A. Ruschhaupt, F. Delgado, and J. G. Muga. LETTER TO THE EDITOR: Physical realization of \mathcal{PT} -symmetric potential scattering in a planar slab waveguide. *Journal of Physics A Mathematical General*, 38:L171–L176, March 2005. doi: 10.1088/0305-4470/38/9/L03. 12
- [28] R. El-Ganainy, K. G. Makris, D. N. Christodoulides, and Ziad H. Musslimani. Theory of coupled optical pt-symmetric structures. *Opt. Lett.*, 32(17):2632–2634, Sep 2007. doi: 10.1364/OL.32.002632. URL <http://ol.osa.org/abstract.cfm?URI=ol-32-17-2632>. 12
- [29] K. G. Makris, Ramy El-Ganainy, D. N. Christodoulides, and Z. H. Musslimani. Optical solitons in pt periodic potentials. *2008 Conference on Lasers and Electro-Optics and 2008 Conference on Quantum Electronics and Laser Science*, pages 1–2, 2008. 12
- [30] Mykola Kulishov, Jacques M. Laniel, Nicolas Bélanger, José Azaña, and David V. Plant. Nonreciprocal waveguide bragg gratings. *Opt. Express*, 13(8):3068–3078, Apr 2005. doi: 10.1364/OPEX.13.003068. URL <http://www.opticsexpress.org/abstract.cfm?URI=oe-13-8-3068>. 13
- [31] Mykola Kulishov, Bernard Kress, and Radan Slavík. Resonant cavities based on parity-time-symmetric diffractive gratings. *Optics express*, 21(8):9473–9483, 2013. 13
- [32] Han Zhao, Pei Miao, Mohammad H. Teimourpour, Simon Malzard, Ramy El-Ganainy, Henning Schomerus, and Liang Feng. Topological hybrid silicon micro-lasers. *Nature Communications*, 9(1):981–, 2018. ISSN 2041-1723. URL <https://doi.org/10.1038/s41467-018-03434-2>. 13
- [33] Cheng Ke, Xun Li, and Yanping Xi. Parity-time symmetric complex-coupled distributed feedback laser with excellent immunity to external optical feedback. *AIP Advances*, 7(3):035010, 2017. doi: 10.1063/1.4978447. URL <http://dx.doi.org/10.1063/1.4978447>. 13
- [34] Mykola Kulishov and Bernard Kress. Distributed bragg reflector structures based on pt-symmetric coupling with lowest possible lasing threshold. *Opt. Express*, 21(19):22327–22337, Sep 2013. doi: 10.1364/OE.21.022327. URL <http://www.opticsexpress.org/abstract.cfm?URI=oe-21-19-22327>. 13
- [35] C. Y. Huang, R. Zhang, J. L. Han, J. Zheng, and J. Q. Xu. Type-ii perfect absorption and amplification modes with controllable bandwidth in combined \mathcal{PT} -symmetric and conventional bragg-grating structures. *Phys. Rev. A*, 89:023842, Feb 2014. doi: 10.1103/PhysRevA.89.023842. URL <https://link.aps.org/doi/10.1103/PhysRevA.89.023842>. 13

- [36] Y. Zhu, Y. Zhao, J. Fan, and L. Zhu. Modal gain analysis of parity-time-symmetric distributed feedback lasers. *IEEE Journal of Selected Topics in Quantum Electronics*, 22(5):5–11, Sept 2016. ISSN 1077-260X. doi: 10.1109/JSTQE.2016.2537209. [13](#)

Chapter 2

Implementation of PT-symmetry in practical devices

The concept of Parity-Time symmetry has raised a lot of interest in the realm of optics for nearly a decade. With the presence of an exceptional point, at the frontier of broken and unbroken PT symmetric regimes, optical circuits designer found a powerful asset in their design toolbox. Indeed, by working around this phase transition point, exotic behavior arise and the PT symmetric system output can be largely tuned by changing the amount of gain in the system. As discussed in the previous chapter, a wide range of functionalities can be implemented from the association of only two building blocks: the PT-symmetric Bragg grating, and PT-symmetric directional coupler.

In our ambition to use Parity-Time symmetry for the design and fabrication of practical devices, we present in this chapter the work performed on the study of modal behavior in conventional and PT symmetric DFB lasers using Abelès matrix formalism, and a novel approach easing fabrication tolerances in the fabrication of PT-symmetric directional coupler. These efforts represent important milestones in the realization of respectively PT symmetric Bragg grating and directional coupler. The second half of this chapter is dedicated to a discussion around the feasibility of a PT-symmetric directional coupler, from the point of view of fabrication tolerances. Existing solutions reported in the literature are discussed, and a new device associating well-known integrated optics tools is proposed to deal with the fabrication constraints.

2.1 Simulation of Bragg reflectors using Abelès formulation

Numerical simulation of distributed Bragg grating structures is presented in this section. The objective here is to compare the mode dynamics between conventional DFB structures, based on either gain or index coupling mechanisms, and complex-coupled DFB lasers. The specific case of a quarter period gratings phase shift is of great interest, as it represents the requirement to be fulfilled to satisfy the condition of PT-symmetry.

We detail in the appendix a matrix method that will provides reflection and transmission coefficient of a Bragg grating periodic structure, through the simulation of plane wave propagation inside a stack of layers of different index using Abelès matrix formalism. The hypotheses of a plane wave formalism represents an important simplification, balanced with the computation of effective indices under a modal method. The association of a plane wave model with a modal method of effective indices computation is an efficient way to simulate the effects of real and imaginary index modulation (classical in integrated optics). In addition to its efficiency, the simplicity of the Abelès matrix formalism is here of great interest, because its transparent and explicit form ensures quick and robust validation.

2.2 Modal behavior inside DFB laser structures

The mode selectivity in semiconductor lasers is an intricate mechanism: unlike other types of lasers, the emission spectrum is not determined by spectral intensity clamping, but by mode competition inside the cavity.

In the previous chapter, we presented the model of a DFB laser structure in which both real and imaginary parts of the index can be modulated. Using Abelès transfer matrices formalism, we chose to express the reflectivity and transmissivity coefficients of such structures. Within the framework of this study we observe that a set of parameters related to the laser geometry has a great impact on the response of our structure. We particularly

study the spectral response of the DFB lasers depending on the gratings facet phase.

To this end, we simulate the response of DFB lasers of several kinds in the presence or absence of facets by changing the outside index from n_{eff} to 1. These two cases will be later referred as AR-coated and non AR-coated (or cleaved facet) lasers respectively, as the absence of facets can be experimentally obtained by the addition of an Anti-Reflection (AR) coating to the laser facet. To get a better insight we also present the effects of the grating phase at the facet, It is indeed physically important because the substantial facet reflectivity can add in-phase or out-of-phase with the grating's own reflection, at extreme cases.

The simulation results are presented under the form of a map displaying the reflected and transmitted amplitudes of incident wave depending on the imaginary part of the index (modeling an increasing amount of gain inside the cavity) and the wavelength. Results for 1st and 3rd order DFB lasers are presented, this choice being related to fabrication constraints, and further exploited in the following chapter.

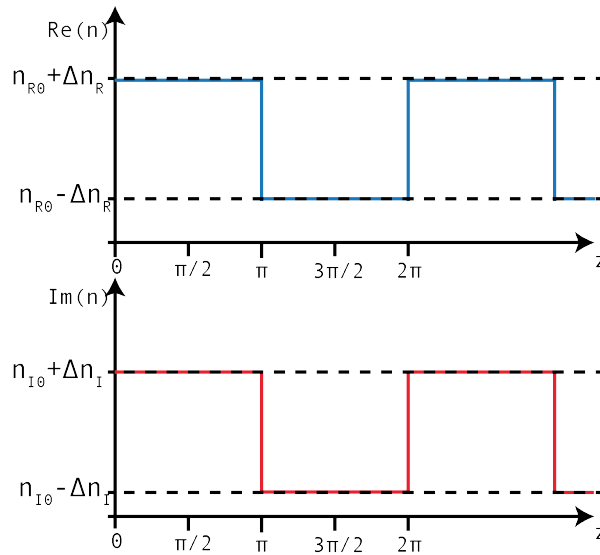


Fig. 2.1. Convention taken for phase of real (top) and imaginary (bottom) parts of the index

Here we note n_{RE} and n_{IM} the real and imaginary parts of the index respectively, n_{R0} , n_{I0} , Δn_R and Δn_I are the mean values of the real and imaginary parts of the index and their respective modulation amplitudes. On top of that, we must set a reference when discussing the laser facet, to fix the origin from which the facet phase is expressed. This convention is presented in figure 2.1. The reference situates the region of high index between (real or imaginary) phases 0 and π .

To start with a rather simplified model, our structure will first feature an integer number of Bragg periods.

2.2.1 Case of a conventional 3rd order index-coupled DFB laser

Figure 2.2 shows the reflected (a) and transmitted (b) wave amplitude of a conventional AR-coated 3rd order index-coupled DFB laser depending on the magnitude of n_{IM} (expressing the gain inside the laser cavity), through a 10nm spectral range, centered on $1.550\mu\text{m}$.

In this ideal case, two modes with equal threshold gain are first amplified with the increase of gain (Figure 2.2 (c) and (d)). The stop-band between them is related to the the

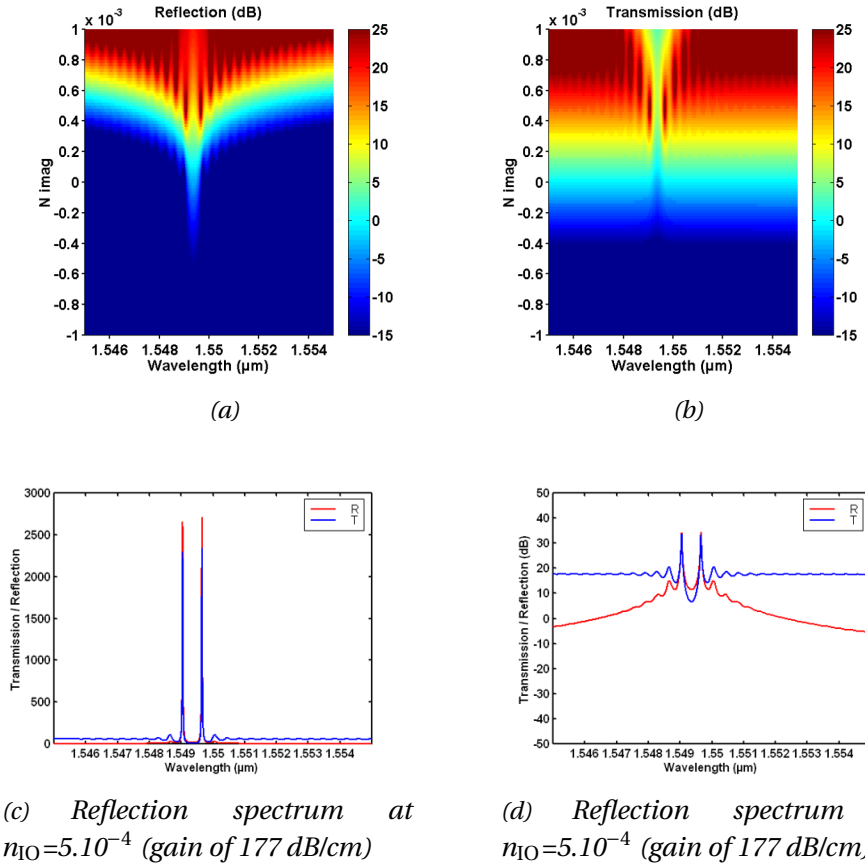


Fig. 2.2. Transmission (a) and Reflection (b) maps and sections at threshold ((c) and (d)) of a traveling wave inside an AR-coated 3rd order index-coupled DFB laser

coupling coefficient magnitude. Despite the lack of internal feedback due to AR-coating, the lasing mode amplification appears at relatively low gain level, around 177 dB/cm, as no additional losses are introduced by the purely index-coupled grating.

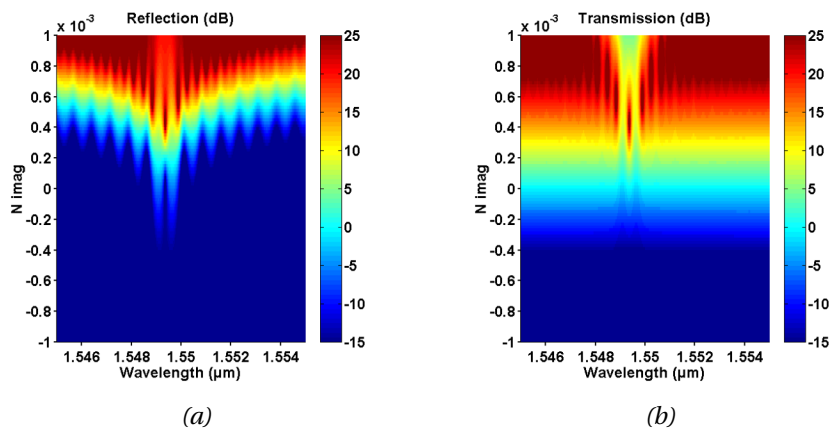


Fig. 2.3. Transmission (a) and Reflection (b) maps of a traveling wave inside a facet free 3rd order index-coupled DFB laser, containing a $\pi/2$ phase shift section

The mode selection in an IC DFB laser can simply be achieved by cleaving of laser, in this case the grating phase at the facets will discriminate one of the two main modes over the other, as can be seen in figure 2.4. As well known, this process is better controlled by introducing a $1/4$ phase shift section inside the laser cavity. This solution, preferred in the

industry for its repeatability, is presented figure 2.3.

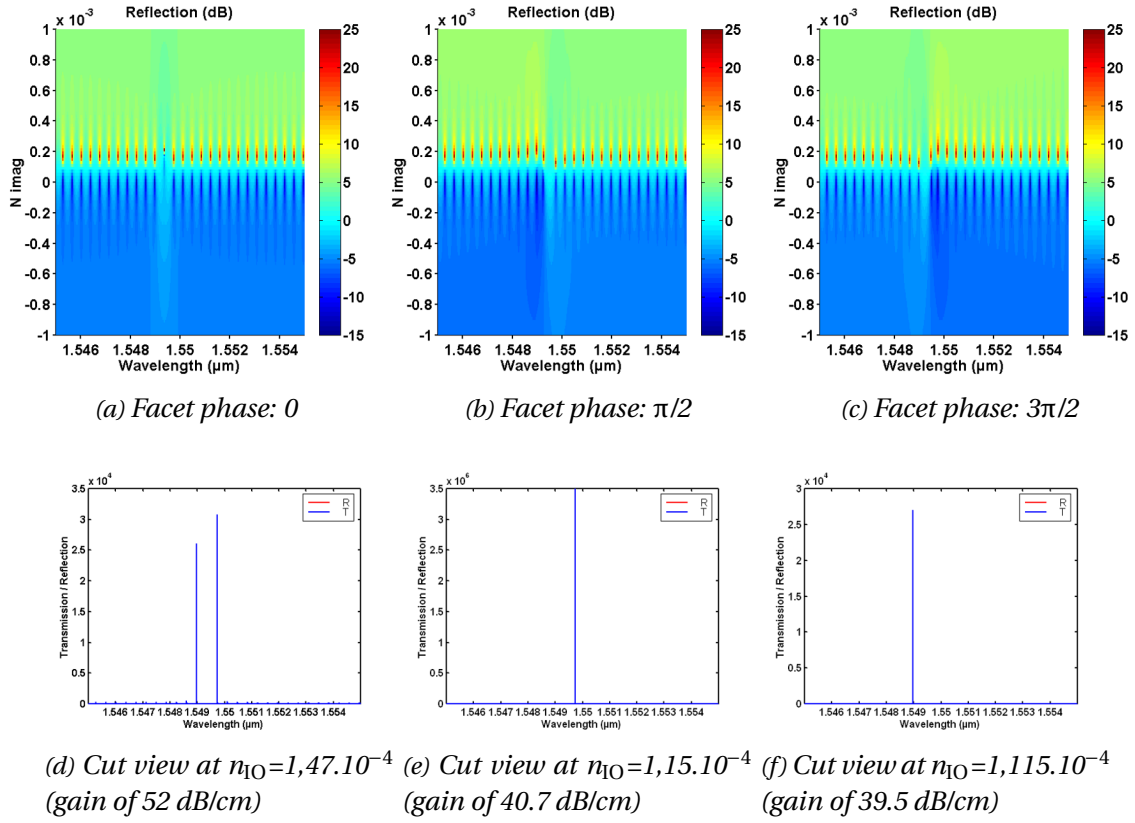


Fig. 2.4. Reflection maps and associated sections at threshold of a traveling wave inside a non AR-coated 3rd order index-coupled DFB laser with different facet phase

In the case of a non AR-coated index-coupled DFB laser, the spectrum of the Fabry-Perot resonances inside the cavity become visible, through the presence of cavity modes for gain values of around $n_{Im}=1,6 \cdot 10^{-4}$ (gain of 56.64dB/cm). Whereas the amplitude map was previously quite continuous, we here observe the emergence of local maxima, all gathered around this central gain value. These local extrema correspond to the poles of the transfer matrix. When the gain reaches one of the poles, the mode is amplified and stimulated emission takes place.

If this type of map does not inform about the mode dynamics after stimulated emission is reached, as the model becomes non-linear, the first mode to reach stimulated emission and its associate threshold gain are however trustworthy information. Furthermore, the distance of the first rising poles to the Fabry-Perot resonances ones gives us an important indication on the emergence of this mode and its modal discrimination margin, Δg_{th} .

Concerning the amplitude of reflected and transmitted waves of the non AR-coated index-coupled DFB laser, the couple of modes emerging makes it quite similar to the AR-coated case, but is distinguishable by the presence of Fabry-Perot (FP) resonance. As the threshold gain margin is very low, the single mode operation will not be very much resistant. At some point the emission will become multimode as the modes of the FP cavity emerge, and the monomodality of the laser will be lost.

It is however interesting to note that the global amount of gain required to reach stimulated emission is decreased from the AR-coated case (gain of 40dB/cm to 52dB/cm), with the associated imaginary part of the index divided by a factor of 2. This observation is

true for any kind of grating assisted lasers, as the presence of facet reflections increase the internal feedback of the laser cavity.

In the following sections, the effect of the facet phase and cavity configuration on the evolution of the modes inside the laser cavity is discussed. The gain threshold of the cavity modes, and the threshold gain difference between the first and the second (or lower) rising poles of the gain/spectrum map are considered. These two indicators will be used as function of merit and are presented in figure 2.5. The extraction of the poles characteristics was performed with a local maximum search algorithm.

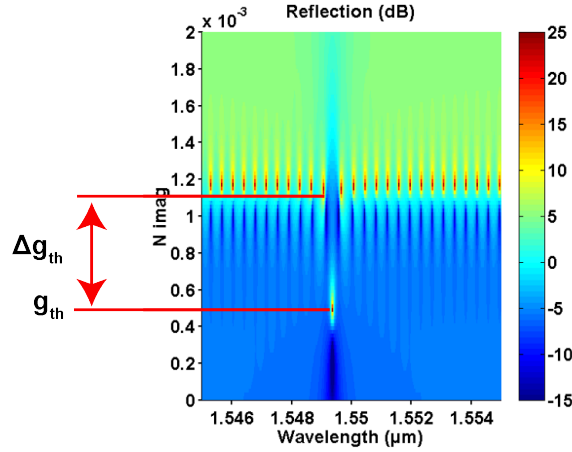


Fig. 2.5. Presentation of the gain threshold (g_{th}) and gain threshold margin (Δg_{th}).

2.2.2 Effect of facet phase on IC DFB lasers emission characteristics

The mode evolution inside first order non AR-coated IC DFB laser cavity with varying facet phase is here investigated. The cases of lasers with an integer number N , $N+0.25$, $N+0.5$ and $N+0.75$ of periods was studied. For each of these four cases, the index grating phase at the entry facet took values of 0 , $\pi/4$, $\pi/2$, $3\pi/4$, π , $5\pi/4$, $3\pi/2$ and $7\pi/4$. The threshold values of the first rising pole (threshold gain) and the distance of this pole to the second rising pole (threshold gain margin) in each configuration are presented in figure 2.6.

Beside the symmetry and periodicity of these graphics, which can be explained by the redundancy of the grating geometry in the case $N \gg 1$, we can here get a better insight of the mode selection mechanism inside the IC DFB laser cavity. The plot on left hand side of figure 2.6, shows that the configuration of $N+0.5$ number of period is the worst in terms of lasing threshold g_{th} . The graphic on the right hand side of figure 2.6 shows that in this configuration, the emission is even systematically multimode, revealed by the gain threshold distance to the second pole, Δg_{th} , null. This spectral behavior can be explained by the high threshold gain of the first rising pole, around 52 dB/cm which is comparable to the gain of the Fabry-Perot modes, at 55,6 dB/cm. The lowest pole (first rising pole) will be closer to the Fabry-Perot cavity poles, thus decreasing the threshold gain margin. It is thus a case of destructive interference between facet and grating feedback.

Equivalent results were obtained for grating made of N periods at facet phases of 0 and π . Under this configuration, the threshold value is maximal, and the laser is multimode. For this cavity length, the remaining facet phases however give low threshold and gain difference to second mode. The best monomode yield is obtained for cavity length of $N+0.25$ and $N+0.75$ periods. For these lasers, the evolution of g_{th} and Δg_{th} are symmetrical with

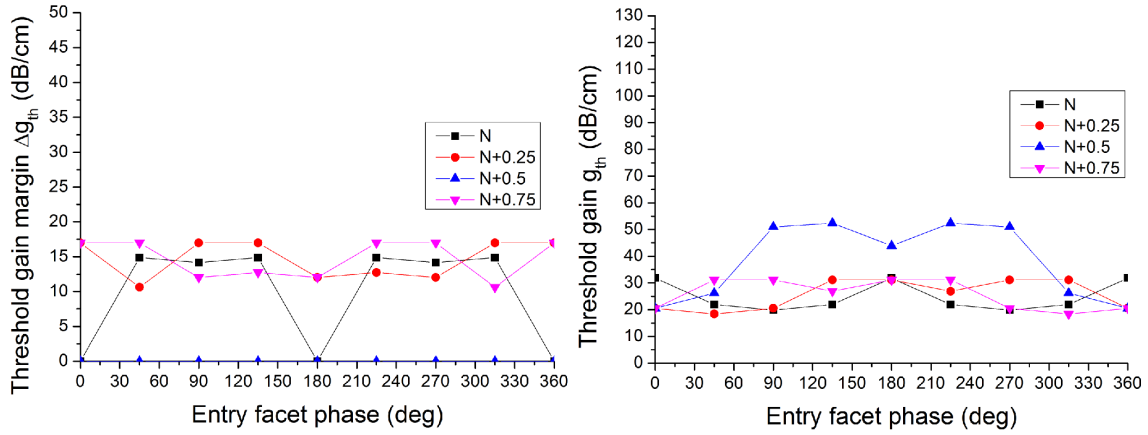


Fig. 2.6. Evolution of the threshold gain margin (left) and threshold gain (right) for first order IC DFB lasers with N , $N+0.25$, $N+0.5$, $N+0.75$ number of periods versus entry facet phase.

regards to the π phase. For these cavity lengths, the monomodality is always achieved and threshold gain equivalent to the case of N number of periods is achieved.

Similar observations were made on the simulations of third order non AR-coated IC DFB lasers. Figure 2.7 presents the threshold gain and threshold gain margin for a variation of facet phase and 4 cavity lengths. The evolution is similar to the case of first order index-coupling, with however a significant difference in threshold gain and threshold gain margin values. Notably, the third order IC DFB laser presents a higher threshold gain and lower threshold gain margin, leading to a potential shorter monomode current range and lower Side Mode Suppressing Ratio (SMSR) value.

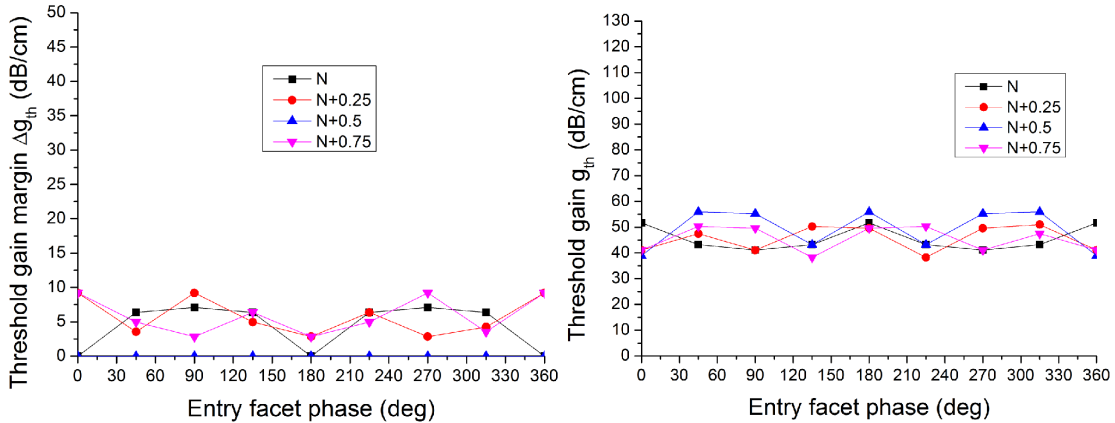


Fig. 2.7. Evolution of the threshold gain margin (left) and threshold gain (right) for third order IC DFB lasers with N , $N+0.25$, $N+0.5$, $N+0.75$ number of periods versus entry facet phase.

2.2.3 Case of a conventional gain-coupled DFB laser

Figure 2.8 shows the simulation results obtained for the case of a first order gain coupled DFB-laser with cleaved facet and $\Delta n_I = 1.10^{-4}$ real part of the index variation. As observed previously, F-P cavity modes are added to the mode satisfying the Bragg condition. It is worth noting that unlike the index-coupled DFB laser, a single mode is here rising inside

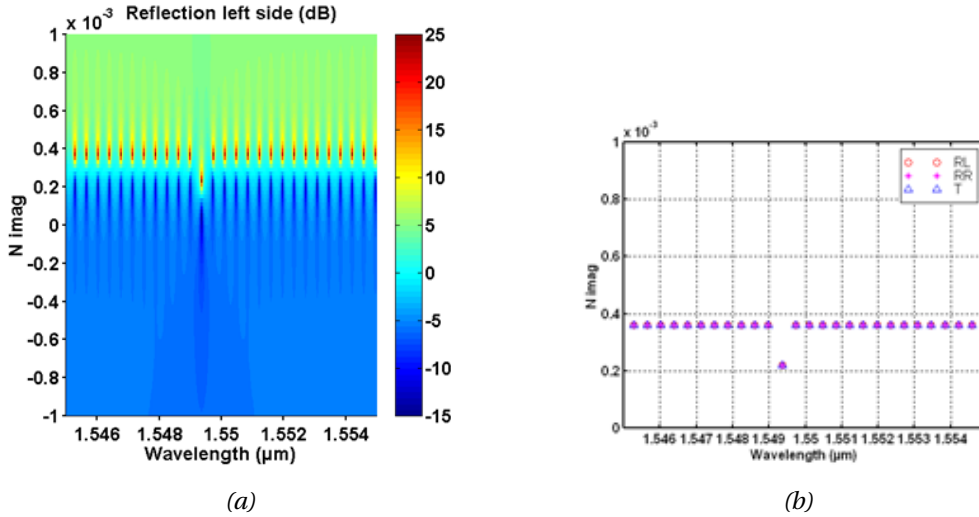


Fig. 2.8. amplification of the modes inside the laser cavity (a) and position of the poles (b) for a non AR-coated 1st order GC DFB laser

the cavity. The threshold gain margin is also improved. $\pi/2$ and $3\pi/2$ correspond to the same grating in which the light would be traveling in opposite directions.

Working at 3rd order naturally leads to a degradation of the laser's spectral behavior and internal feedback. The coupling between the wave and the grating is affected, resulting in a decreased emission power. A comparison between first and third order GC DFB lasers in terms of gain threshold and gain threshold difference is presented thereafter.

2.2.4 Effect of facet phase on GC DFB lasers emission characteristics

Similarly to the case of cleaved facets first and third order IC DFB lasers, the effect of facet phase on threshold gain and threshold gain margin of GC DFB lasers was investigated. Figure 2.9 shows the evolution of g_{th} and Δg_{th} versus the entry facet phase and for first order GC DFB lasers of varying length.

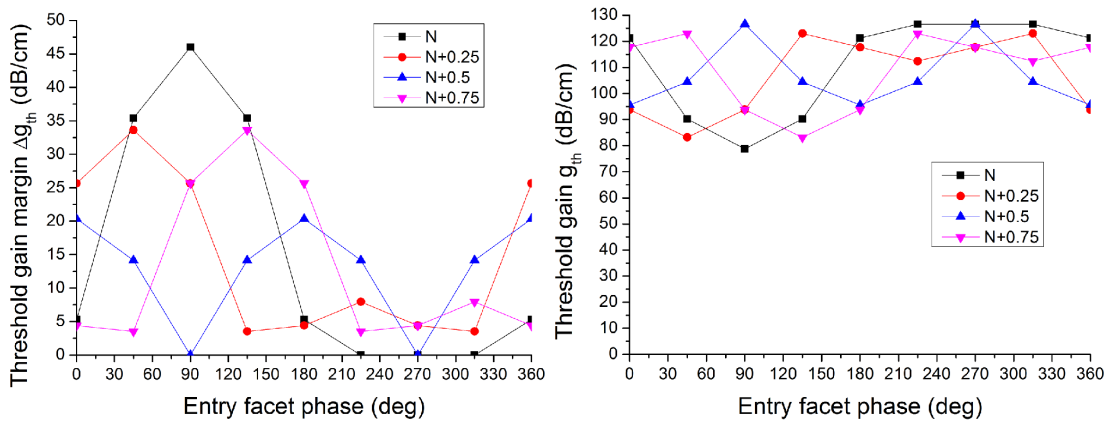


Fig. 2.9. Evolution of the threshold gain (left) and threshold gain margin (right) for first order GC DFB lasers with N , $N+0.25$, $N+0.5$, $N+0.75$ number of periods versus entry facet phase.

By comparing results presented on figure 2.9 to the previous case of IC DFB lasers, we observe that the threshold gain is here increased by a factor 4 because of the presence of the loss grating. The threshold gain margin of first order GC DFB laser, however, is

increased by a factor of 3 compared to its IC counterpart. This strongly suggest that such laser will be monomode over a wider current range, with a potential higher SMSR value. Furthermore, over the large range of cavity length and facet phase investigated, only 4 configurations show a threshold gain margin of 0, which proves that the monomodality of this type of laser is almost systematic. These observations are in good agreement with the studies made from a long time on the resistance of first order gain-coupled DFB lasers on their remarkable monomode stability.

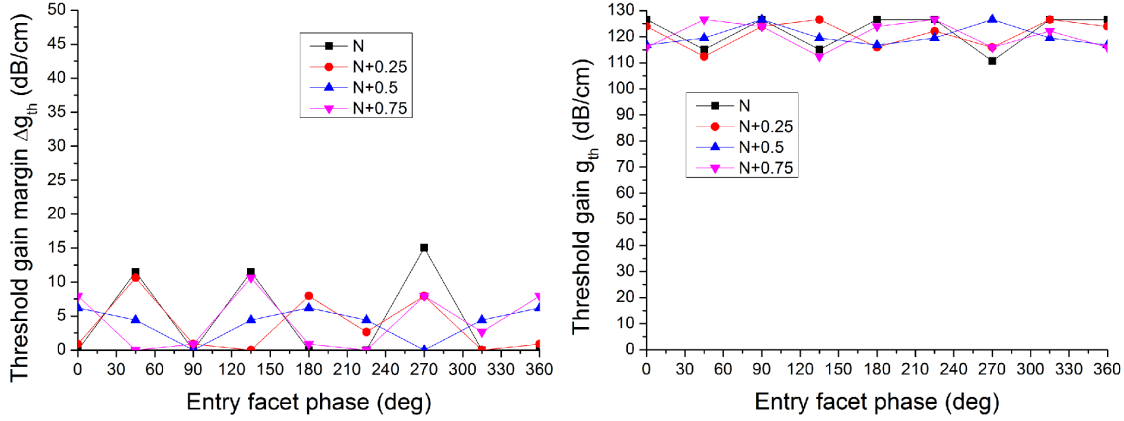


Fig. 2.10. Evolution of the threshold gain margin (left) and threshold gain (right) for third order GC DFB lasers with N , $N+0.25$, $N+0.5$, $N+0.75$ number of periods versus entry facet phase.

The case of third order GC DFB laser is far less favorable. As can be seen on figure 2.10, if the gain threshold values are conserved with regards to first order GC DFB lasers, the gain threshold margin is however largely decreased. The overall value of threshold margin value is here 3 times lower, and the number of multimode configurations is 17, almost 5 times larger than the at first order. However, third order GC DFB laser is found to have a higher threshold margin than its IC DFB laser equivalent (above-10 dB/cm⁻¹ range vs. below-10 dB/cm⁻¹ range).

It must be mentioned here that diffraction induced losses being not taken into account in our plane wave model, the gain threshold value should be higher than predicted here, even if this effect is not expected to have a strong dependence on facet.

2.2.5 Case of complex-coupled DFB laser

In this section we apply the same strategy to the analysis of the mode evolution inside the cavity of CC DFB lasers with cleaved facets. The investigation is this time trickier, as the relative phase between index and gain gratings also impact the modal behavior of these types of lasers. The relevant information here being the potential performances of our lasers and their tolerances to random cleaving locations, we hence represent the gain threshold and gain threshold difference depending on the relative phase between the index and gain gratings.

Though figure 2.11 presents a high density of information, the overall tendencies can be analyzed. The minimum threshold gain reachable by any grating phase configuration, 100 dB/cm, is slightly lower than for the most favorable facet cleaving case of third order GC DFB lasers, with over 110dB/cm. The maximum reachable threshold gain margin, is also slightly increased. If the best performances are obtained for specific facet phase of gratings in or out of phase, the homogeneity over the facet phase variation is highest

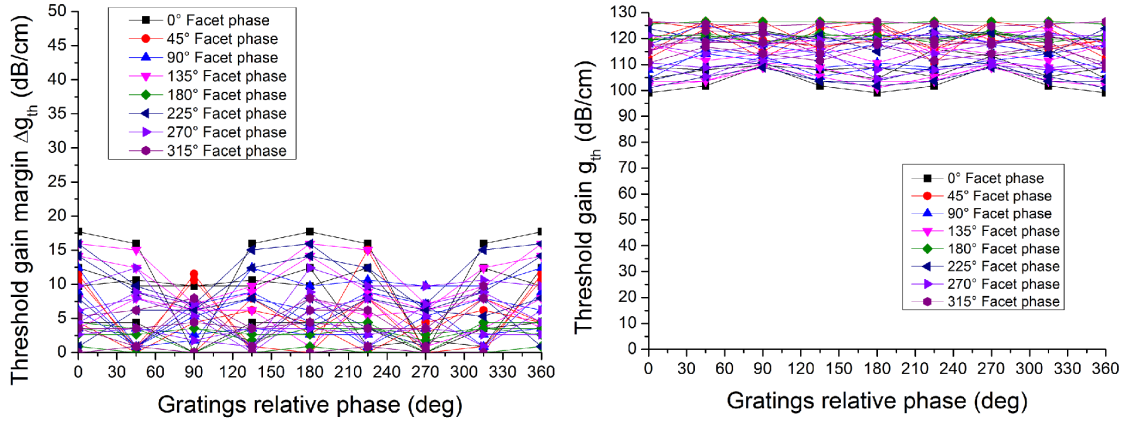


Fig. 2.11. Evolution of the threshold gain margin (left) and threshold gain (right) for third order CC DFB lasers with $N, N+0.25, N+0.5, N+0.75$ number of periods and at different facet phase versus gratings relative phase.

for gratings relative phase of $\pi/2$ and $3\pi/2$. It is hence plausible that respecting the PT symmetric condition (with corresponding phases of $\pi/2$ and $3\pi/2$) does not increase the reachable laser characteristics, but rather reduces the performances variation versus the facets locations.

To compare the laser characteristics between IC, GC and CC DFB laser together with their immunity to facet phase, the results presented were compiled in a characteristic map. This map is formed by the threshold gain and threshold gain margin (see figure 2.12). Each item, located with $(g_{th}, \Delta g_{th})$, represent the performances obtained from the simulation of a given geometry, defined by the entry facet phase and cavity length (between $N, N+0.25, N+0.5, N+0.75$).

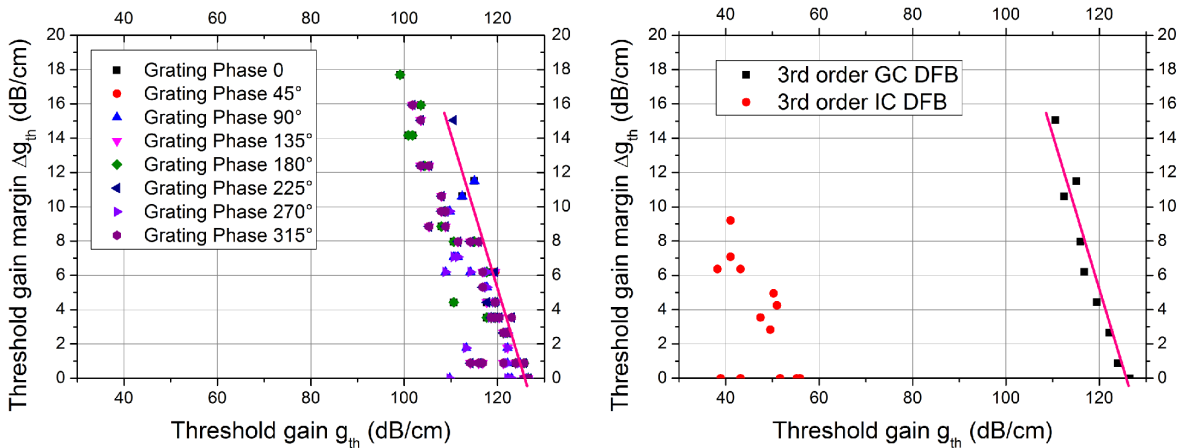


Fig. 2.12. Characteristic map of IC, GC (right) and dephased CC (left) DFB lasers. Each item present on the map represent a specific facet phase and cavity configuration ($N, N+0.25, N+0.5$ and $N+0.75$ cavity length).

Figure 2.12 is a comparison of the IC, GC and dephased CC DFB lasers in terms of emission characteristics. The advantages of IC and GC technologies are to attain respectively low threshold gain and large threshold difference, but these assets are not compatible within a combination of both of the gratings. On the other hand, the performances of dephased CC DFB lasers remains in the vicinity of what is obtained by GC DFB lasers. However, the slight improvement that can be seen here has to be put into perspective as the

indices modulation magnitudes are here respectively of $\Delta n_{RE}=2.10^{-3}$ and $\Delta n_{IM}=4.10^{-4}$. Indeed, despite the order of magnitude difference between the index modulation components, the simulation results show stronger similitude between CC and GC DFB lasers emission characteristics. We could hence imagine that an even weaker imaginary index modulation, would lead to the improvement of CC DFB lasers performances, toward what was obtained with IC DFB lasers.

2.2.6 Asymmetric response of DFB lasers and effects of facet reflections

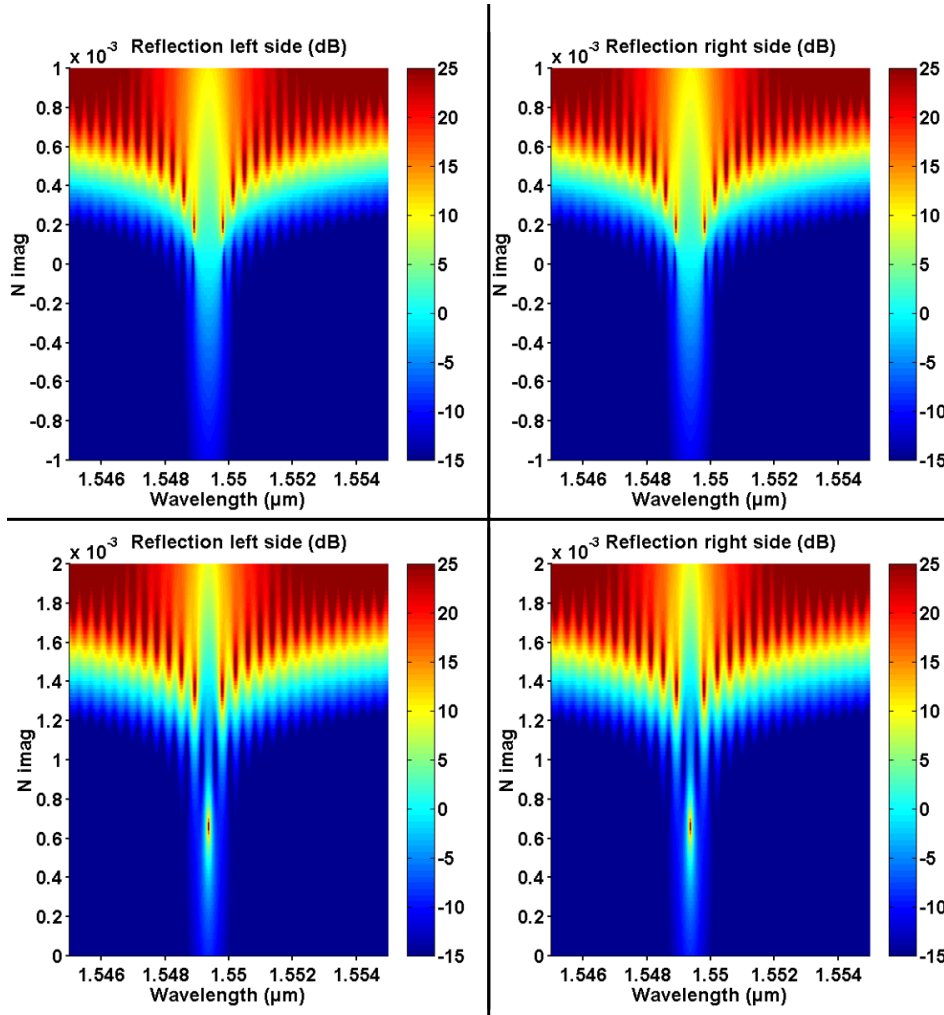


Fig. 2.13. Characteristic map of AR-coated first order IC (top) and GC (bottom) DFB lasers in both directions of propagation (left, right).

We investigate here the potential asymmetry observed in the mode evolution inside DFB laser cavities. Figure 2.13 presents the amplification map in reflection for AR-coated first order IC (top) and GC (bottom) DFB lasers in both directions of propagation. The gain threshold and gain threshold margin values have already been discussed for such DFB laser cavities with cleaved facets. In both cases, the amplified reflection spectrum is similar in propagation direction 1 (left) and 2 (right), in agreement with the underlying laser grating symmetry.

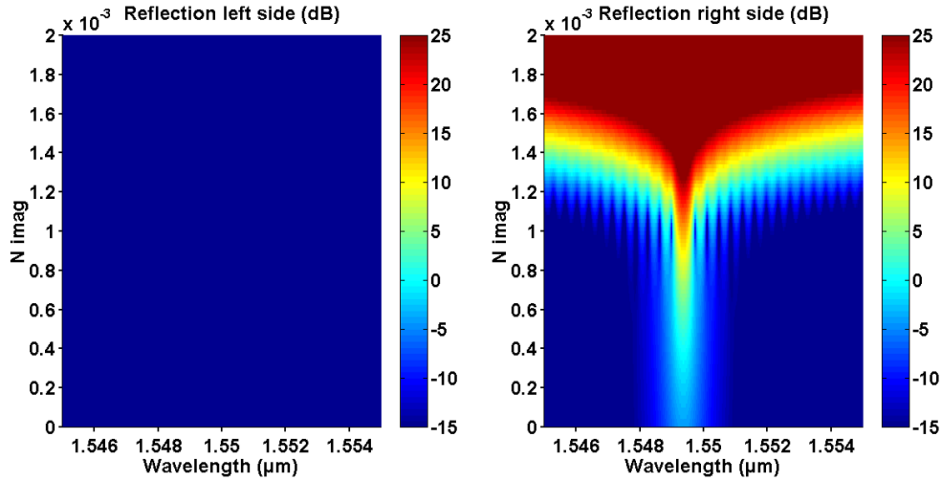


Fig. 2.14. Characteristic map of AR-coated first order CC DFB laser respecting the PT symmetric condition, in both directions of propagation (left, right).

The case of PT symmetry, known for its intriguing behavior (see chapter 1) is presented in Figure 2.14. We here consider the grating to operated at first order, without facet reflections and the relative gratings phase is $\pi/2$ in order to respect the PT symmetry condition. The asymmetry of the amplified reflection spectrum is here striking, as in one direction of propagation the light will be amplified in the vicinity of the Bragg wavelength, and attenuated along the full spectrum in the other direction of propagation.

Furthermore, by shifting the gratings away from this specific condition of PT symmetry, the asymmetry in reflection amplification remains. As shows Figure 2.15, as soon as both gratings are not in phase (phase 0) or out of phase (phase π) i.e when the index and gain/loss profile is not symmetric, the amplification reflection map shows differences depending on the propagation direction. Precisely, one direction will be affected by a stronger attenuation (or in presence of gain, a weaker amplification) than the other.

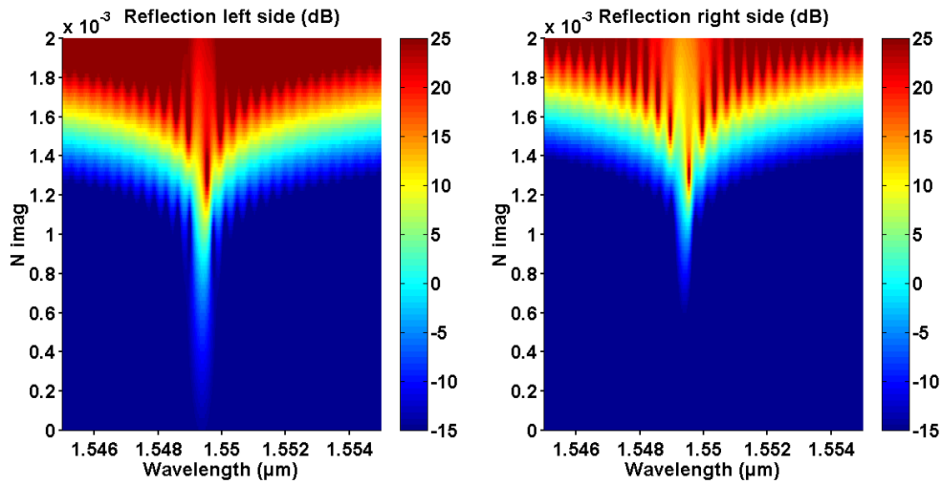


Fig. 2.15. Characteristic map of AR-coated first order CC DFB laser with gratings phase shift of $3\pi/4$, in both directions of propagation (left, right).

In our approach to apply PT symmetry to practical devices, the case of facet reflection must be dealt with. Indeed, the sole grating feedback of our DFB lasers is not sufficient to reach laser operation and additional reflectors are required. We are hence interested in studying the potential asymmetry of the reflected spectrum of cavities in presence of facet reflections.

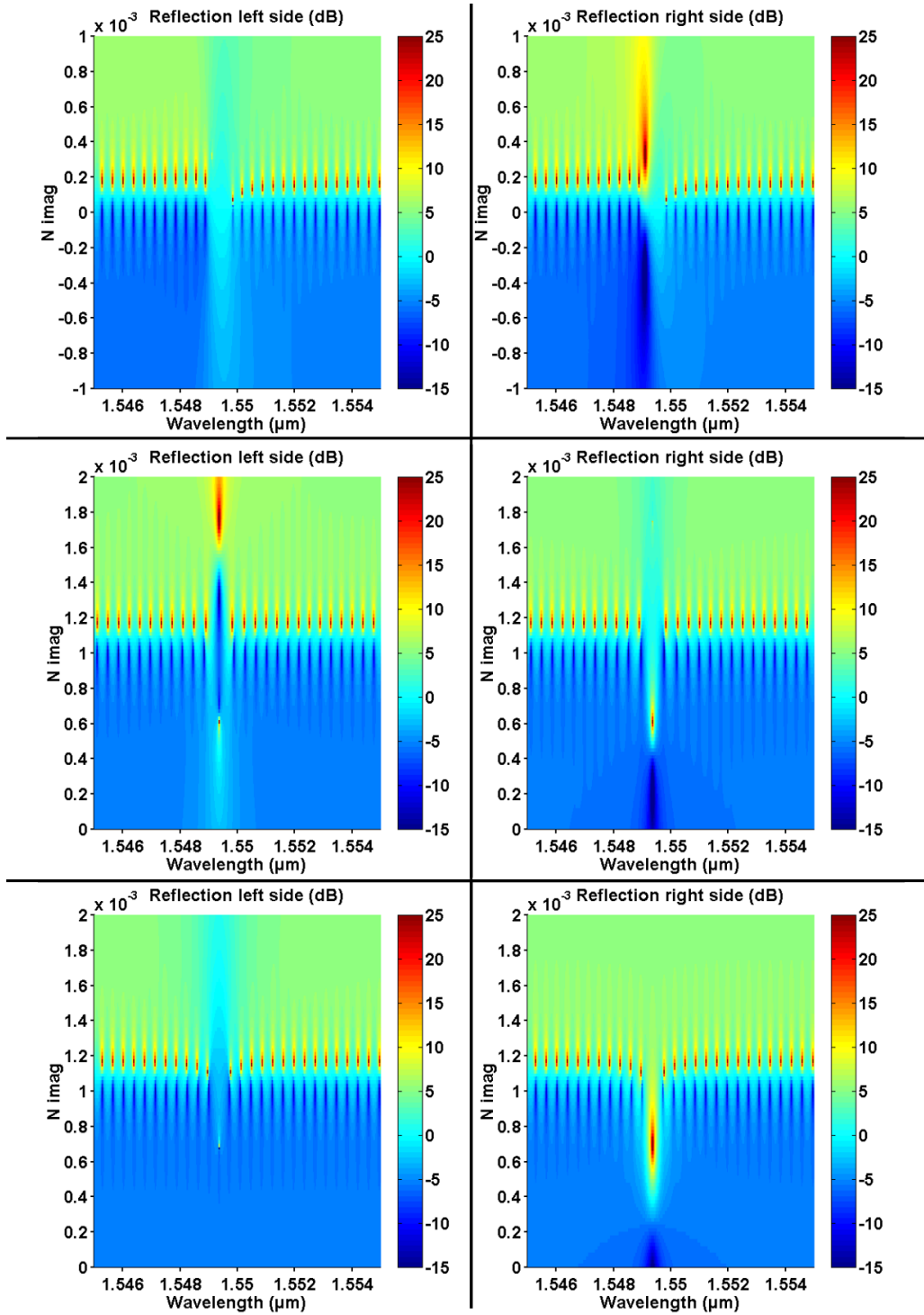


Fig. 2.16. Characteristic map of non AR-coated first order IC (top), GC (middle) and PTS CC (bottom) DFB lasers, in both directions of propagation (left, right).

Figure 2.16 presents the map of the amplified reflection spectrum of IC (top), GC (middle) and CC (bottom) DFB lasers with cleaved facets. The CC DFB laser respects the PT symmetry, with a relative phase shift of $\pi/2$ between gratings. As mentioned in the previous sections, the spectrum is here influenced by the Fabry-Perot resonance. The modulation of the real and imaginary parts of the index in the case of CC DFB lasers are similar to the IC and GC and of equal amplitudes, with $\Delta n_{RE,IM}=2.10^{-3}$.

This figure describes well enough the observations we made during our investigations on

the effects of facet phase on the amplification spectrum of the different laser cavities. Indeed, if the reflection map of the PT symmetric grating (figure 2.16 bottom) is different from one propagation direction to the other, the facet reflections influence the symmetry of the amplification for conventional IC and GC DFB laser cavities as well. Specifically we observed that the amplification spectrum is asymmetric as soon as the coupling (i.e. index or gain/loss) profile is also asymmetric. These observations are valid for first and third order.

In the light of these simulations, it appears that the unidirectional amplification in reflection of CC DFB lasers with facet reflections should not be mistaken for PT symmetric induced effect originating from the combination of index and gain grating.

2.2.7 Conclusion and objectives of this work

In this first part, we simulated the evolution of modes inside IC, GC and CC DFB laser cavities, using Abelès matrix formalism. The performances of first and third order conventional IC and GC DFB lasers with variation of facet phase was investigated, and the threshold gain g_{th} and threshold gain margin Δg_{th} were monitored. The advantages of low threshold gain and high threshold gain margin were exposed for respectively IC and GC DFB lasers, with the specific example of index variation of $\Delta n_{RE}=2.10^{-3}$ and $\Delta n_{IM}=4.10^{-4}$. The advantages of combining both coupling mechanisms, was studied with the case of CC DFB lasers. It was found that the threshold gain of CC DFB lasers is slightly improved with regards to their GC counterparts, though remaining well above IC DFB lasers performances. This proves that the metallic contribution should be decreased to reach optimum threshold gain performances.

We emphasized that complex coupling DFB lasers could present exotic behavior by the expression of Parity-Time symmetry. In such grating, the real and imaginary parts are shifted from a quarter of their period, satisfying the PTS condition $n(x)=n^*(-x)$. By entering the regime of broken PT symmetry, non-reciprocal propagation of an incident light can be observed: its reflection being amplified in one direction and attenuated in the opposite. Furthermore, we observed that weaker asymmetric amplification of reflection was possible in the case of CC DFB lasers, as soon as metallic and index gratings are neither in nor out of phase. In practice, asymmetric amplification profile can be found in reflection for conventional IC or GC DFB lasers in presence of facet reflection. This phenomenon, originating from the asymmetry of the index or gain/loss profile brought by the face reflections, should not be mistaken with the PTS unidirectional amplification in reflection. If Parity-Time symmetry can be used through the coupling of contra-propagative waves, which will be the case of the experimental work of this thesis, co-propagative coupling is a fertile playground for PT symmetry, as it can be used to implement an optical switch. From these two building blocks, a wide variety of optical functions can be created such as buffer memories, re-configurable spatial multiplexers or single mode amplifier to name but a few.

The example of the PTS optical switch is discussed in the second part of this chapter.

2.3 Design of a Parity-Time Symmetric coupler

A pair of coupled waveguides with gain and loss represents the simplest configuration of PT-symmetric optical system (PTSS), which was extensively studied in view of optical signals manipulation [1, 2, 3, 4, 5, 6, 7, 8, 9, 10] or of terahertz devices [11, 12]. For such system, light is introduced in a waveguide carrying gain which through its propagation evanescently couples into a waveguide carrying losses. By tuning the amount of gain in the system, the coupling length is changed, changing the output state or the coupler, enabling switching operation. Such abrupt variation in the coupler output is here made possible by the presence of Exceptional Point (EP), and the adjustment of the system parameters around it.

Several studies focused their attention on the singular properties of PT-symmetric optical system (PTSS) related to the abrupt evolution of propagation constants $\beta+i\beta''$ in the vicinity of the EP singularity [4, 6, 7, 8, 9, 10]. Experimentally however, achieving operation right at the EP is far from being trivial. The main factors causing the smearing of EP spectral singularity are the imbalance in propagation constants of coupled waveguides [9, 10] and/or a complex-valued coupling coefficient [8, 9]. To circumvent these issues, the solution proposed to recover the spectral singularity at the EP is to consider a design with vertically stacked waveguides having different core thickness [9]. The phase matching condition between non-identical waveguides is obtained by using for the core a dispersive material of very high gain ($\approx 1500 \text{ cm}^{-1}$).

Our work on this topic was to propose a more affordable solution in terms of gain (loss) level. For 1-mm length-scale device, the required gain (loss) level of our design does not exceed $\approx 50 \text{ cm}^{-1}$ (i.e. approximately 200 dB/cm). Furthermore, this design not only ensures a robust recovery of the EP singularity, but it is also perfectly suited for binary switching operation below EP [13, 14]. In addition it does not impair the use of birefringence compensation technique for achieving polarization-independent operation [15].

2.3.1 Impact of the detuning due to fabrication constrains

To present our approach, we start with the simplest model of two coupled waveguides, one with gain and the other with balanced losses. We consider two scalar fields a_1 and a_2 propagating in these waveguides and described by the system:

$$j \frac{da_1}{dz} = (\beta_1 + i\gamma)a_1 + \kappa a_2; \quad j \frac{da_2}{dz} = \kappa a_1 + (\beta_2 - i\gamma)a_2 \quad (2.1)$$

Where $\kappa = \kappa' + i\kappa''$ is the complex coupling coefficient while γ is the z-invariant gain-loss coefficient. As a first approximation, we consider that the coupling coefficient is real (i.e. $\kappa'' = 0$). The eigenvalues of propagation constants in the system are:

$$\sigma = \frac{\beta_1 + \beta_2}{2} \pm \sqrt{\kappa'^2 + \delta^2 - \gamma^2 + 2i\delta\gamma} \quad (2.2)$$

Here the convenient variable $\delta = (\beta_1 + \beta_2)/2$ is the half-detuning of the waveguides propagation constants. As evident from equation 2.2 the presence of an imaginary term in the square-root of the expression leads to the emergence of complex eigenvalues, and further results in the smearing of the EP singularity. The ratio $|\delta + \kappa''|/\kappa$ may serve as a measure of deviation from the ideal case i.e., the EP singularity. To evaluate the impact of the detuning δ , the deviation of waveguides propagation constants, whose limits are dictated by

technological imperfections, we assume for the moment that $\kappa'' = 0$. Expressing a meaningful condition of a "small" detuning around EP singularity then involves the coupling length $L_c = \pi/2\kappa$ as follows:

$$\frac{\delta}{\kappa} = \frac{L_c}{\lambda} (n_2 - n_1) \ll 1 \quad (2.3)$$

Where n_j is the waveguide j effective index. For 1-mm scale coupling length typical for integrated optics and 1- μm scale wavelength, the detuning is negligible when the effective index difference $\Delta n = (n_1 - n_2)$ obeys $\Delta n \ll 10^{-3}$.

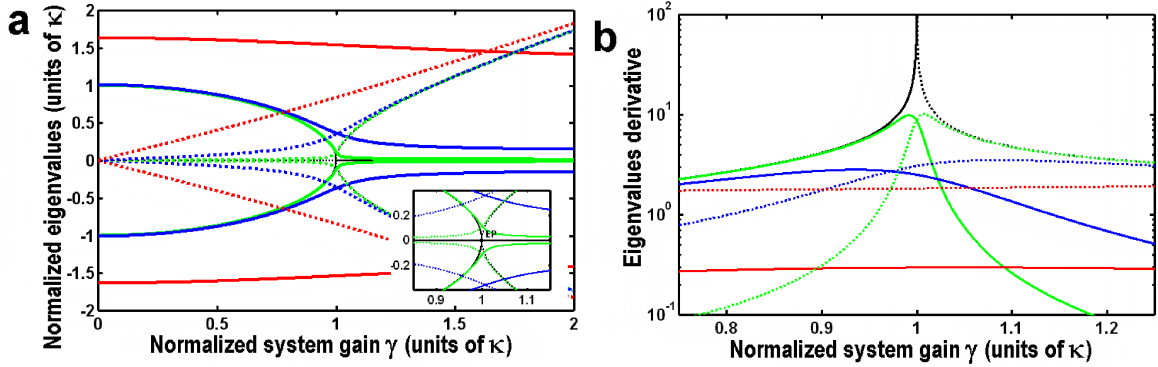


Fig. 2.17. System of PT-symmetric waveguides with different values of detuning ($\Delta n = 0$, black lines; $\Delta n = 10^{-5}$, green lines; $\Delta n = 10^{-4}$, blue lines; $\Delta n = 10^{-3}$, red lines). (a) Real parts (solid lines) and Imaginary parts (dotted lines) of the two normalized eigenvalues β_1 and β_2 ; (b) Real parts (solid lines) and Imaginary parts (dotted lines) of the eigenvalues derivative $d\sigma/d\gamma$.

The detrimental impact of the waveguides effective index difference Δn on the EP singularity is illustrated in figure 2.17 (a). As can be seen, when $\Delta n = 10^{-3}$, the evolution of coupled waveguides eigenvalues as a function of γ widely differs from evolution in the ideal case $\Delta n = 0$. For $\Delta n = 10^{-4}$ some resemblance of eigenvalues curves with respect to the ideal case is retrieved, though large deviations subsist even far from the EP. When $\Delta n = 10^{-5}$ a global behavior approaching to that of an ideal case is recovered, except in the near vicinity of EP (as can be seen on the inset in figure 2.17 (a)). One important parameter that motivated the quest for operating at the EP is the steep variation of eigenvalues ($d\sigma/d\gamma$) in its near vicinity. In the presence of finite detuning δ , the maxima for real and imaginary components of $d\sigma/d\gamma$ are achieved at the inflection points of corresponding branches, $\text{Re}(\sigma)$ and $\text{Im}(\sigma)$. In contrast to the ideal case when $\delta = 0$, the maxima of $d[\text{Re}(\sigma)]/d\gamma$ and $d[\text{Im}(\sigma)]/d\gamma$ on the abscissa axis γ split and go below and above the EP, respectively. Furthermore, a direct but tedious calculation shows that maxima are equidistant (albeit to first order only) from the exact EP ($\gamma/\kappa = 1$):

$$\frac{\gamma_{\text{Re}}}{\kappa} = \sqrt{1 + \frac{4\delta^2}{3\kappa^2} - \frac{1}{\sqrt{3}} \frac{|\delta|}{\kappa}}; \quad \frac{\gamma_{\text{Im}}}{\kappa} = \sqrt{1 + \frac{4\delta^2}{3\kappa^2} + \frac{1}{\sqrt{3}} \frac{|\delta|}{\kappa}} \quad (2.4)$$

It is worth noting that despite it is a linear approximation when $\delta/\kappa \ll 1$, the derivatives $d\text{Re}(\sigma)/d\gamma$ and $d\text{Im}(\sigma)/d\gamma$ are tending toward the same limit:

$$\lim_{\delta \rightarrow 0} \frac{\partial \text{Re}(\sigma)}{\partial \gamma} = \lim_{\delta \rightarrow 0} \frac{\partial \text{Im}(\sigma)}{\partial \gamma} \approx \left(\frac{27}{16}\right)^{-4} \sqrt{\frac{\kappa}{|\delta|}} \quad (2.5)$$

As follows from equation 2.5 the steepness of eigenvalues derivatives $d\sigma/d\gamma$ in the near vicinity of EP grows only as $\gamma^{-1/2}$. It means that in order to increase by an order of magnitude $d\sigma/d\gamma$ from the modest value of 10 observed for $\Delta n = 10^{-5}$ up to a more palatable

10^2 target, the index detuning should be reduced by two orders of magnitude, down to $\Delta n=10^{-7}$, which is all but attainable with any foreseeable technologies.

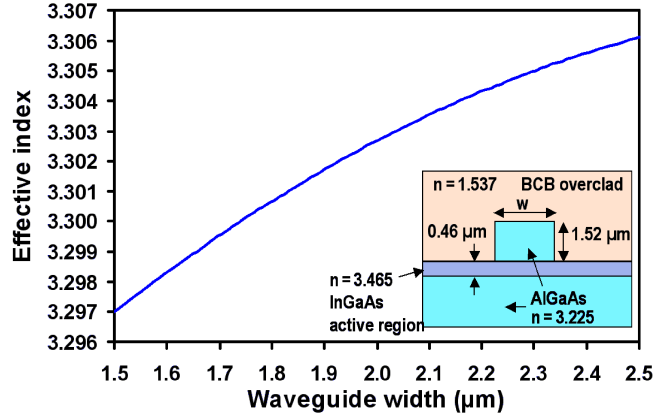


Fig. 2.18. Effective index as function of waveguide width w . Inset: Sketch of an AlGaAs/InGaAs rib waveguide with BCB overclad (values of refractive indices are indicated for $\lambda=1.55\mu m$).

To illustrate this we consider a typical design of III-V semiconductor waveguide with BCB overclad represented in figure 2.18 (a). The numerically calculated dependence of TE polarization effective index as a function of waveguide width w is displayed in figure 2.18 (b). As can be seen for $w \approx 2\mu m$, corresponding to the single mode operation, a variation of waveguide width by 100nm leads to a change in effective index $\Delta n=10^{-3}$. Thus, to achieve $\Delta n=10^{-5}$, the width of the two coupler waveguides should be identical within an accuracy of 1nm. And to achieve a detuning of $\Delta n=10^{-7}$, a sub-atomic precision level is required. Consequently, the capability to control detuning through waveguides geometry and material parameters is definitely quite elusive.

Similar findings holds when considering switching operation in the PT-symmetric phase below EP [13]. Traditionally, such “ 2×2 ” four-port devices operate either in the so-called bar state or in the cross state [16]. To tackle the switch we consider the evolution of the input "binary" state $|\uparrow\rangle = (e^{-i\Phi}, 0)^T$, T standing for the transpose and ket and bra vectors being used for $(a_1, a_2)^T$. We want the output of the device $z=L$ (L being the length of the device) to be either $|\uparrow\rangle$, also called bar state T_{11} , or $|\downarrow\rangle = (0, e^{i\Phi})^T$, called cross state T_{12} . For the considered coupler of length $L=2.1L_c$ with constant coupling and gain-loss profile, the lowest binary state is bar. It is achieved when $\gamma \approx 0.3\kappa$. The second binary state corresponding to the switching operation from bar to cross is achieved at $\gamma \approx 0.7\kappa$.

The transfer matrix of the gain-loss waveguides system of such directional coupler is [16]:

$$M(z) = \begin{pmatrix} \cos(\Omega z) - \frac{j\delta}{\Omega} \sin(\Omega z) & \frac{j\kappa}{\Omega} \sin(\Omega z) \\ \frac{j\kappa}{\Omega} \sin(\Omega z) & \cos(\Omega z) + \frac{j\delta}{\Omega} \sin(\Omega z) \end{pmatrix} \quad (2.6)$$

With:

$$\Omega = \sqrt{\delta^2 + \kappa^2} \quad (2.7)$$

It is then possible to calculate the transmitted light intensity T^{ij} at the output of the j -th waveguide for light injected through the i -th waveguide for $z=L$:

$$T^{ij} = |M_{ij}|^2 \quad (2.8)$$

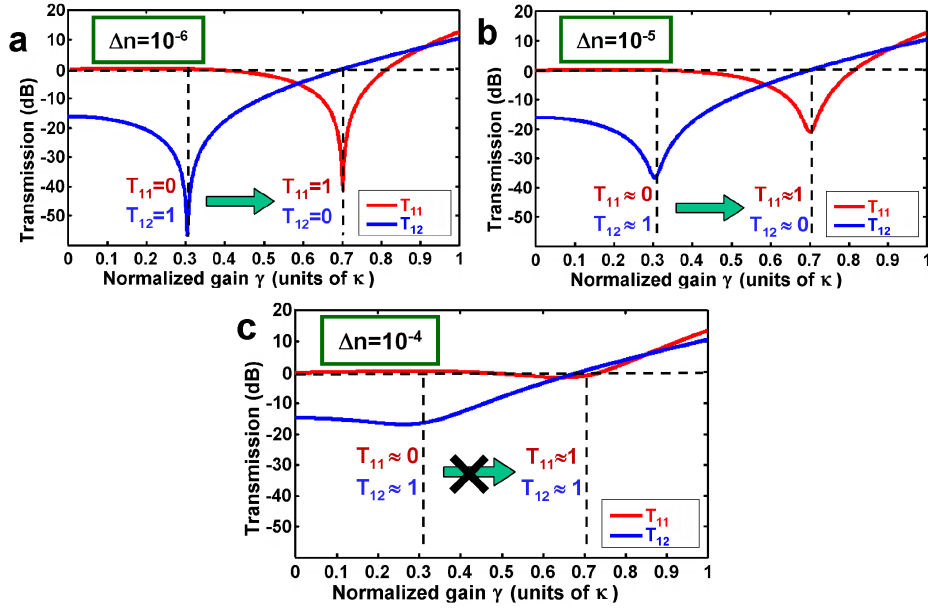


Fig. 2.19. Switching operation of conventional PT-symmetric coupler of length $L=2.1L_c$ for different values of detuning. (a) $\Delta n=10^{-6}$; (b) $\Delta n=10^{-5}$; (c) $\Delta n=10^{-4}$.

The detrimental effect of effective index detuning appears in figure 2.19. Almost perfect switching operation with very low level of zero (<-40 dB) is observed when $\Delta n=10^{-6}$ as can be seen in figure 2.19 (a). As figure 2.19(b) shows, when $\Delta n=10^{-5}$ the switching is still acceptable with the level zero ≈ -20 dB. But further increase of detuning up to $\Delta n=10^{-4}$ totally compromises the switching operation (see figure 2.19 (c)).

Similar behavior for the switching operation and EP singularity is observed when the impact of complex part of the coupling coefficient $\kappa=\kappa'+i\kappa''$ instead of detuning is considered. The measure of smallness in this case is given by the κ''/κ' ratio.

It should be noted that as follows from equation 2.2 the negative impact of κ'' can be compensated by a judicious introduction of detuning δ and vice versa. The associated analysis was performed in [8] and [9]. The issue is that for a fixed detuning δ the impact of κ'' can be corrected only for a single gain point on the eigenvalues dispersion diagram $\sigma(\gamma)$, when meeting the condition:

$$\delta\gamma + \kappa'\kappa'' = 0 \quad (2.9)$$

2.3.2 Grating assisted directional coupler

An alternative solution, consists in compensating detuning by using complex valued coupling coefficient [9]. This provides some freedom to tune the operation point on the $\sigma(\gamma)$ diagram, but, as said, requires huge gain levels. Hence, this solution is not satisfactory either. In the following section, we will consider the coupling coefficient as real.

As follows from equation 2.9 the situation can be remediated if it is possible to modulate the detuning as function of some parameter. The wavelength becomes such a parameter in two interesting cases. First, an asymmetric directional coupler design [17] naturally makes dispersion curves coincide at some wavelength λ_0 ensuring thus the phase matching condition $\beta_1(\lambda_0) = \beta_2(\lambda_0)$. In a linear expansion $\beta_j(\lambda) = \beta_j(\lambda_0) + (\lambda - \lambda_0)d\beta_j/d\lambda$ the detuning δ can be expressed as:

$$\delta = (\lambda - \lambda_0) \frac{d(\beta_1 - \beta_2)}{d\lambda} \quad (2.10)$$

This does offer practical tenability since the typical value of $d(n_1 - n_2)/d\lambda$ for III-V semiconductor waveguides is $\approx 0.01 \mu\text{m}^{-1}$, meaning that a $\Delta\lambda = 10 \text{ pm}$ step, common for laser diode control, readily attains a detuning $\Delta n < 10^{-7}$. Indeed, this is even too fine a tuning.

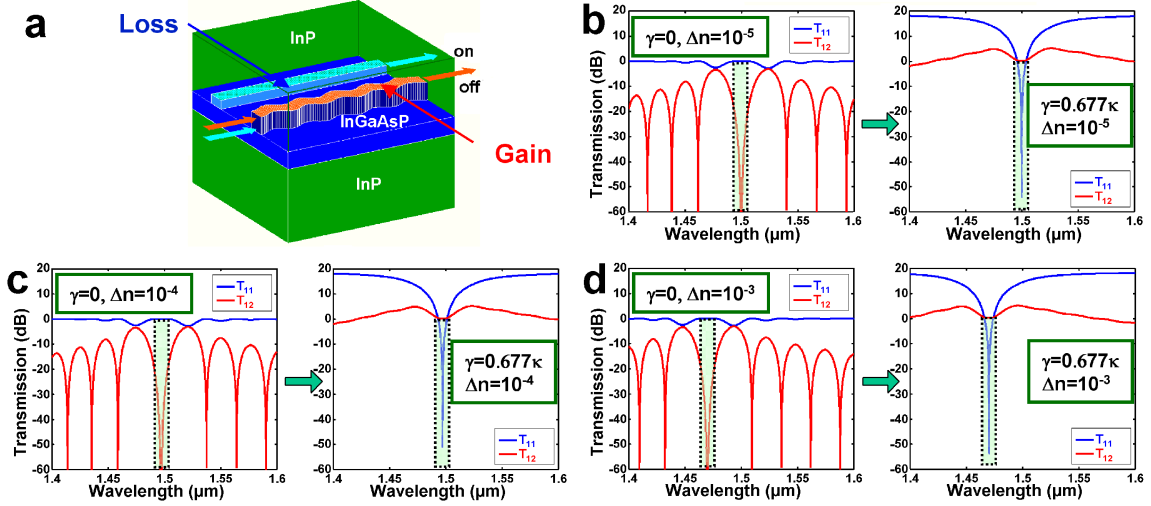


Fig. 2.20. Switching operation of grating assisted PT-symmetric coupler of length $L = 2L_c$ for different values of detuning. (a) $\Delta n = 10^{-5}$; (b) $\Delta n = 10^{-4}$; (c) $\Delta n = 10^{-3}$

The second case, more convenient to hit an adapted detuning (say $\Delta n \approx 10^{-6}$) is to use long period grating assisted directional couplers (GADC), as presented in figure 2.20 (a), providing greater degree of freedom for the choice of materials and design of the waveguides. The gain waveguide is turned into a long period sinusoidal grating, and the phase matching condition in this case becomes:

$$\beta_1(\lambda_0) - \beta_2(\lambda_0) = 2\pi/\Lambda \Leftrightarrow \lambda_0 = \Lambda \cdot [n_1(\lambda_0) - n_2(\lambda_0)] \quad (2.11)$$

Where Λ is the grating period, typically on the order of few tens of microns. Furthermore, the birefringence compensation technique originally proposed in [15] and experimentally demonstrated in [18, 19] allows achieving polarization independent operation.

To this end a condition of identical TE and TM birefringence should be met through appropriate guide design (material composition and geometry):

$$n_1^{\text{TE}} - n_1^{\text{TM}} = n_2^{\text{TE}} - n_2^{\text{TM}} \quad (2.12)$$

To examine the switching behaviour of grating assisted PT-symmetric coupler we consider the example of device with length $L = 2.0L_c = 2 \text{ mm}$, $n_1 = 3.3$, $n_2 = 3.25$, $\Lambda = 30 \mu\text{m}$. According to equation 2.10 the phase matching condition is met at $\lambda_0 = 1.5 \mu\text{m}$. For the given coupler length the bar state $|\uparrow\rangle$ occurs for $\gamma = 0$ and the cross state $|\downarrow\rangle$ is achieved when $\gamma \approx 0.677$ corresponding to amplification level of 18.5 dB [13]. The impact of introducing additional detuning Δn between waveguides is illustrated in figures 2.20 (b) to (d). As can be observed, perfect switching operation is now successfully observed even for $\Delta n = 10^{-3}$, though at the expense of a $\approx 30 \text{ nm}$ shift of the phase-matching wavelength, as can be seen in figure 2.20 (d). The phase matching wavelength is red-shifted if $\Delta n > 0$ and blue-shifted if $\Delta n < 0$. The shift scales linearly with Δn and is thus down to $\Delta\lambda_0 \approx 1 \text{ nm}$ for a feasible

target $\Delta n \approx 3.3 \cdot 10^{-5}$. Such shifts from the nominal value can be commonly compensated using for instance a thermal tuning mechanism [19]. Note also that the amplification (attenuation) γ required for switching can be reduced down to only 13.6dB level by considering an appropriate square longitudinal modulation of the gain-loss profile as detailed in a recent optimization study [14].

2.4 Conclusion on the design of PTS GADC

In summary, the impact of effective index detuning in a system of PT-symmetric coupled waveguides is considered. It is shown that for a 2-mm-long coupler, the achievement of EP singularity as well as switching operation in PT-symmetric phase requires a detuning typically lower than $\Delta n \approx 10^{-5}$. Achieving a detuning below this limit seems elusive because of tight constraints imposed on fabrication technology. To circumvent these issues a long-period grating-assisted PT-symmetric coupler design was considered and shown to perform well at the expense of a manageable wavelength shift. The proposed solution advantageously restores robust binary switching operation and exceptional point singularity. In addition such design is compatible with birefringence compensation techniques providing polarization-independent operation as well as with gain-loss or coupling longitudinal profile tailoring allowing reduction of amplification (attenuation) level with respect to the conventional uniform PT-symmetric coupler design.

2.5 Références

- [1] Christian E. Rüter, Ramy El-Ganainy, Demetrios N. Christodoulides, Mordechai Segev, and Detlef Kip. Observation of parity–time symmetry in optics. *Nature Physics*, 6, 2010. 34
- [2] P. L. Chu, G. D. Peng, B. A. Malomed, H. Hatami-Hanza, and I. M. Skinner. Time-domain soliton filter based on a semidissipative dual-core fiber. *Opt. Lett.*, 20(10): 1092–1094, May 1995. doi: 10.1364/OL.20.001092. URL <http://ol.osa.org/abstract.cfm?URI=ol-20-10-1092>. 34
- [3] Boris A. Malomed, G. D. Peng, and P. L. Chu. Nonlinear-optical amplifier based on a dual-core fiber. *Opt. Lett.*, 21(5):330–332, Mar 1996. doi: 10.1364/OL.21.000330. URL <http://ol.osa.org/abstract.cfm?URI=ol-21-5-330>. 34
- [4] S. Klaiman, U. Günther, and N. Moiseyev. Visualization of Branch Points in PT-Symmetric Waveguides. *Physical Review Letters*, 101(8):080402, August 2008. doi: 10.1103/PhysRevLett.101.080402. 34
- [5] Jiří Čtyroký, Vladimír Kuzmiak, and Sergey Eyderman. Waveguide structures with antisymmetric gain/loss profile. *Opt. Express*, 18(21):21585–21593, Oct 2010. doi: 10.1364/OE.18.021585. URL <http://www.opticsexpress.org/abstract.cfm?URI=oe-18-21-21585>. 34
- [6] Henri Benisty, Aloyse Degiron, Anatole Lupu, André De Lustrac, Sébastien Chénais, Sébastien Forget, Mondher Besbes, Grégory Barbillon, Aurélien Bruyant, Sylvain Blaize, and Gilles Lérondel. Implementation of pt symmetric devices using plasmonics: principle and applications. *Opt. Express*, 19(19):18004–18019, Sep 2011. doi: 10.1364/OE.19.018004. URL <http://www.opticsexpress.org/abstract.cfm?URI=oe-19-19-18004>. 34
- [7] Vladimir V. Konotop, Valery S. Shchesnovich, and Dmitry A. Zezyulin. Giant amplification of modes in parity-time symmetric waveguides. *Physics Letters A*, 376(42):2750 – 2753, 2012. ISSN 0375-9601. doi: <https://doi.org/10.1016/j.physleta.2012.07.027>. URL <http://www.sciencedirect.com/science/article/pii/S0375960112008584>. 34
- [8] H. Benisty, C. Yan, A. Degiron, and A. Lupu. Healing near-pt-symmetric structures to restore their characteristic singularities: Analysis and examples. *Journal of Lightwave Technology*, 30(16):2675–2683, Aug 2012. ISSN 0733-8724. doi: 10.1109/JLT.2012.2205222. 34, 37
- [9] Ngoc B Nguyen, Stefan A Maier, Minghui Hong, and Rupert F Oulton. Recovering parity-time symmetry in highly dispersive coupled optical waveguides. *New Journal of Physics*, 18(12):125012, 2016. URL <http://stacks.iop.org/1367-2630/18/i=12/a=125012>. 34, 37
- [10] N. Asger Mortensen, P. A. D. Gonçalves, Mercedeh Khajavikhan, Demetrios N. Christodoulides, Christos Tserkezis, and Christian Wolff. Fluctuations and noise-limited sensing near the exceptional point of parity-time-symmetric resonator systems. *Optica*, 5(10):1342–1346, Oct 2018. doi: 10.1364/OPTICA.5.001342. URL <http://www.osapublishing.org/optica/abstract.cfm?URI=optica-5-10-1342>. 34

- [11] Xu-Lin Zhang, Xi-Bin Wang, and C. T. Chan. Switching terahertz waves using exceptional points. *Phys. Rev. Applied*, 10:034045, Sep 2018. doi: 10.1103/PhysRevApplied.10.034045. URL <https://link.aps.org/doi/10.1103/PhysRevApplied.10.034045>. 34
- [12] Kun Ding, Guancong Ma, Z. Q. Zhang, and C. T. Chan. Experimental demonstration of an anisotropic exceptional point. *Phys. Rev. Lett.*, 121:085702, Aug 2018. doi: 10.1103/PhysRevLett.121.085702. URL <https://link.aps.org/doi/10.1103/PhysRevLett.121.085702>. 34
- [13] Anatole Lupu, Henri Benisty, and Aloyse Degiron. Switching using pt symmetry in plasmonic systems: positive role of the losses. *Opt. Express*, 21(18):21651–21668, Sep 2013. doi: 10.1364/OE.21.021651. URL <http://www.opticsexpress.org/abstract.cfm?URI=oe-21-18-21651>. 34, 36, 38
- [14] Anatole Lupu, Vladimir V Konotop, and Henri Benisty. Optimal pt-symmetric switch features exceptional point. *Scientific reports*, 7(1):13299; 13299–13299, 10 2017. doi: 10.1038/s41598-017-13264-9. URL <https://www.ncbi.nlm.nih.gov/pubmed/29038509>. 34, 39
- [15] S. Francois, S. Fouchet, N. Bouadma, A. Ougazzaden, M. Carre, G. Herve-Gruyer, M. Filoche, and A. Carencu. Polarization-independent filtering in a grating-assisted horizontal directional coupler. *IEEE Photonics Technology Letters*, 7(7):780–782, July 1995. ISSN 1041-1135. doi: 10.1109/68.393204. 34, 38
- [16] H. Kogelnik and R. Schmidt. Switched directional couplers with alternating delta-beta. *IEEE Journal of Quantum Electronics*, 12(7):396–401, July 1976. ISSN 0018-9197. doi: 10.1109/JQE.1976.1069190. 36
- [17] C. Wu, C. Rolland, N. Puetz, R. Bruce, K. D. Chik, and J. M. Xu. A vertically coupled in-gaasp/inp directional coupler filter of ultranarrow bandwidth. *IEEE Photonics Technology Letters*, 3(6):519–521, June 1991. ISSN 1041-1135. doi: 10.1109/68.91020. 37
- [18] A. Lupu, H. Sik, A. Mereuta, P. Boulet, M. Carre, S. Slempek, A. Ougazzaden, and A. Carencu. Three-waveguide two-grating codirectional coupler for $1.3/\text{sup} - //1.3/\text{sup} + //1.5 / \text{spl} \mu/\text{m}$ demultiplexing in transceiver. *Electronics Letters*, 36(24): 2030–2032, Nov 2000. ISSN 0013-5194. doi: 10.1049/el:20001402. 38
- [19] A. Lupu, P. Win, H. Sik, P. Boulet, M. Carre, S. Slempek, and A. Carencu. Tunable filter with box-like spectral response for $1.28/1.32 / \text{spl} \mu/\text{m}$ duplexer application. *Electronics Letters*, 35(2):174–175, Jan 1999. ISSN 0013-5194. doi: 10.1049/el:19990131. 38, 39

Chapter 3

Design And Fabrication

This chapter is dedicated to the implementation of the Parity-Time symmetric (PTS) grating, and the key aspects that had to be dealt while its design and fabrication. The philosophy of this work was to use tools and processes used by opto-electronic components manufacturer to realize PTS DFB lasers, and to compare them to existing technological solutions available on the market.

3.1 Design of PTS DFB laser

3.1.1 Technical Choices

In this section, I talk about the choices made prior to the fabrication, and their link with the lasers technical specifications that we anticipated. As our motivation here is to fabricate a practical device, the objective is to make use of market technologies and their associated manufacturing process. Technical choices and design were driven by the idea that our lasers should correspond to the technological standards available in the industry, and be compatible with existing platforms.

The ingame of the design of a Parity-Time Symmetric (PTS DFB) structure is to be able to create strong modulation in the real and imaginary part of the index simultaneously. To do that, different strategies have been reported. Some of them use grating bearing on the top of the guiding ridge or ring [1], coupled structures [2, 3] or use the induced variation of real and imaginary part of index by a variation of guiding ridge width [4]. Our approach however is based on the consideration that PTS grating can be made of the association of a conventional index coupled and a conventional gain coupled Distributed FeedBack (DFB) laser with specific phase relation. To construct PTS DFB laser we thus need to be able to fabricate index and gain coupled DFB lasers, and integrate both gratings together.

A critical step in the realization of micro or nanometric opto-eletronic components lies in the choice of material to fabricate them. Several options can be considered in the design of a single-mode laser cavity using Bragg grating: from external to distributed feedback reflectors, using edge or vertical emitting lasers and with a buried, vertical or lateral grating. The active structures, representing the amplification medium can be quantum well, quantum dots or quantum dash from III-V semiconductor based compounds.

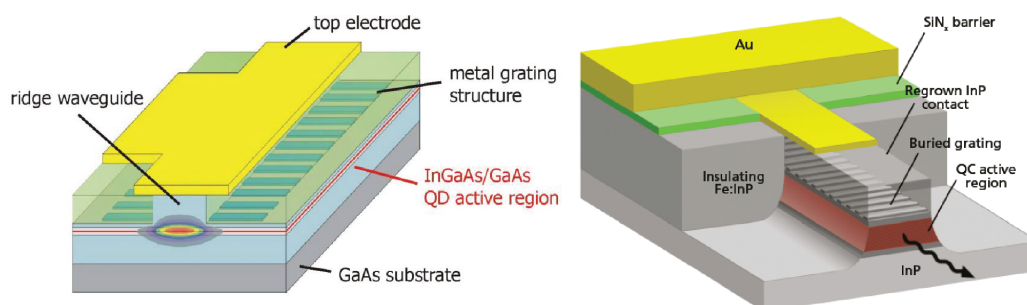


Fig. 3.1. Presentation of 2 DFB lasers architectures: Laterally coupled (upper left), Buried Ridge Structure (upper right)

The C2N has strong experience in the design of DFB lasers in the InP/InGaAsP and GaAs/AlGaAs material systems, particularly in the fabrication of laterally coupled edge emitting

ridge structures. This design is widespread in the realm of semiconductor lasers for optical networks even though the predominant DFB technology in use for long range telecommunication networks is the Buried Ridge Structures (BRS) lasers. As this type of laser requires epitaxial re-growth, it is much more complicated to fabricate than lateral grating structures. Furthermore, because of its design layout, the implementation of PTS grating seems more complicated than for a DFB based on a lateral grating.

Whereas a two quantum well layers is among the least feedback resistant type of structures, our approach is here to enhance the effects of different laser cavities, and to demonstrate the specificity of PTS structure over conventional DFB laser. To enhance the coupling between the mode traveling inside the cavity and the lateral grating, we designed the structure for the grating to be as close as possible to the active region, where the mode is guided.

An interesting feature of the PTS DFB laser that we are here willing to prove is their great resistance under external feedback. As the purpose of this work is to demonstrate effects of PTS on semiconductor lasers, we didn't opt for an epitaxial structure known for its good resistance to external feedback, as can be quantum dots or multiple quantum well structures, but rather for a two quantum well structure. This way the confinement should be low enough to enhance the effects of the lateral grating inside the laser cavity.

3.1.2 Simulation and Design

N° Layer	Function	Compound	Thickness (nm)	Doping
0	Buffer	InP	>1000	Si
1	SCH	InGaAsP 1,17	200	nid
2	QW	InGaAsP	6	nid
3	Barrier	InGaAsP 1,17	20	nid
3	QW	InGaAsP	6	nid
3	SCH	InGaAsP 1,17	200	nid
4	Top	InP	100	Be
5	SCH	InGaAsP 1,17	35	Be
6	Cladding	InP	1500	Be
7	Contact	InGaAs	300	Be

Table 3.1. Epitaxial structure of the material used for fabrication, *nid* stands for "non intensional doping"

The active structure used for this work is presented in table 3.1. It was grown by Gas Source Molecular Beam Epitaxy (GSMBE), and is composed of two III-V quaternary compound quantum wells, formed to present an optimal bandgap at $1.55\mu\text{m}$. The two quantum wells are surrounded by quaternary layers of different bandgap to ensure confinement of the amplified mode, and a P-N junction is formed by n and p doping in InP cladding. By etching the InP cladding covering the active region, the effective index of the structure will be altered, forming a higher index region in which the wave will be guided. As for many technological reasons the spectral gain of the material can slightly change, three lasers of different Bragg wavelength were designed. This way we ensure to have Bragg gratings in the spectral region of maximum gain. The chosen wavelength were $1.53\mu\text{m}$, $1.55\mu\text{m}$ and $1.57\mu\text{m}$. An additional wavelength was also added in order to get results in a spectral domain outside of the material bandgap, to measure transmission and reflection of the grating.

As stated in the previous section, the PTS DFB lasers can be seen as the combination of a gain coupled DFB laser and an index coupled DFB laser, bringing respectively the gain/loss modulation and the refractive index modulation. The second one can be brought by a variation of the width of the guiding ridge, inducing a change in the effective index seen by the mode through the propagation. The second modulation can be achieved by an array of metal stripes lying on each sides of the ridge, absorbing part of the mode that overlap with the conductive material. As mentioned in the previous chapter, the condition of PT-symmetry stipulates that index and gain/loss modulation must be shifted by quarter of a period. This requires a stringent alignment between the fabrication steps, which is fortunately feasible using electron beam lithography. For this reason, and because of the feature size of the gratings, the fabrication process is very challenging. As both gratings need to be of the same period to satisfy PT symmetry, it is only necessary to compute the Bragg grating period for one of the two gratings. For sake of simplicity, and because the real part of effective index is sparsely impacted by the action of the metallic grating, the index grating was designed first and the loss grating then added.

To evaluate the amplitude of effective index modulation, we simulated the structure using Tempsele simulation software. A simplified model of plane wave was used here, while still computing the effective indices through a modal method. The simulations were done for three grating amplitudes (A): 250nm, 500nm and 1 μ m. The average width of the ridge was taken equal to 2 μ m to achieve single transversal mode, the width of the large and narrow parts of the ridge were respectively: 1.750 μ m/2.250 μ m; 1.500 μ m/2.500 μ m and 1 μ m/3 μ m. The input indices of the software were based on the work of Broberg et al. on the measurement of InGaAsP layers in the transparent region [5], the results of the simulation are represented in figure 3.2.

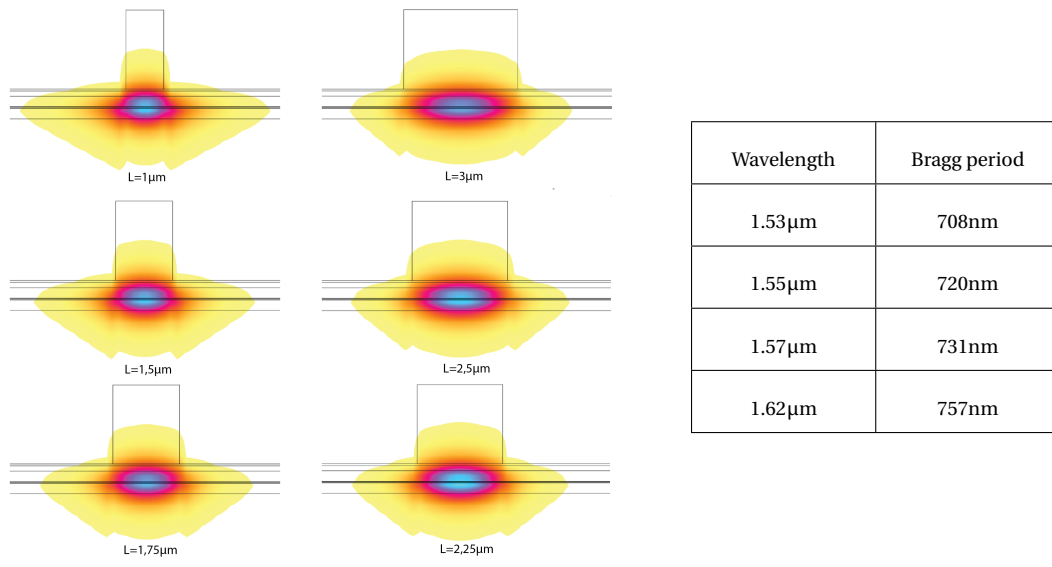


Fig. 3.2. Simulation results of effective index variation

With this work we were able to put in relation the width variation of the ridge with the associated index variation. The results obtained for the effective index associated to their width variation of the ridge are presented in table 3.2. As the average width was kept at 2 μ m, the average effective indices turn to be approximately constant with the different width variations. The effective index of a 2 μ m width waveguide built within our epitaxial structure is 3.229. Once this average effective index known, we are able to compute the

Bragg grating period, given by equation 1.1 of chapter 1. Results are presented in table 3.2.

	A=250nm	A=500nm	A=1 μ m
$\lambda=1.53\mu\text{m}$	$2.618\cdot 10^{-3}$	$5.307\cdot 10^{-3}$	$10.948\cdot 10^{-3}$
$\lambda=1.55\mu\text{m}$	$2.830\cdot 10^{-3}$	$5.737\cdot 10^{-3}$	$11.819\cdot 10^{-3}$
$\lambda=1.57\mu\text{m}$	$2.934\cdot 10^{-3}$	$5.946\cdot 10^{-3}$	$12.224\cdot 10^{-3}$
$\lambda=1.62\mu\text{m}$	$3.200\cdot 10^{-3}$	$6.478\cdot 10^{-3}$	$13.240\cdot 10^{-3}$

Table 3.2. Simulation results of effective index variation

Because the trenches of the gratings are taking lateral space, 1 μ m amplitude grating would put the metallic grating further away, and therefore bring the risk to have no overlap between the guided mode and the second grating, bringing the gain modulation. The amplitude of 500nm is here a better trade off between grating strength and favorable distance from guided mode to metallic grating.

The precision of the Bragg wavelength computed here will be controlled experimentally by the measure of the lasers spectra, and the coupling coefficient of both loss and index gratings will be evaluated through with the associated photonic bandgap, measured in transmission and reflection.

No further investigations are required to calculate the Bragg period of the gain grating. Indeed, the PT-symmetric condition requires that index and gain modulations periods must be equal, and phase shifted from a quarter of a period. The assumption was made that the effective gain modulation would be perfectly in phase with the metallic grating, and for this reason it was decided to take the same filling factor of 50% for its design.

3.1.3 Sample layout

One ambition of this work on Parity-Time Symmetry is to compare the performances of existing technology on DFB lasers, either index coupled or gain coupled, and demonstrate the assets of PTS for single frequency lasers. For this reason, the decision was taken to fabricate on the same wafer the two sorts of DFB lasers and test them under the same protocol. Index coupled DFB lasers were hence fabricated with the same index modulation than the PTS DFB lasers, whose design was exposed previously. To get a full insight of the influence of the grating amplitude, three different lasers were fabricated incorporating 250nm, 500nm and 1 μ m amplitude of index gratings. First and third order gain coupled DFB lasers were also appended to the fabrication process.

Figure 3.3 shows the principle of the fabrication sample layout. Because of misalignment issues that could occur between Electron Beam Lithography (EBL) steps during the fabrication process, and to be able to study the evolution of the lasers performances, it was decided to fabricate 8 gratings having both index and gain/loss modulations (a.k.a double gratings), with 8 different phase shifts. From this, the criticality of a deviation or misalignment during process is reduced as the correct PTS phase shift of 1/4 phase can be recovered. The double gratings DFB lasers thus have phase shift between 0 and $7\pi/8$ with a quarter phase shift increment. This also means that unidirectional behavior could be ideally probed from either side, as the lasers are then symmetric. As stated previously, lasers were designed at 4 wavelengths, i.e for each wavelength the whole set of conventional and

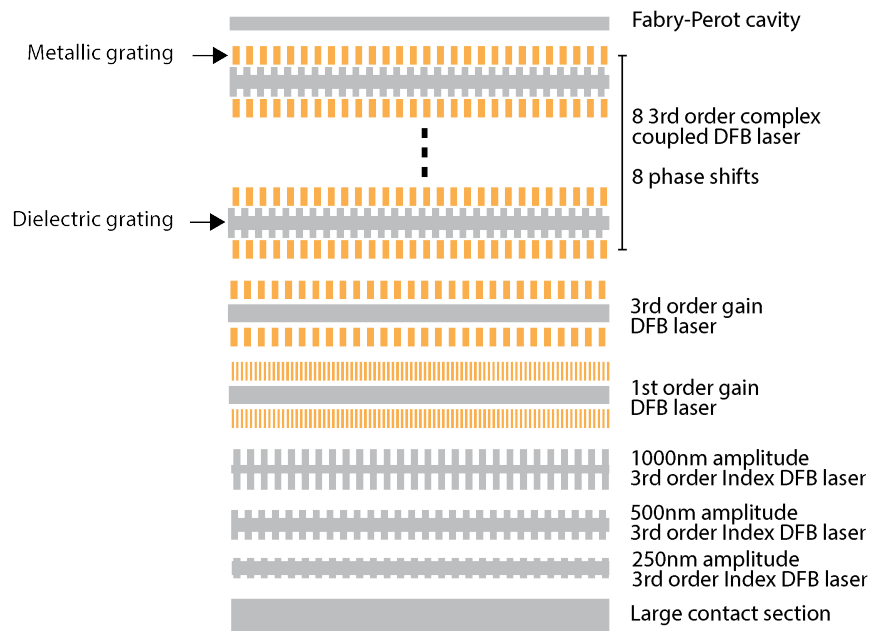


Fig. 3.3. Layout of the one section of the fabricated sample

PTS DFB lasers were fabricated, grouped in sections of same operating wavelength on the wafer. Broad-area and Fabry-Perot lasers were also fabricated to measure the electric and emission characteristics of the processed structures.

The wafer size used for this work was 2 inches, but only a quarter of a wafer was used for each fabrication run for saving reasons.

3.2 Fabrication of a PTS DFB laser

The fabrication of the PTS DFB lasers was performed in the clean room of C2N-Marcoussis with the expert help of the technical staff. To be in agreement with our willing to apply PTS symmetry to practical devices, the processing steps involved in the fabrication of the PTS DFB lasers were taken as close as possible to the industry building blocks. The final process flow includes several steps of Electron Beam Lithography (EBL), Reactive Ion Etching Capacitively Coupled Plasma (RIE CCP) and Inductively Coupled Plasma (ICP) etching and Physical Vapor Deposition (PVD) for metallic and dielectric deposition processes. The process flow gathering the fabrication steps required for the realization of our PTS DFB lasers is presented in figure 3.4.

The fabrication process includes specific steps for the implementation of gain or index coupled DFB lasers, which can be skipped for the realization of either gratings.

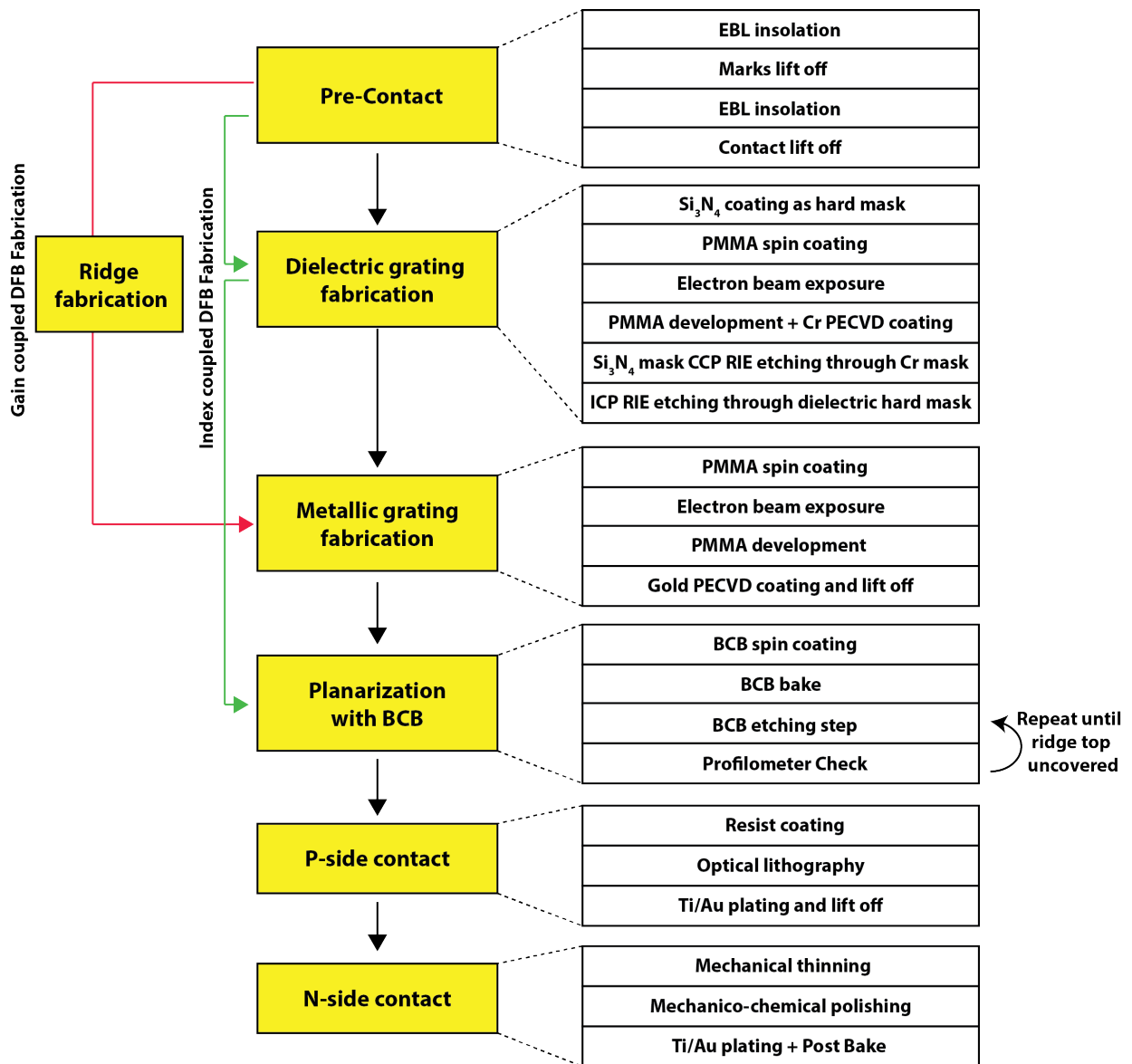


Fig. 3.4. Flow-chart of the fabrication process of PTS DFB lasers

3.2.1 Electron beam lithography

If UV optical lithography is a widely used fabrication process for micro-electronic and opto-electronic components, particularly appreciated for its robustness and rapidity, this technique is however unsuitable for the fabrication of our lasers. Indeed, the minimal feature size of tens nanometers and the need for flexibility of masks layout make it a bad candidate for our needs.

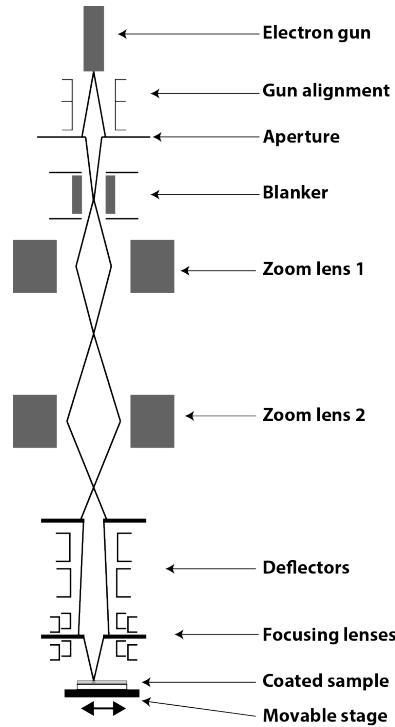


Fig. 3.5. Section of an electron-beam lithography machine

A common technique used for the fabrication of DFB lasers for optical networks is the Electron-Beam Lithography (EBL). This direct writing technology has become a fabrication standard and is very much valued for its high precision and control, its flexibility and the minimal feature size attainable. In EBL technique, an electron beam of several keV to hundreds of keV is created and focused on a specific resist. The beam is shaped by the action of electromagnetic lenses that accelerate and deflect electrons created by a Field Effect Gun (FEG). Electrons are then focused on the resist coated sample, lying on a movable stage.

Where the minimal printable size in optical lithography technique is limited by the wavelength of UV photons exposing the lithography resist, EBL will not suffer from diffraction as the electron wavelength is small enough, and will only be limited by the resist resolution. The electromagnetic lenses can deflect the beam within a distance of about $500\mu\text{m}$. While writing, the EBL machine will scan over one field and larger shifts will be achieved by moving the stage. This direct writing ability makes the EBL technology very flexible and useful for process development, we particularly took advantage of it for the development of test samples for ICP etching.

As EBL is computer controlled, the mask is designed using a Computer Assisted Design (CAD) software and processed from a dedicated software before being processed to satisfy the machine input format. Though EBL is a very powerful technique for the advantages

described earlier, the processing time is much more important than of optical lithography technique, in which the exposure duration is of the order of tens of seconds. This difference in processing time is significant because UV optical lithography is a fully planar parallel technology, while EBL is a sequential technology. As the processing time in EBL depends on the resolution and design complexity, the grating exposure steps were particularly long. However, by properly tuning the machine resolution, the processing time can be significantly decreased, but requires that all feature sizes must be compatible with the adapted resolution.

3.2.2 ICP etching development

One of the most critical step of our fabrication is the dry-etching processes. As discussed in the previous section, the EBL technique enables the writing of structures of small size with high precision. However, etching small sized structures down the wafer can be very challenging depending on the material, pattern shape and etching depth. Wet etching process can be used for laser ridge etching but is dependent of the crystal orientation. Dry etching, however, can be tune to be either anisotropic or isotropic independently to the crystal orientation and is widely used in the etching of gratings on InP substrates.

ICP etching mechanisms

Reactive Ion Etching (RIE) processes consist in transferring the layout of a mask to a substrate by chemically removing the substrate through the mask open areas. The denomination of “dry etching” is due to the gaseous phase of the species involved, on the contrary to wet etching where they are in liquid phase [6, 7, 8]. The etching mask is a film covering the substrate, that prevents reactions of chemical species with the surface under cover. For this reason the mask material should not be chemically etched by the by-products of the plasma involved to etch the III-V semiconductor. The selectivity of an etching process is defined by the ratio of the etching rate of the material by mask etching rate. The selectivity of the lithography resists being very low, a second mask (designated as "hard" mask) is required to be able to transfer the pattern to the material, that can itself be etched using RIE. Two technologies are used to initiate and maintain the plasma: the Capacity Coupled Plasma technique (CCP) and Induced Coupled Plasma (ICP). Dry etching processes are particularly used for the anisotropy of the etching mechanism. CCP and ICP etching technologies were used to etch respectively the Si_3N_4 hard mask and InP semiconductor.

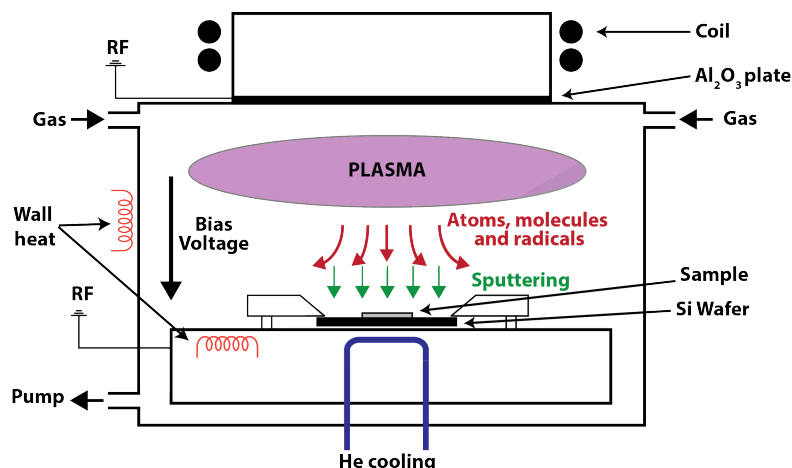


Fig. 3.6. Working principle of an RIE ICP etching reactor

In ICP etching techniques, the energy of the RF generator is transmitted to the plasma by induction through a dielectric plate. Electrons, ions and neutral species (atoms molecules and free radicals) are consequently present inside the plasma. Radical species react with the sample surface and form volatile compounds, evaporated subsequently from the surface. Electrons temperature inside the plasma involved in RIE techniques reaching 5 to 20 eV, and is categorized as “Cold plasma”. Plasma density for CCP technique is between 10^9 and 10^{10} cm^{-3} and between 10 and 100 cm^{-3} for ICP reactors.

Role of chemical species

During the etching process, the sample uncovered surface is gradually removed by the action of atoms, ions, molecules and free radicals. These species involved in plasma activity have distinct role in the dry etching mechanism,.

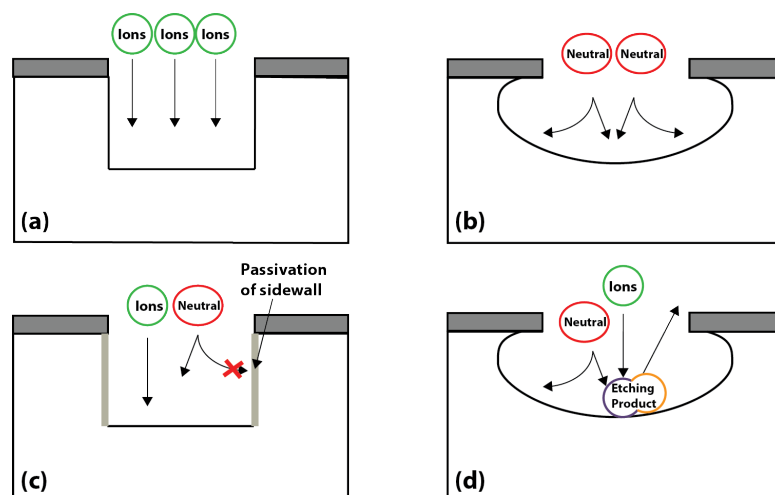


Fig. 3.7. Action of different species during etching

Sputtering (or ion bombardment) is a purely physical mechanism, non selective, in which the ionic species react inertly with the etched material. Because of its anisotropy, it can be useful for the etching of holes or high form factor structures. Involved in any RIE process with variable magnitudes, it has however restrictions: low etching rate, low selectivity and result in low surface quality.

Chemical etching is the results of chemical reactions between radicals at the substrate surface. In the vast majority of cases this mechanism is isotrope, with a rather high etching rate. Species draining has tendency to highly limit the chemical reaction, the etching pattern outline will thus impact chemical etching as it depends on the width of the etched structures.

Ion enhance chemistry is both a physical and chemical process. Chemical etching is improved by sputtering, as the flux of ions brings energy to the substrate surface, promoting molecules and neutral radicals mobility, thus improving etching reactions. Sputtering is furthermore necessary as it enhances the draining of species by its energetic contribution.

Passivation is due to the reaction between plasma species and the surface of the substrate. These reactions will form compounds, resulting in a protecting layer on the etching walls. This layer, sensitive to sputtering is however resistant to chemical

etching, and thus have the interesting ability to improve the anisotropy of the etching process.

Because of the draining of the active species as well as the isotropic effects of the chemical etching, the efficiency of the process will greatly depend on the design layout of the etched structure. Etching the substrate with a low surface roughness, square etched floors and high form factor is challenging.

ICP Parameters

The etching mechanisms described earlier can be tuned by changing the etching conditions through the ICP reactor parameters. Plasma density and composition and the action of chemical species will indeed be different depending on reactor pressure, ICP power, bias voltage, temperature and species flow.

The reactor pressure is directly fixing the mean free path of the species. A higher pressure will promote isotropic etching of the material. It can be worth noting that the flow of species will affect the minimum reachable pressure, as the efficiency of reactor pumping will depend on the amount of gas inside the chamber.

The ICP power will fix the energy of the species, specially the electrons, thus influencing the ionisation and dissociation rate. This impacts the density and radicals inside the reactor, and their energy. If the pressure is too important though, the mean free path is too short and the electrons energy is not sufficient to dissociate or excite. Further more with high gas flow the ICP power has to be stronger: gases will require more energy to be fully ionised.

Self-bias voltage . While the plasma is being nurtured by the ICP power, the species are deflected to the surface of the substrate and react with it. The self-bias is naturally created on the substrate to avoid plasma electron depletion.

The temperature is an important parameter as it will act as a catalyzer on the chemical reactions between etching gases and substrate. It allows the evaporation of by products of the plasma surface reactions.

The species flow will determine the quantity and ratio of chemical species reacting with the surface substrate.

It is reported [9] that high (>250°C) substrate temperature would foster chemical-surface activation, improve InP desorption and reduce RIE lag, whereas ion bombardment will be predominant for lower (190°C/230°C) substrate temperature. Few tests on our equipment demonstrated that temperatures between 150°C and 200°C was enough for a correct desorption of InP, and compatible with the etching we were willing to make.

3.2.3 Etching of InP corrugated grating

Because of the wide use of InP substrate in telecommunication photonic devices, the etching of InP structures using ICP has been investigated for a long time. Investigations about the etching of ridges [10, 11, 12], photonic crystals [13, 9, 12, 14, 15, 16, 17] or other structures [12, 18] have been reported.

The PTS DFB laser we are willing to fabricate is composed of a index grating of short period, present in the form of corrugations, for which the dry etching process can be challenging. We are here facing three difficulties:

- the rectangular shape of the slots will bring non uniformity in the draining of species and compounds -
- the high aspect ratio (around 1:7), can be tough to reach while keeping squared etching floor at the bottom of the structure, to maximize the index contrast -
- the grating asymmetry is a very important impairment, as the isotropic etching mechanisms will not have the same magnitude in the interior of the slots than in the external area.

Because of these difficulties, it can be easier to etch the sample in two steps: one defining the grating openings (holes) and one constructing the central ridge. Whereas dividing the etching in two steps seems to be an easy way to ease the etching process, it requires to run two EBL steps instead of one, increasing the risk of misalignment and thus of deformation of the grating shape. Before settling for one or the other strategy, we decided to steer the etching process development to both strategies by etching both rectangle holes and corrugated patterns. The mask layout principle is presented figure 3.8.

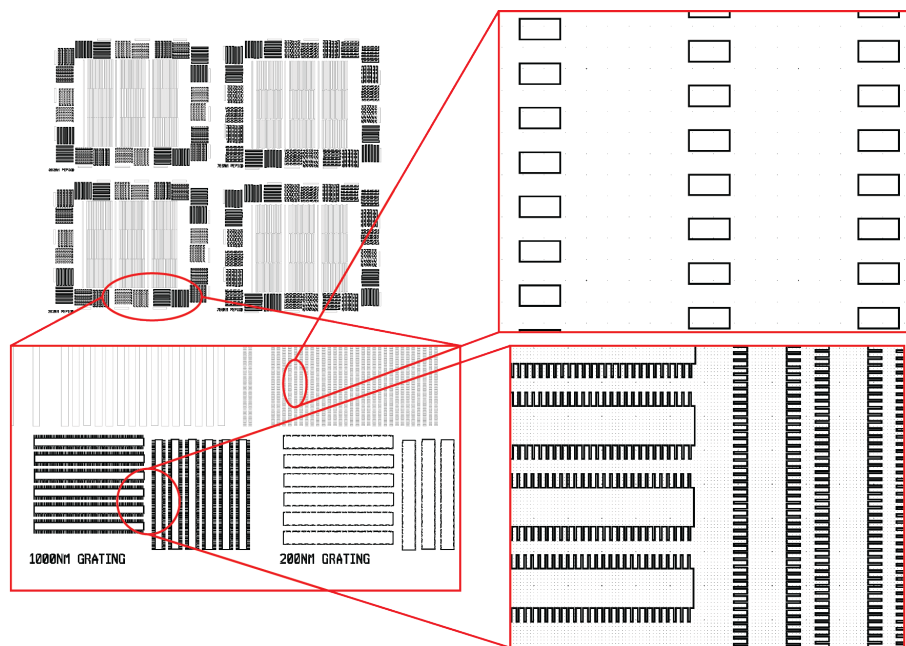


Fig. 3.8. Mask layout principle of the etching test samples: association of holes and corrugations

Naturally, hole sizes and corrugation geometries corresponding to several design wavelengths and grating amplitudes were printed, to get the best insight of etching performances of the tested process. It is worth noticing here that the etching of a linear array of rectangle holes as is described in the two steps strategy is very similar to the etching of a linear photonic crystal. For this reason the etching tests were inspired from results in literature related to the etching of photonic crystals.

The etching of photonic crystals in InP substrate has long been of great interest for the achievement of compact Photonic Integrated Circuits (PCIs). Achievements have been reported in literature, particularly concerning the etching of micrometric photonic crystals using Cl_2 based ICP etching recipes. Chlorine is very often used in the etching of InP

as it is a powerful reagent at low temperature. Under the action of a strong magnetic field, the Cl_2 double bond break, producing Cl^+ ions. As Cl^+ ions will lead to the isotropic desorption of InP, it is necessary to combine them with the action of sputtering, passivation or both in order to avoid undercut and improve surface roughness of the bottom and the sidewalls.

The investigations on an optimized recipe for the etching of our structure were first based on the study of four gas compositions: $\text{Cl}_2:\text{Ar}$ - $\text{Cl}_2:\text{H}_2:\text{O}_2$ - $\text{Cl}_2:\text{H}_2:\text{O}_2:\text{He}$ - $\text{HBr}:\text{O}_2:\text{He}$. For each composition, the temperature, RF power, bias voltage, internal pressure and species flow was slightly changed, in order to study the evolution of etching mechanisms during the process.

The addition of O_2 to the chlorine plasma will improve the dissociation and creation of Cl^+ by cracking Cl_2 [19, 13]. O_2 plays a role of passivation promoter, that will protect the sidewalls from etching. Chlorine radicals are thus consumed preferably at the bottom surface instead of sidewalls, resulting in improved anisotropy [13] and etch rate. Increasing the flux of dioxygen however leads to increase of passivation at the bottom, and as a consequence to micromasking and decrease in etching rate.

H_2 and Ar species will here improve the dissociation of Cl_2 , thus leading to an increased presence of chlorine radicals. However, those two elements will have interesting effect of removing etch products in the vertical direction as they take important part on the ion bombardment, improving anisotropy. Helium is a neutral gases, and its addition to the etching recipe is strictly in order to dilute the reactive elements, tune the reaction with the substrate and enhance the surface quality of the etched structures. As a starting point, gases ratio were decided on existing results and observations of the etching made on the ICP reactor.

3.2.4 Development of the ICP etching process

The sample was stuck and thermally coupled to a 4 inched silicon wafer with thermal paste, itself clamped inside the ICP reactor and thermally monitored. The reaction of silicon with halogen gases can have positive influence on the plasma chemistry, and etching dynamics [20]. The hard mask was composed of Si_3N_4 deposited using PECVD, and etched with CCP RIE process after lift off of chromium mask on PMMA (Polymethyl Methacrylate, EBL resist used here), previously exposed with EBL.

Cl_2/Ar plasma

We started our work on ICP etching with the test of a $\text{Cl}_2:\text{Ar}$ recipe. To improve the evacuation of etched products and improve anisotropy, the parameters tested were the bias voltage and pressure. Temperature was chosen in the high range of the reactor, with a low pressure to avoid undercuts and improve surface roughness of the bottoms and sidewalls. Results are presented in figure 3.9.

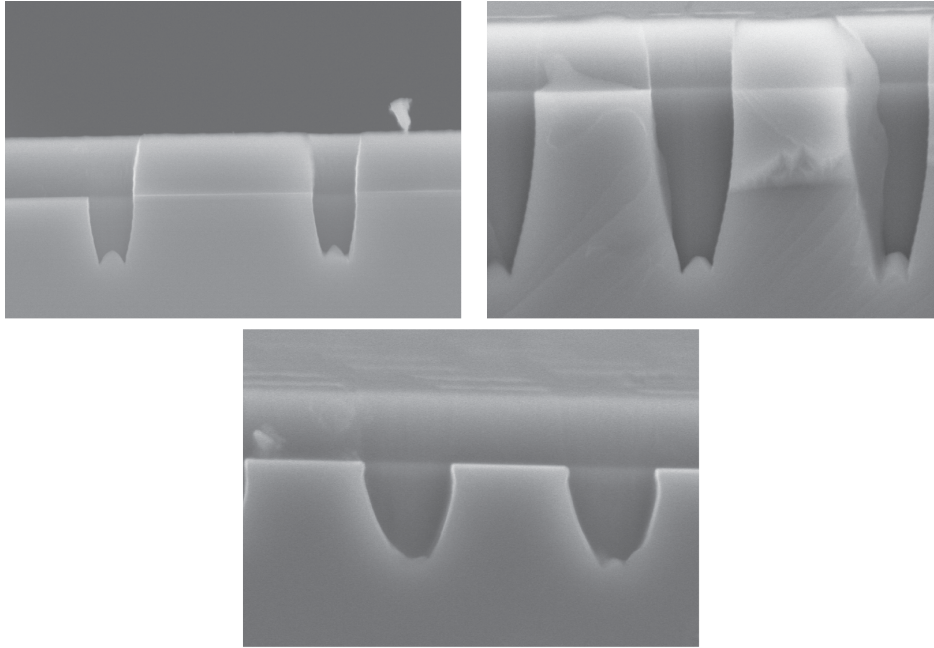


Fig. 3.9. Pictures of holes etched with $\text{Cl}_2:\text{Ar}$ etching process. The width of the holes are 500nm (top) and 1000nm (bottom).

Using this set of parameters, we noticed an effect of trenching, unveiled in the bottom of the holes by the presence of a bowing shape. This effect comes from the charging of the sidewalls that deflect the ions to both sides of holes. Consequently the sidewalls will be slightly tilted and bottom will be bowed. Trenching could be slightly reduced using a lower bias voltage and increasing the pressure. However an increase in pressure also led to an increase in chemical etching rate of the sidewalls, increasing under etching and isotropy.

From these observation, the decision was taken to introduce a passivation gas in order to increase the amount of Cl_2 while still being able to control the etching and its anisotropy.

In the following sections, the results presented were obtained by a single ICP etching step process. Indeed, with the development of three and four gases processes, it was considered that the misalignment risks were to high with regards to the attainable profile obtained from a single step process.

$\text{Cl}_2:\text{H}_2:\text{O}_2$ plasma

A first step was to adjust the ratio of chlorine and oxygen, which will define the process of chemical etching, impacting the anisotropy, etching rate and surface roughness. The gas ratio between Cl_2 and H_2 was kept at 1:2, and the flow of oxygen started with 1 sccm. By monitoring the machine throttle position, the pressure was taken as low as possible, around 0,9 mTorr, enhancing the etching residuals draining. ICP power and bias voltage were taken at 800W and -200V to fully ionize the plasma and obtain a high etching rate, and thus improve anisotropy.

The first test, presented on figure 3.10, demonstrated a high etching rate of around 500 nm/min, important micromasking, slight under etch and poor surface roughness. In order to correct the micromasking, it was decided to increase the temperature while keeping other parameters constants.

If this second test improved the micromasking at the bottom of the holes, the isotropy

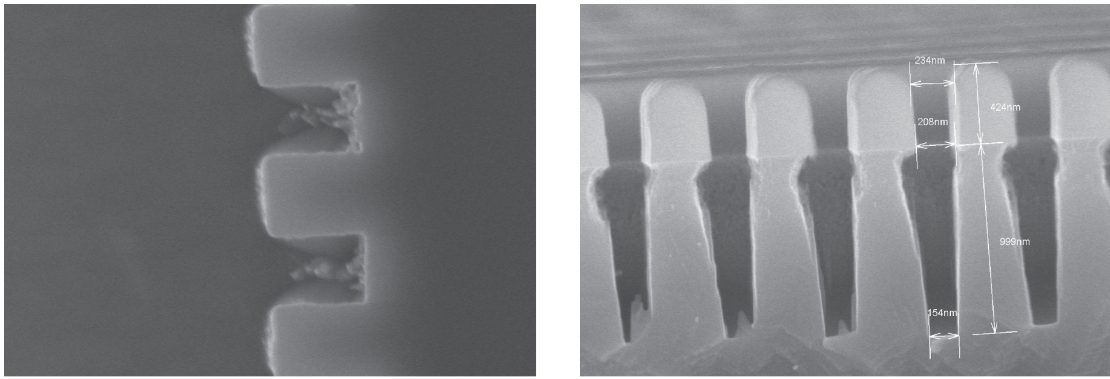


Fig. 3.10. First etch test on $Cl_2:H_2:O_2$ recipe. The periode of the structure on the left picture is 720nm, the width of the holes on the right is approximately 220nm.

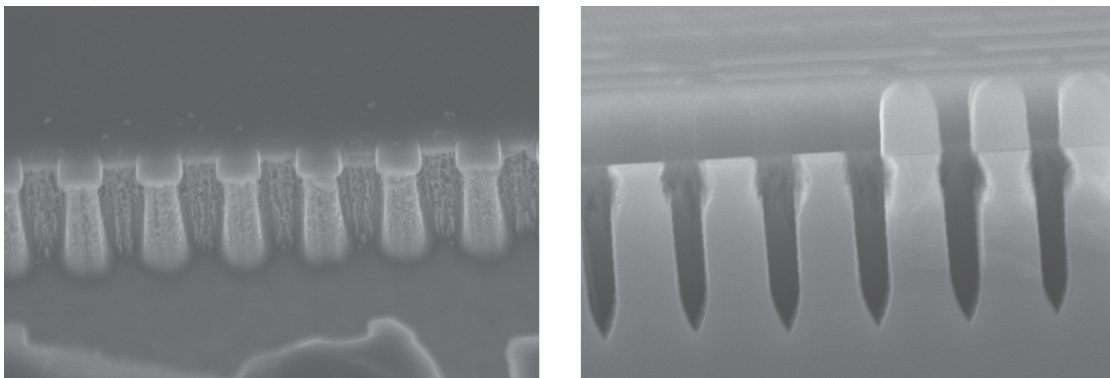


Fig. 3.11. Second etch test on $Cl_2:H_2:O_2$ recipe. The periode of the structure on the left picture is 720nm, the width of the holes on the right is approximately 220nm.

of the process was raised (see figure 3.11). It seemed as the augmentation in temperature also boosted chemical reactions on the sidewalls, increasing the under etching of the structures, degrading its surface roughness and geometric form. The micromasking was thus reduced at the cost of surface quality though keeping a quite good anisotropy and verticality. It then seemed important to reduce the efficiency of the chemical etching, to promote passivation and decrease surface roughness.

By dividing the gases flow by a factor of 2, we were able to observe interesting results with vertical and relatively smooth sidewalls and reduced under etch. However, it seems that chemical etching is still predominant at the beginning of the etching as structures are rough at their top. The sidewalls verticality and the relative squared angles at the bottom the gratings demonstrated an improvement in the anisotropy of the etching and was a great sign that we were getting closer to our objective. Nevertheless we still had to improve the etching inside the trenches of the grating, in which the results were not yet satisfying (see figure 3.12). These areas are the most difficult to etch as the reactive species will not have access to the end of the trenches directly.

It was then decided to increase the pressure and bias voltage in order to improve the chemical reaction inside the grating openings. To avoid surface quality degradation in the other parts of the grating it was decided to dilute gases using Helium.

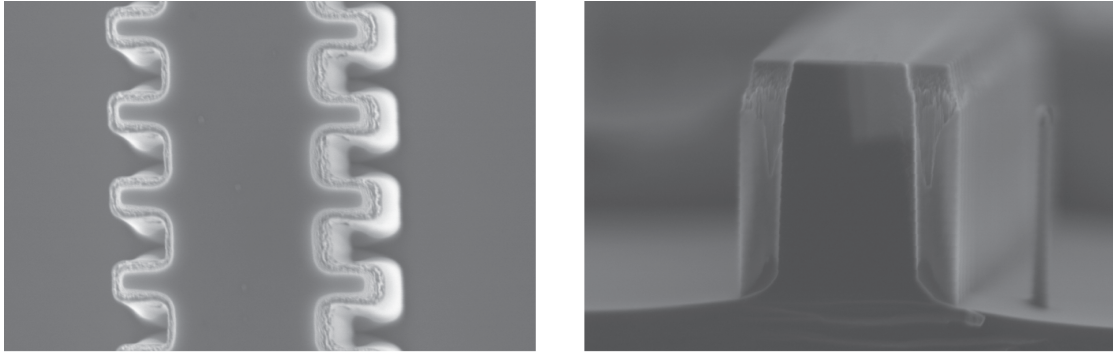


Fig. 3.12. Third and last etch test on $\text{Cl}_2:\text{H}_2:\text{O}_2$ recipe. The grating period is 720nm.

$\text{Cl}_2:\text{H}_2:\text{O}_2:\text{He}$ plasma

This recipe gave very interesting results, as it was the first one that could seriously be considered for the fabrication of our lasers. The pattern fidelity was very good, with square edges of the gratings corrugations (see figure 3.13). Cut views of the etched grating show a relatively smooth surface quality, as well as vertical sidewalls. The only downturn of this etching recipe was the slope at the bottom of the structure, in the inside of the trenches. It can again be explained by the asymmetry of the geometry, leading to a difficult access of the chemical species to these regions.

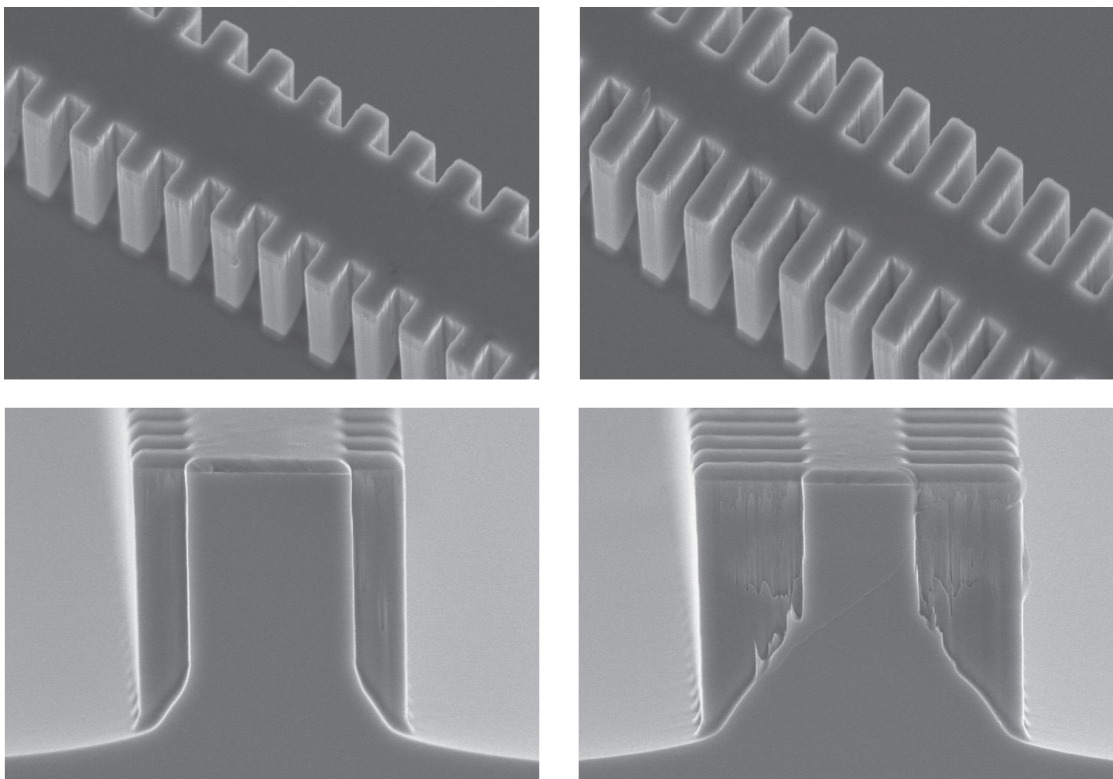


Fig. 3.13. First etch test on $\text{Cl}_2:\text{H}_2:\text{O}_2:\text{He}$ recipe. The grating period is 720nm, height is 2.4 μm .

From this working point, the variation of several parameters were studied, with the objective to reduce a little the roughness of sidewalls, and to flatten the slope at the bottom

inside the trenches. We played on the flow of gases, the pressure and the self-bias.

1. Increasing the flux of Helium improved the surface roughness and slightly reduced the slope inside the trenches (figure 3.14 (b)).
2. Reducing the flow of Chlorine and Hydrogen while keeping an 1:2 ratio gave interesting results on the etching of the structure, however the inside and outside of the trenches started to be polluted by micromasking effect (figure 3.14 (a)). This can be due to insufficient chemical etching and unremoved etch product redepositing on the substrate.
3. With the reduced amount Cl_2 and H_2 , reducing the flow of Oxygen leads to a better slope inside the trenches but created a second slope in the longitudinal direction (figure 3.14 (c)). The reason can be that the passivation is less effective in the bottom of the trench, causing a better etching and reducing trench in one direction. The appearance of the second slope might be due to re-deposition of etching products, unable to be evacuated.
4. From the initial gas flow, increasing the pressure gave interesting results, though displaying micromasking and degraded roughness inside trenches (figure 3.14 (d)). The pressure increase might act as chemical reaction promoter at the top of the grating, but also decrease the removal of etching products leading to micromasking.
5. Increasing the self-bias (related to the bias voltage) gave good results, with still presence of micromasking and degraded etching inside trenches (figure 3.14 (e)). The sharpness of the etching and its anisotropy were satisfying.
6. Increasing the pressure with higher bias power, very interesting results were observed. The grating corrugations started getting a round shaped edges. Though this is not ideal in our case, this process could be interesting for fabrication of DFB with cosine index profile (figure 3.14 (f)).

Eventually, satisfying results were obtained for processes (a), (d) and (e). The original process also had good balance between the isotrope attack of chemical etching, sidewalls passivation and ion bombardment, and presence of micromasking observed on the (d) and (e) etching recipes represent a risk for the etching of the functional sample. The particularly satisfying feature of the original and (a) recipes were the verticality of the sidewalls, square shape of the grating and the good surface quality inside the trenches. Though the bottom inside of the trenches were not etched with a good 90° angle, it could not be improved significantly while keeping good surface quality and sharp square etched grating.

The last gaz composition tried was a recipe incorporating HBr, O_2 and He. Very interesting results were obtained with these process parameters at C2N [10], and an interesting working point was found using this process.

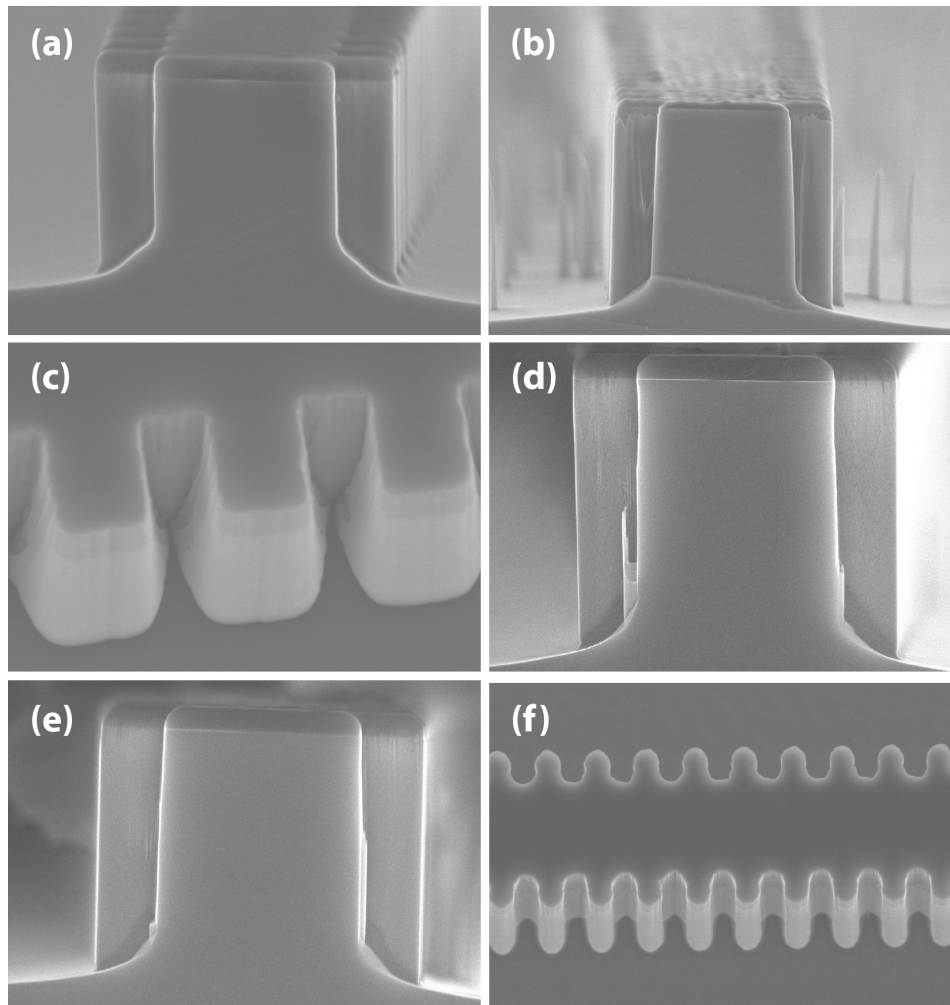


Fig. 3.14. Results on the development of a $\text{Cl}_2:\text{H}_2:\text{O}_2:\text{He}$ etching process. The grating period is 720nm, height for (a) is $2.2\mu\text{m}$, for (b) $2.45\mu\text{m}$, for (d) $2.2\mu\text{m}$, for (e) $2\mu\text{m}$.

HBr: O_2 :He plasma

If Cl-containing gas mixture are commonly used for the etching of InP and other III-V compounds, hydrogen bromide can be considered as an interesting alternate halogen gas for the etching of our gratings. Few results were reported on the work of etching recipe development using HBr based etching processes using different forms of RIE [7, 21, 22], some of which using ICP technique at room temperature [23] and higher temperatures [24], with positive results. The work on such ICP chemical composition was well-advanced at C2N, with good knowledge of the dynamics [25, 10, 26] and beautiful realizations [27], for this reason we decided to perform series of test using HBr as etching gas.

The working principle of the gas mixture tried is similar to some of which were introduced earlier with chlorine. Here the chemical reactive agent Cl_2 is replaced by HBr but the working principle remains the same: Bromine ions brings isotrope chemical etching with the support of Hydrogen ions, the etching anisotropy is balanced with passivation thanks to the presence of Oxygen, and the corrosion of the etching can be controlled from the dilution of the gases with Helium. For the first run, the gas flow were chosen similarly to the previously presented Cl_2 based processes.

The first results we obtained with this gas mixture were very satisfying, as can be seen in

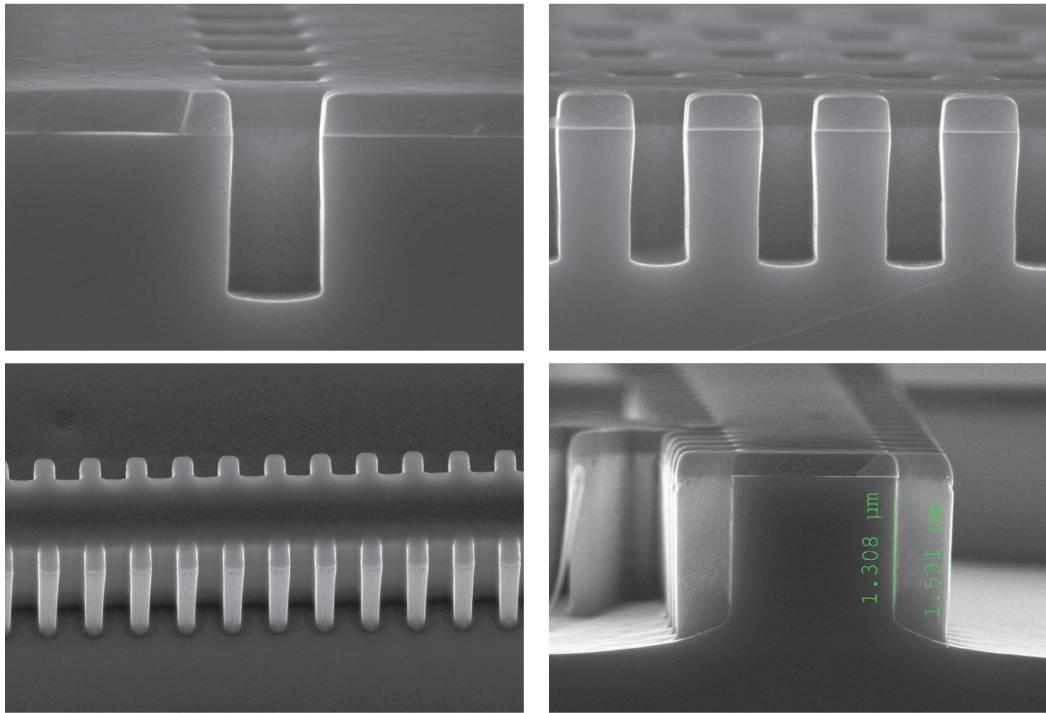


Fig. 3.15. First etch test on HBr:O₂:He recipe. The grating period is 720nm, the openings width are 500nm (top left) and 250nm (top right).

figure 3.15. The roughness was particularly improved, and the lateral slope at the foot inside the trench was improved. The results are presented in figure 3.15.

To get the sharpest shape possible and lowest lateral slope, the effects of parameters and gas flow variation were investigated. Here are the results that could be observed:

1. Increasing the flow of HBr while keeping all parameters constant led to the apparition of over etching at the bottom of the grating. The roughness was increased on sidewalls as shown figure 3.16(a).
2. Reducing bias power led to the apparitions of trenches at the bottom the grating. This could be due to the deviation of ions by sidewalls, charged under the action of the species, and was amplified as the bias was not sufficient to accelerate them. Figure 3.16(b) shows results from this etching test.
3. Increasing HBr and He flow by a factor of 2 led to a bad surface quality and didn't improved much the grating geometry. Figure 3.16(c) is a picture of the etched structure from this test run.

From the entire etching test, the first HBr recipe gave the best results in terms of quality of the etched surface, verticality of sidewalls and lateral slope down the trench. Furthermore it seemed possible with these parameters to perform the index grating etching in one step only instead of using two consecutive masks as stated at the beginning of this study. To ensure that this slope at the bottom of the trench would give sufficient index modulation,

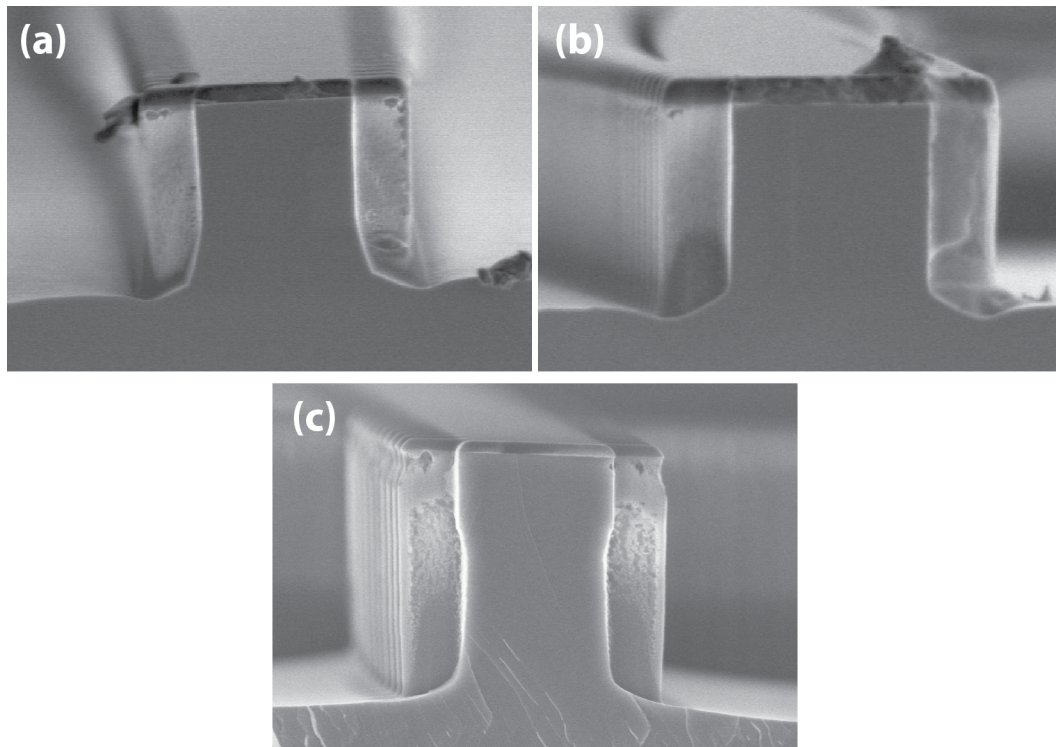


Fig. 3.16. Results on the development of HBr based etching process. The top structures have a height of $1.6\mu\text{m}$, bottom structure has a height of $2.4\mu\text{m}$

its effect on the effective index was simulated using the software previously presented for the computation of effective indices. It was found that the order of magnitude of the index modulation was kept unchanged, at 10^{-3} for a slope height as high as 400nm inside the trenches.

3.2.5 Etching of the index grating

The etching process of our sample was monitored using a laser interferometer. The principle is to use the refractive index variation among layers of our structure, and use them as reflectors. By pointing a laser on the surface while the sample is being etched, a modulation of the reflected wave amplitude can be observed. The principle of operation of this technique is shown figure 3.17 on the left. The phase difference between the reflected wave at the boundaries between layers 1 and 2 is $2n_1e(2\pi/\lambda)\cos(\theta)$, where n is the refractive index of the first layer, e its thickness, λ the wavelength of the laser used and θ the angle of incidence of the laser ray falling on layer 1. At normal incidence, the thickness of material etched during one period will thus be: $e_{etched}=\lambda/2n$.

The laser interferometry is here used to recognize the layer being etched. As the period of the amplitude modulation depend on the index of the material being etched, a change in this period can be noticed when passing from layer to layer during the etching process. This principle is shown on figure 3.17 on the right, with the associated layer etched.

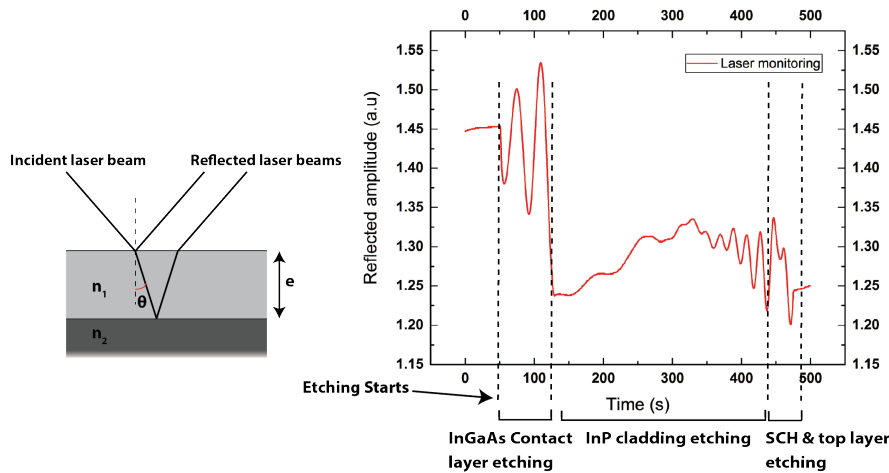


Fig. 3.17. Working principle of laser interferometer monitoring (left) and reflected amplitude variation pattern during the etching process (right). We used a laser with a wavelength of 645nm.

Pictures of the etched structure for the functional sample are presented figure 3.18. This was done using the initial HBr process with results presented on figure 3.15. The cladding was etched entirely, as well as the SCH and top layers, in order for the grating to be as close as possible to the active region, where the mode is guided. Observation from scanning electron microscopy shows that the roughness is satisfying and though we are not able to cleave the sample to see the inside of the trenches, we can see the outside shape is sharp and seems very well defined. Once the index grating etched, the metallic grating was exposed and deposited.

3.2.6 Fabrication of the metallic grating, and back-end

As stated previously, the relation of PT symmetry stipulates that real and imaginary part of the complex index must be respectively even and odd function of the propagation point. It was decided that gain/loss modulation of our Parity-Time Symmetric laser would be brought by the absorption of a metallic (gold) grating. This grating thus has to be in phase with the index grating bringing the refractive index modulation, and of similarly filling factor.

To implement the lateral metallic grating on PTS DFB lasers, Electron Beam Lithography technique was used to define the pattern in a PMMA resist, which was then developed to leave the grating stripes opened. A thin layer of Titanium was then coated to work as an adhesion promoter for the Gold layer that was later deposited. The metal layers were lifted off in solvent bath in areas still covered with the resist, after dissolution of the PMMA. Pictures of the resulting double gratings lasers are shown figure 3.19.

The last steps required to finalize the lasers are then to encapsulate them for protection, build the metallic contact on the top of them from which current will be injected, thin the InP back substrate to improve conduction, polish and build contact on the back side of the wafer for the cathode plating. One Rapid Thermal Annealing (RTA) was performed in order to defuse the contact and improve the electric conductivity. The diode is then electrically fully functional, but the lasers need to be cleaved in order to form cavities inside which stimulated emission will take place.

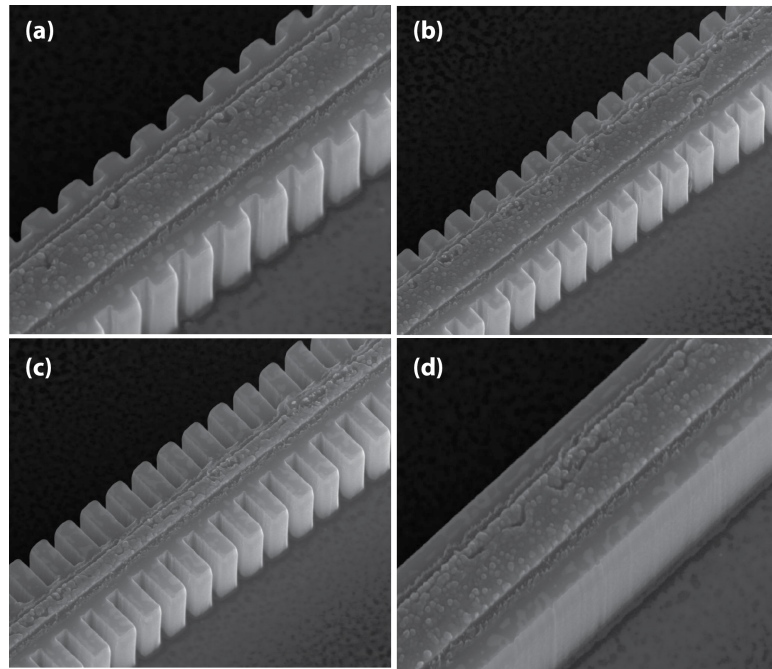


Fig. 3.18. Pictures of fabricated PTS DFB lasers after etching step: 250nm amplitude index grating (a), 500nm amplitude index grating (b), 1000nm amplitude index grating (c), straight waveguide (d)

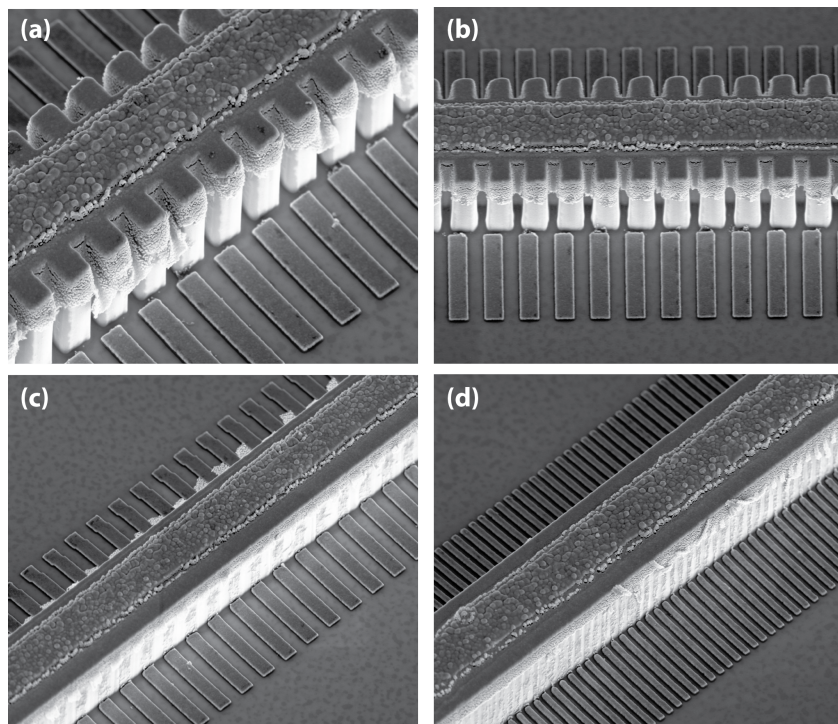


Fig. 3.19. Pictures of lasers after implementation of metallic gratings: PTS DFB lasers (a) & (b), third and first order gain coupled DFB laser (c) & (d) respectively. The grating period is 720nm.

3.3 Conclusions

Parity-Time symmetric Distributed Feedback lasers were designed and fabricated from two quantum well structure, composed of InP/InGaAsP compounds. As the approach is here to apply PT-symmetry to fabrication of practical devices, specific care was put into the simplicity of design and realization, as well as the compatibility of the fabrication with existing high-end manufacturing techniques. With that in mind the design of PTS DFB lasers consisted in the simulation of index modulation defined by the grating inside the InP/InGaAsP structure, at different wavelengths and for several grating amplitudes. Once the design validated, the Electron Beam Lithography mask was designed, composed of conventional gain and index coupled DFB lasers as well as multiple PTS DFB lasers with increasing phase shifts, in order to prevent possible misalignment that could occur during the consecutive EBL steps. Because of the geometry of its corrugations, the index grating is very challenging to etch. An ICP etching process was developed specifically for the implementation of the index grating. Chlorine-based recipes were developed, but the best results were obtained with Bromine-based chemistry. The metallic grating giving the loss modulation of the PTS DFB lasers was of the same period and filling factor as the index grating, it was fabricated using consecutive EBL and metallic PECVD deposition. From the first wafer desoxydation to the last back-end process, the fabrication process was performed in C2N cleanroom, with the help of the cleanroom staff.

3.4 Références

- [1] Liang Feng, Zi Jing Wong, Ren-Min Ma, Yuan Wang, and Xiang Zhang. Single-mode laser by parity-time symmetry breaking. *Science*, 346(6212):972–975, 2014. ISSN 0036-8075. doi: 10.1126/science.1258479. URL <http://science.sciencemag.org/content/346/6212/972>. 45
- [2] Liang Feng, Ye-Long Xu, William dos Santos Fegadolli, Minghui Lu, José Edimar Barbosa Oliveira, Vilson R Almeida, Yan-Feng Chen, and Axel Scherer. Experimental demonstration of a unidirectional reflectionless parity-time metamaterial at optical frequencies. *Nature materials*, 12 2:108–113, 2013. 45
- [3] Christian E. Rüter, Ramy El-Ganainy, Demetrios N. Christodoulides, Mordechai Segev, and Detlef Kip. Observation of parity–time symmetry in optics. *Nature Physics*, 6, 2010. 45
- [4] Choloong Hahn, Seok Ho Song, Cha Hwan Oh, and Pierre Berini. Single-mode lasers and parity-time symmetry broken gratings based on active dielectric-loaded long-range surface plasmon polariton waveguides. *Opt. Express*, 23(15):19922–19931, Jul 2015. doi: 10.1364/OE.23.019922. URL <http://www.opticsexpress.org/abstract.cfm?URI=oe-23-15-19922>. 45
- [5] B. Broberg and S. Lindgren. Refractive index of $\text{In}_1-x\text{Ga}_x\text{As}_y\text{P}_{1-y}$ layers and InP in the transparent wavelength region. *Journal of Applied Physics*, 55(9):3376–3381, 1984. doi: 10.1063/1.333377. URL <https://doi.org/10.1063/1.333377>. 47
- [6] S.J. Pearton. Dry-etching techniques and chemistries for III-V semiconductors. *Materials Science and Engineering: B*, 10(3):187 – 196, 1991. ISSN 0921-5107. doi: [https://doi.org/10.1016/0921-5107\(91\)90125-F](https://doi.org/10.1016/0921-5107(91)90125-F). URL <http://www.sciencedirect.com/science/article/pii/092151079190125F>. 52
- [7] S.J. Pearton, F. Ren, T.R. Fullowan, A. Katz, W.S. Hobson, U.K. Chakrabarti, and C.R. Abernathy. Plasma etching of III-V semiconductor thin films. *Materials Chemistry and Physics*, 32(3):215 – 234, 1992. ISSN 0254-0584. doi: [https://doi.org/10.1016/0254-0584\(92\)90203-K](https://doi.org/10.1016/0254-0584(92)90203-K). URL <http://www.sciencedirect.com/science/article/pii/025405849290203K>. 52, 61
- [8] Vincent M. Donnelly and Avinoam Kornblit. Plasma etching: Yesterday, today, and tomorrow. *Journal of Vacuum Science & Technology A*, 31(5):050825, 2013. doi: 10.1116/1.4819316. URL <https://doi.org/10.1116/1.4819316>. 52
- [9] C. F. Carlström, R. van der Heijden, M. S. P. Andriess, F. Karouta, R. W. van der Heijden, E. van der Drift, and H. W. M. Salemink. Comparative study of Cl_2 , Cl_2/O_2 , and Cl_2/n_2 inductively coupled plasma processes for etching of high-aspect-ratio photonic-crystal holes in InP . *Journal of Vacuum Science & Technology B*, 26(5):1675–1683, 2008. doi: <http://dx.doi.org/10.1116/1.2968696>. URL <http://scitation.aip.org/content/avs/journal/jvstb/26/5/10.1116/1.2968696>. 54
- [10] S. Bouchoule, S. Azouigui, S. Guilet, G. Patriarche, L. Largeau, A. Martinez, L. Le Gratiet, A. Lemaitre, and F. Lelarge. Anisotropic and smooth inductively coupled plasma etching of III-V laser waveguides using HBr-O_2 chemistry. *Journal of The Electrochemical Society*, 155(10):H778–H785, 2008. doi: 10.1149/1.2965790. URL <http://jes.ecsdl.org/content/155/10/H778.abstract>. 54, 60, 61

- [11] S. Guilet, S. Bouchoule, C. Jany, C. S. Corr, and P. Chabert. Optimization of a cl₂-h₂ inductively coupled plasma etching process adapted to nonthermalized inp wafers for the realization of deep ridge heterostructures. *Journal of Vacuum Science & Technology B*, 24(5):2381–2387, 2006. doi: <http://dx.doi.org/10.1116/1.2348728>. URL <http://scitation.aip.org/content/avs/journal/jvstb/24/5/10.1116/1.2348728>. 54
- [12] Fouad Karouta. A practical approach to reactive ion etching. *Journal of Physics D: Applied Physics*, 47(23):233501, 2014. URL <http://stacks.iop.org/0022-3727/47/i=23/a=233501>. 54
- [13] C. F. Carlström, R. van der Heijden, F. Karouta, R. W. van der Heijden, H. W. M. Salemink, and E. van der Drift. Cl₂/o₂-inductively coupled plasma etching of deep hole-type photonic crystals in inp. *Journal of Vacuum Science & Technology B*, 24(1): L6–L9, 2006. doi: <http://dx.doi.org/10.1116/1.2151915>. URL <http://scitation.aip.org/content/avs/journal/jvstb/24/1/10.1116/1.2151915>. 54, 56
- [14] A. Berrier, M. Mulot, S. Anand, A. Talneau, R. Ferrini, and R. Houdré. Characterization of the feature-size dependence in ar/cl₂ chemically assisted ion beam etching of inp-based photonic crystal devices. *Journal of Vacuum Science & Technology B*, 25(1):1–10, 2007. doi: <http://dx.doi.org/10.1116/1.2402142>. URL <http://scitation.aip.org/content/avs/journal/jvstb/25/1/10.1116/1.2402142>. 54
- [15] P. Strasser, R. Wüest, F. Robin, D. Erni, and H. Jäckel. Detailed analysis of the influence of an inductively coupled plasma reactive-ion etching process on the hole depth and shape of photonic crystals in inp/ingaasp. *Journal of Vacuum Science & Technology B*, 25(2):387–393, 2007. doi: <http://dx.doi.org/10.1116/1.2712198>. URL <http://scitation.aip.org/content/avs/journal/jvstb/25/2/10.1116/1.2712198>. 54
- [16] F. Pommereau, L. Legouézigue, S. Hubert, S. Sainson, J.-P. Chandouineau, S. Fabre, G.-H. Duan, B. Lombardet, R. Ferrini, and R. Houdré. Fabrication of low loss two-dimensional inp photonic crystals by inductively coupled plasma etching. *Journal of Applied Physics*, 95(5):2242–2245, 2004. doi: <http://dx.doi.org/10.1063/1.1644630>. URL <http://scitation.aip.org/content/aip/journal/jap/95/5/10.1063/1.1644630>. 54
- [17] N. Sultana, Wei Zhou, Tim P. LaFave, and Duncan L. MacFarlane. Hbr based inductively coupled plasma etching of high aspect ratio nanoscale trenches in inp: Considerations for photonic applications. *Journal of Vacuum Science & Technology B*, 27(6):2351–2356, 2009. doi: <http://dx.doi.org/10.1116/1.3250263>. URL <http://scitation.aip.org/content/avs/journal/jvstb/27/6/10.1116/1.3250263>. 54
- [18] Wei Zhou, N. Sultana, and D. L. MacFarlane. Hbr-based inductively coupled plasma etching of high aspect ratio nanoscale trenches in gainasp/inp. *Journal of Vacuum Science & Technology B*, 26(6):1896–1902, 2008. doi: <http://dx.doi.org/10.1116/1.3010711>. URL <http://scitation.aip.org/content/avs/journal/jvstb/26/6/10.1116/1.3010711>. 54
- [19] E. L. Lim, J. H. Teng, L. F. Chong, N. Sutanto, S. J. Chua, and S. Yeoh. Inductively coupled plasma etching of inp with hbr / o₂ chemistry. *Journal of The Elec-*

- trochemical Society*, 155(1):D47–D51, 2008. doi: 10.1149/1.2801872. URL <http://jes.ecsdl.org/content/155/1/D47.abstract>. 56
- [20] S. Guilet, S. Bouchoule, C. Jany, C. S. Corr, and P. Chabert. Optimization of a cl_2 -h₂ inductively coupled plasma etching process adapted to nonthermalized inp wafers for the realization of deep ridge heterostructures. *Journal of Vacuum Science & Technology B: Microelectronics and Nanometer Structures Processing, Measurement, and Phenomena*, 24(5):2381–2387, 2006. doi: 10.1116/1.2348728. URL <https://avs.scitation.org/doi/abs/10.1116/1.2348728>. 56
- [21] S. J. Pearton, F. Ren, and C. R. Abernathy. Temperature-dependent dry etching characteristics of iii-v semiconductors in hbr- and hi-based discharges. *Plasma Chemistry and Plasma Processing*, 14(2):131–150, Jun 1994. ISSN 1572-8986. doi: 10.1007/BF01465743. URL <https://doi.org/10.1007/BF01465743>. 61
- [22] J. M. Rossler, Y. Royter, D. E. Mull, W. D. Goodhue, and C. G. Fonstad. Bromine ion-beam-assisted etching of inp and gaas. *Journal of Vacuum Science & Technology B: Microelectronics and Nanometer Structures Processing, Measurement, and Phenomena*, 16(3):1012–1017, 1998. doi: 10.1116/1.590060. URL <https://avs.scitation.org/doi/abs/10.1116/1.590060>. 61
- [23] S. Vicknesh and A. Ramam. Etching characteristics of hbr-based chemistry on inp using the icp technique. *Journal of The Electrochemical Society*, 151(12):C772–C780, 2004. doi: 10.1149/1.1812731. URL <http://jes.ecsdl.org/content/151/12/C772.abstract>. 61
- [24] Mark Dineen Ligang Deng, Goodyear L. Andrew. Icp etching of inp and related materials using photoresist as mask. volume 5280, pages 5280 – 5280 – 6, 2004. doi: 10.1117/12.520922. URL <https://doi.org/10.1117/12.520922>. 61
- [25] S. Bouchoule, S. Azouigui, G. Patriarche, S. Guilet, L. le Gratiot, A. Martinez, F. Lelarge, and A. Ramdane. Processing of inp-based shallow ridge laser waveguides using a hbr icp plasma. In *2007 IEEE 19th International Conference on Indium Phosphide Related Materials*, pages 218–221, May 2007. doi: 10.1109/ICIPRM.2007.381162. 61
- [26] S. Bouchoule, L. Vallier, G. Patriarche, T. Chevolleau, and C. Cardinaud. Effect of cl_2 - and hbr-based inductively coupled plasma etching on inp surface composition analyzed using in situ x-ray photoelectron spectroscopy. *Journal of Vacuum Science & Technology A*, 30(3):031301, 2012. doi: 10.1116/1.3692751. URL <https://doi.org/10.1116/1.3692751>. 61
- [27] Guillaume Crosnier, Dorian Sanchez, Alexandre Bazin, Paul Monnier, Sophie Bouchoule, Rémy Braive, Grégoire Beaudoin, Isabelle Sagnes, Rama Raj, and Fabrice Raineri. High q factor inp photonic crystal nanobeam cavities on silicon wire waveguides. *Opt. Lett.*, 41(3):579–582, Feb 2016. doi: 10.1364/OL.41.000579. URL <http://ol.osa.org/abstract.cfm?URI=ol-41-3-579>. 61

Chapter 4

Investigation on Distributed Feedback lasers: performance and comparison

In this chapter, we discuss measurements performed on the lasers whose fabrication was previously exposed. We will here discuss the performance of our lasers, and try to evaluate the efficiency of the different kinds of gratings. A particular attention is brought to the analysis of Complex-Coupled (CC) DFB lasers emission, and comparison to conventional Fabry-Perot and DFB laser technologies.

To be measured, the lasers were cleaved and divided by sections gathering 15 different lasers with same Bragg wavelength, described in section 2.1.3 of previous chapter. This way, we are able to test and compare different laser technologies of lasers with the same cavity length. Unless mentioned, no High-Reflection (HR) or Anti-Reflection (AR) coating was performed on these lasers, their facet reflectivity is thus only determined by the cleaved facets. From simple measurements, and by collecting data from the different sorts of lasers fabricated, it was possible to have a good representation of the influence of dielectric and metallic gratings, as well as the phase shift between gratings when possible. These first sets of measurements will be later confronted to more in-depth measurements, which consist on one hand in the probing of the laser cavities with external tunable laser and on the other hand in the evaluation of external feedback resistance of our lasers.

4.1 Sample layout

First and foremost, we introduce the layout chosen to arrange the fabricated devices. Because of the high number of lasers, a specific labeling is used in order to avoid long references to their design characteristics. As our approach is here to compare the emission and operation of DFB lasers grating types, we kept lasers corresponding to each grating type within the same cleaved bar. This way, laser of same cavity length can be compared for the set of lasers belonging to the same bar. To clarify the operating wavelength, grating type, and cavity length, a labeling convention was decided. This convention is used in this chapter to refer to the different types of lasers, with the following layout:

a00_0000

The first letter is associated to the design Bragg wavelength of the laser, "a" represent gratings with a Bragg wavelength of $1.53\mu\text{m}$, "b" for lasers with Bragg wavelength of $1.55\mu\text{m}$, "c" of $1.57\mu\text{m}$ and "d" of $1.62\mu\text{m}$. The number following this letter is associated to the type of laser, or more precisely, the coupling mechanism involved. Table 4.1 presents the lasers numbers and the laser type associated during the design phase.

The amplitude mentioned in this table is a reference to the amplitude of the dielectric grating, presented in chapter 3. Finally the last number appended to the laser name is related to the cavity length, also corresponding to the length of the bar each set of 15 lasers is cleaved from. In this chapter and the following, we will be particularly interested in the performances of lasers operating at $1.53\mu\text{m}$ and $1.55\mu\text{m}$ as lasers with $1.57\mu\text{m}$ Bragg wavelength were not working properly, for reasons identified as coming from the electron-beam lithography step, and $1.62\mu\text{m}$ were mainly fabricated to be measured in passive mode away from the gain curve of the active region.

Laser number	Laser type
01	Broad area electrical contact
02	250nm amplitude index coupled DFB laser
03	500nm amplitude index coupled DFB laser
04	1 μ m amplitude index coupled DFB laser
05	First order gain coupled DFB laser
06	Third order gain coupled DFB laser
07	Complex-Coupled DFB laser
08	Complex-Coupled DFB laser
09	Complex-Coupled DFB laser
10	Complex-Coupled DFB laser
11	Complex-Coupled DFB laser
12	Complex-Coupled DFB laser
13	Complex-Coupled DFB laser
14	Complex-Coupled DFB laser
15	Fabry-Perot laser

Table 4.1. Layout used to label the types of lasers

4.2 Light current characteristic

The Light Current (LI) characteristic, showing the evolution of the emission output as a function of the injection current, was measured in pulsed current operation at 21°C. The equipment used to monitor the optical power from the lasers was a photodiode combined with a synchronized automated acquisition system. Thanks to this free space configuration, all the emission could be converted without using a coupling fiber.

A high number of devices were investigated of different grating types, to try to ascertain any physical explanation of the results distribution, and a potential relation with PT symmetry.

4.2.1 Performances of the Fabry-Perot

In most cases, broad area lasers are added to the fabrication process to determine material properties. The fabrication process inducing lower losses in such structures, the emission characteristics of broad area lasers are more reliable. We however decided to fabricate broad contact section without cavity, to test the electrical conductivity of the material, and chose not to fabricate any broad area laser, for wafer space saving reasons. The performances of the Fabry-Perot cavity can also teach a lot on the characteristics of the active structure our lasers are made. If its value is best determined from broad area lasers, the modal gain of the material can be evaluated from the current threshold of Fabry-Perot cavities. It also gives a good indication of the optimal laser length to be cleaved without considering the effect of potential grating, as the threshold current and output power will be linked to the density of current, itself set by the length of our lasers. The threshold current density is defined by:

$$J_{th} = \frac{I_{th}}{L \cdot W} \quad (4.1)$$

Where J_{th} is the current density at threshold of stimulated emission, I_{th} is the injection current at threshold, L is the length of the laser and W is the width of the laser ridge. The modal gain of the structure is associated to the density of current at threshold by the so-called logarithm-gain relation, valid for quantum wells:

$$\ln(J_{th}) = \ln(J_0) + \frac{\alpha_i + \alpha_m}{\Gamma \cdot g_0} \quad (4.2)$$

Whith J_0 being the current density at transparency, $\Gamma \cdot g_0$ the modal gain, α_i the internal losses and α_m the mirror losses. The modal gain can thus be written as:

$$\ln(J_{th}) = \ln(J_0) + \frac{\alpha_i}{\Gamma \cdot g_0} + \frac{1}{2 \cdot \Gamma \cdot g_0} \ln\left(\frac{1}{R_1 R_2}\right) \left(\frac{1}{L}\right) \quad (4.3)$$

Where the mirror losses α_m are expressed as:

$$\alpha_m = \frac{1}{2 \cdot L} \ln\left(\frac{1}{R_1 \cdot R_2}\right) \quad (4.4)$$

Where L is the cavity length and R_1 and R_2 the reflectivity of the laser facets. We mostly worked with uncoated cleaved facet, giving $R_1 = R_2 \approx 0.32$. These equations will be used later to compute the modal gain in the light of measurements discussed thereafter.

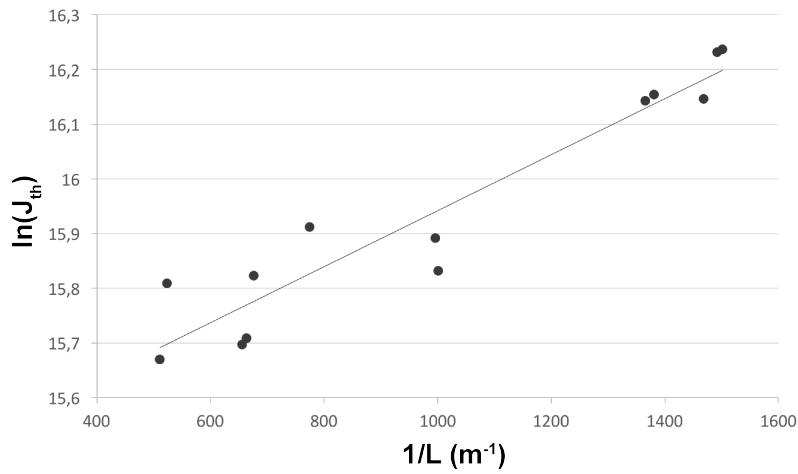


Fig. 4.1. Neperian logarithme of J_{th} versus the inverse of the cavity length

Figure 4.1 is a graphical representation of the variation of the neperian logarithm of the threshold current density measured from Fabry-Perot cavity lasers versus the inverse of their cavity length. From equation 4.3, we see that the evolution between the two quantities should be linear. The modal gain of our material can thus be calculated from the slope S of the curve, using the following expression:

$$\Gamma \cdot g_0 = \frac{1}{2 \cdot S} \ln\left(\frac{1}{R_1 R_2}\right) \quad (4.5)$$

The calculated modal gain of our wafer is $\Gamma \cdot g_0 = 23\text{cm}^{-1}$, which is comparable to what can be found in the literature for multiple quantum-well based structures [?]. As a reminder, the active layer used within this work is composed of two quantum wells.

4.2.2 Overview

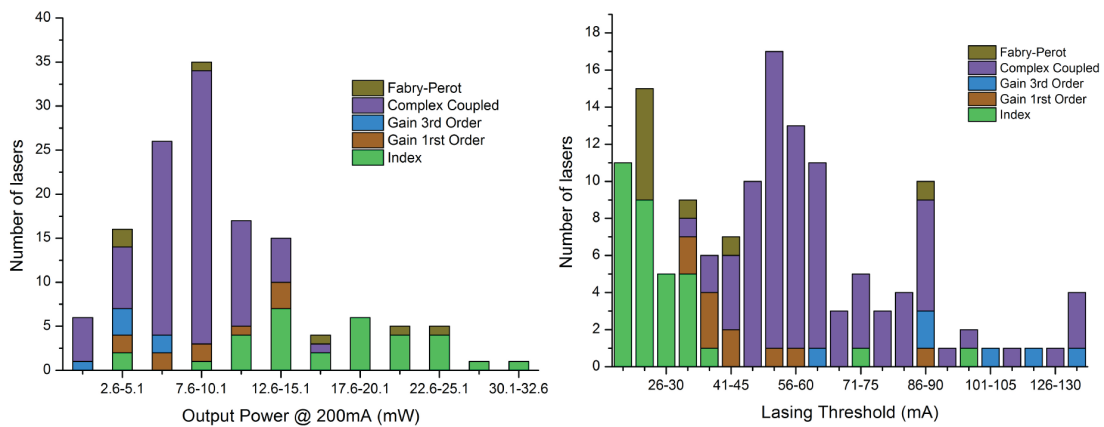


Fig. 4.2. Power (left) and threshold current (right) distribution of lasers with Bragg wavelength of 1.55 microns

Figure 4.2 right presents the distribution of the lasing threshold among the population of fabricated lasers designed to operate at $1.55\mu\text{m}$. The horizontal axis represents the range of lasing threshold, while the vertical axis represents the amount of lasers belonging to the associated threshold category. The colors present the type of lasers among the population: Fabry-Perot cavity, Index-coupled, gain-coupled or complex-coupled DFB lasers. Figure 4.2 left is the equivalent histogram, in which lasers are arranged from their output power at 200mA injection current. These distributions are obtained for a pool of 128 lasers staggered in 16 samples, designed to operate at $1.55\mu\text{m}$, and of cavity length ranging from $750\mu\text{m}$ to $1960\mu\text{m}$. Let us give an overview of the main trends.

Best results among the data set are obtained for standard Index-Coupled (IC) DFB lasers, a vast majority of them presenting a threshold current under 40mA, and output power above 10mW at 200mA. Grating amplitudes of 250nm, 500nm and $1\mu\text{m}$ seem to give same output power with results of 20mW at 200mA which is consistent with results exposed in the literature over large span of materials and architectures [? ? ? ?].

Comparable results were obtained with Fabry-Perot cavities, but the dielectric grating improving the photon density inside the laser cavity, a lower threshold and higher output power is reached in IC DFBs. This phenomenon is only mitigated by the losses, originating from the grating geometry and surface roughness.

These charts show that first order Gain-Coupled (GC) grating devices present a lower threshold and higher output power than their third order equivalent. This difference in lasing performances is most likely due to the presence of radiation losses [? ?] and lower coupling coefficient [?] when operating at third order, and is consistent with the observation made at the end of chapter one, where the emission maps showed that threshold was reached with an increased amount of gain compared to first order gain-coupled DFB lasers. Furthermore, the Bragg period being 3 times longer for a similar duty-cycle, the overlap between the electric field extrema and the metal is larger, thus leading to higher metallic losses. This physical mechanism is presented on figure 4.3.

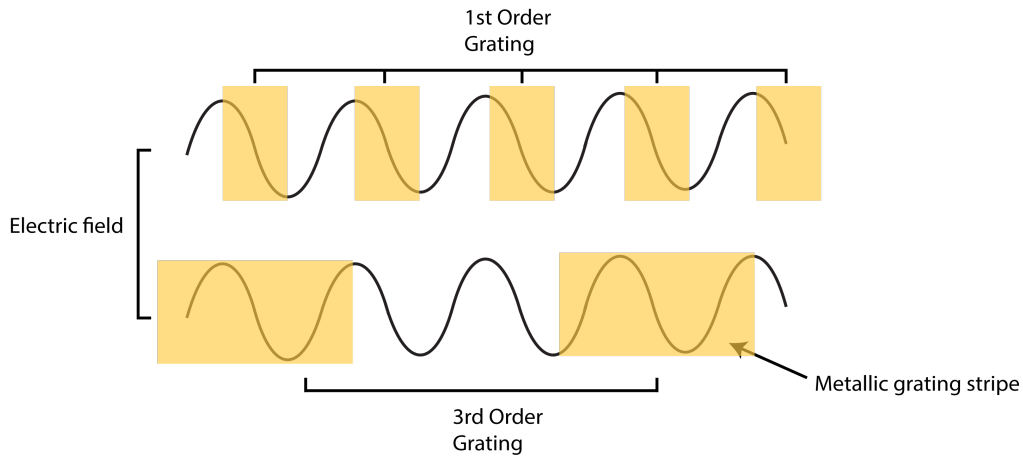


Fig. 4.3. Representation of the overlap between electric field and first or third order metallic gratings

For these reasons, third order GC DFB lasers are poorly represented in the distribution exposed, as a majority of them could not be found to reach lasing conditions. The performances measured on working samples show a very high threshold, mostly above 90mA, and a relatively low output power, under 7.5mW at 200mA.

The purple bars represent data measured from the CC DFB lasers. These lasers have output powers ranging from 5mW to 12.5mW for the majority and lasing thresholds between 45mA to 65mA. Though these performances are reduced compared to index-coupled lasers, they represent a major improvement with regard to their third order gain-coupled counterpart. The distribution of these lasers is however less homogeneous, due to a higher number of lasers, and to the variety of phase shifts between metallic and dielectric gratings, impacting their emission performances. The detailed performances of IC and CC DFB lasers will be presented in the following sections, as these two types have a parametric variation in the population.

Finally, a similar set of observations are made for lasers designed to work at Bragg wavelength of $1.53\mu\text{m}$ for "a" type lasers. Figure 4.4 presents the histogram associated to the population distribution.

4.2.3 Performances of the complex-coupled DFB lasers

In the previous section, we discussed the power and threshold distribution of the general types of lasers, split in 4 categories: index, gain, complex coupled DFB lasers and Fabry-Perot cavity lasers. It is quite clear that lasers have different threshold and power characteristic depending on their grating, the distribution diagrams did not discriminate the complex-coupled DFB lasers depending on their relative (real to imaginary) phase however.

Because of the uncertainty about the exact relative phase between the metallic and dielectric gratings, related to the misalignment observed after the EBL process, analyzing the lasers simply from their assumed laser type or number would be biased. Indeed, it is not certain that their label is a reliable information on the exact associated relative grating phase. However, as discussed earlier in this chapter, the phase shift increment is itself considered as a trustworthy information. It is then possible to compare lasers originating from the same sample, as they are all located in the same latitude of the fabricated wafer. The phase shift increment being conserved, it is interesting to look for a pattern in the measurement data, and try to identify lasers from their light current characteristics.

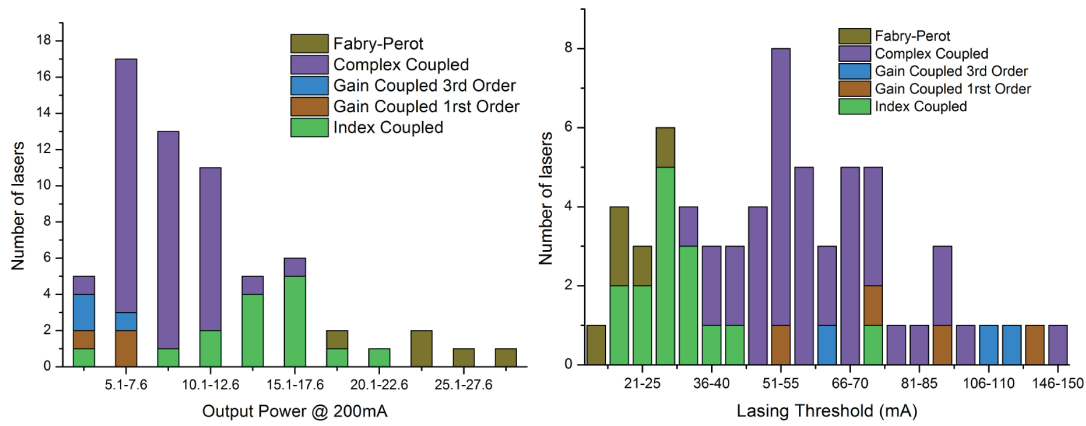


Fig. 4.4. Power (left) and threshold current (right) distribution of lasers with Bragg wavelength of 1.53 microns

Figure 4.5 shows the emission threshold (red) and output power (black) of lasers of the same sample. Lasers sharing the same graphic belong to the same sample, and are therefore of equal cavity length. The laser number in abscissa correspond to the labeling presented earlier in this chapter, in Table 4.1. We remind that the imaginary-to-real phase grows from left to right by $\pi/8$ increment.

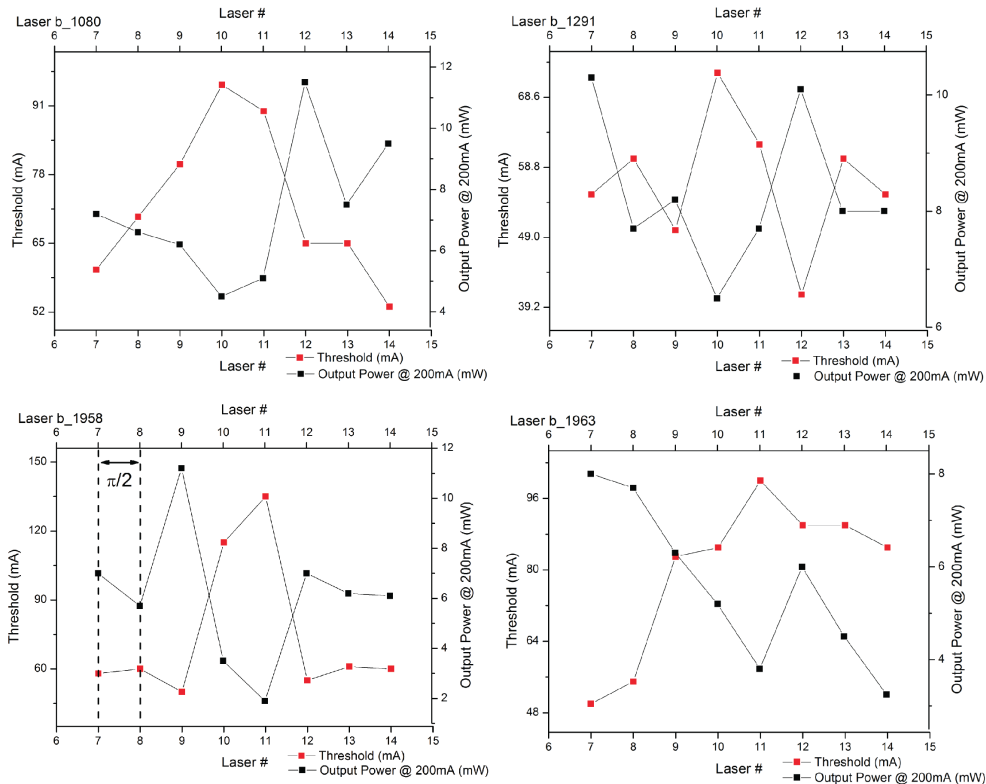


Fig. 4.5. Evolution of the lasing threshold (red) and output power at 200mA (black) of complex-coupled DFB lasers following their labellings and nominal phase, operating at 1.55 microns. The phase is increased by $\pi/8$ for each label.

First it is not surprising to see that the lasing threshold and output power at 200mW varies in opposite ways. Indeed, the differential efficiency being somewhat constant between

the lasers, a lower threshold will lead to higher output power for a given injection current. The output power of the CC DFB lasers varies from around 2mW to 12mW within a given sample, and similarly the lasing threshold ranges from around 40mA to over 90mA for a given set of lasers. This amplitude of variation and its repetition tend to prove the existence of a correlation between laser types and emission characteristics.

A common pattern seems to emerge between the entire data set. First, the single occurrence of a minimum threshold current for each set of lasers indicates the existence of a preferential phase shift demonstrating optimal performances. Aside from this extremum value, the threshold current seems to decrease linearly in the case of b_1080 and b_1963. It is worth noting here that laser b07 and b12 are lasers demonstrating the best overall performances, when the higher threshold current (and therefore lowest output power) is reached for b10 and b11.

The specific pattern followed by the output power and lasing threshold seems to be dependent on the gratings relative phase. However, the pattern extrema of data are not systematically achieved for the same relative phase. This reason can be due to deviation or alignment shift of EBL process, or uncontrolled index and/or loss variations coming from the fabricated structure. Unfortunately, it is quite demanding to get a full set of complex-coupled DFB lasers all working correctly, for various reasons, at least one of them misses, very often due to either breakage but also other malfunction. Yet the only lasers allowed for comparison are lasers found within the same sample. Indeed, as previously stated we were only able to be certain of the phase shift increment between lasers belonging to the same sample. Four laser bars of type a and 6 of type b have their entire set of CC DFB lasers working, the measures acquired on type "a" and "b" lasers are presented in the appendix.

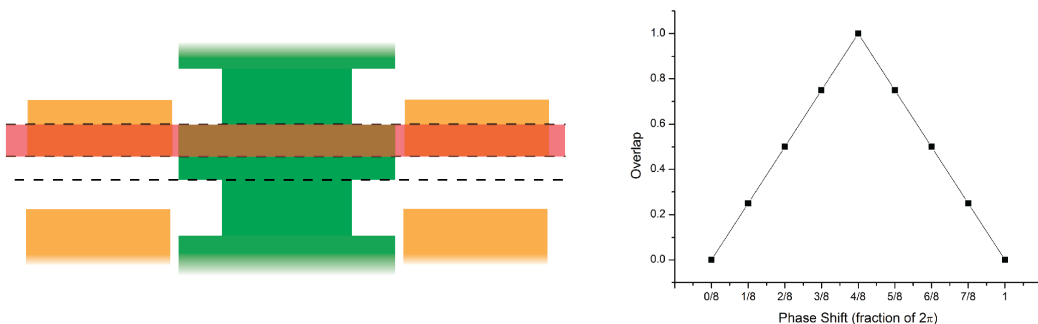


Fig. 4.6. Estimated overlap between regions of maximum amplitudes of metallic and dielectric gratings. On left is a representation of this overlap for a given phase shift. On right is the representation of the convolution between two pulses of equal width versus the phase delay, evaluating the surface overlap between them

A reason that can be found to explain the evolution of the LI characteristic of laser with the relative phase can be the change in mode confinement with the modulation of the ridge width. Indeed, as shown in figure 4.6, if we consider that the mode in large grating amplitude region is less confined, we can surmise that the total amount of losses seen by the mode inside the cavity will be dependent on the overlap between these high grating amplitude regions and the metallic stripe of the gain grating. This overlap is maximum when the gratings are in phase, and minimum when gratings are out of phase.

4.2.4 Conclusion on the emission power

The light-current characteristic of the IC, GC and CC DFB lasers fabricated were measured. From these measurements, the threshold current and output power at 200mA were extracted to serve as indicators, monitoring the output performances of our devices. From these data, it was found that CC DFB lasers could deliver significantly higher power than third order GC DFB lasers, while carrying similar characteristic in their loss grating profile. At third order, the association of dielectric and metallic grating seem to be a better solution than conventional GC DFB laser to reach low threshold current and high output power values.

The monitoring of the indicators presented above versus the laser label -assumed to be monotonously linked to their gratings relative phase without knowing it precisely-, tends to show that the performances of the CC DFB lasers is related to the phase shift value between dielectric and metallic gratings. Indeed, the variations in laser performances are quite sizable, and present in all the samples measured. Notably, best performances seems to be obtained for a given phase value, which could be linked to the amount of losses seen from the mode depending on its confinement.

4.3 Spectral Performance and Evolution

The spectra of the lasers were measured using an Optical Spectrum Analyzer (OSA), associated to an optical isolator, avoiding reflections that could deteriorate the laser emission. The resolution of the OSA was set to 1pm, and the spectrum was observed on a range from 1500nm to 1600nm. The lasers were mounted and soldered to a copper baseplates using Indium coating, and positioned on a metallic plate thermally regulated by a Peltier ThermoElectric Controller (TEC). The acquisition was performed at a temperature set point of 21°C. Current was injected in continuous wave (CW) regime and the laser output was collected using a lensed fiber.

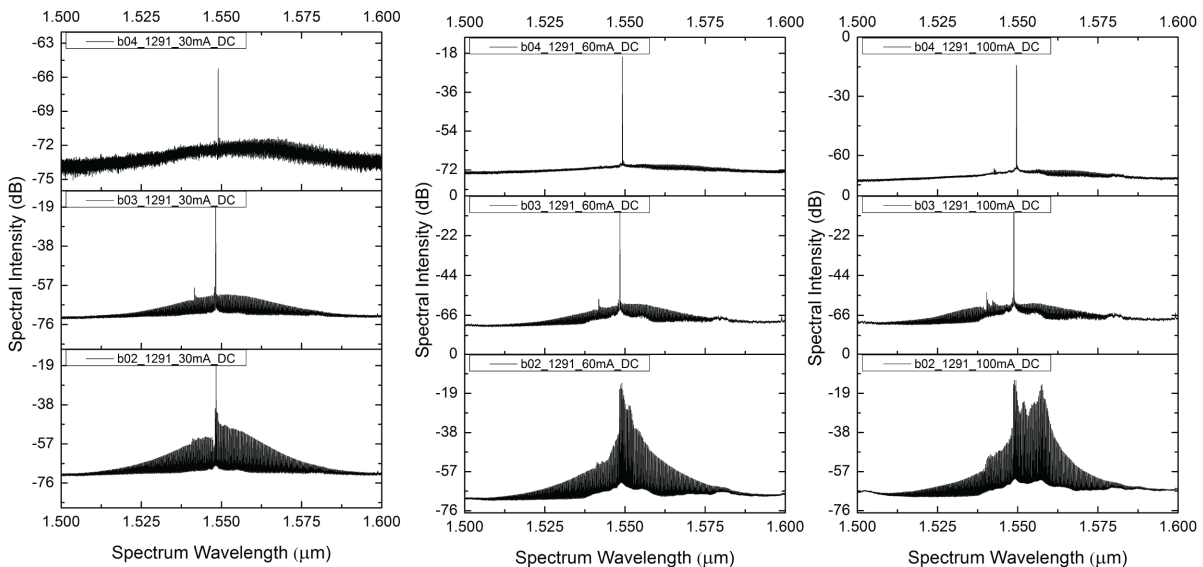


Fig. 4.7. Spectrum of index-coupled DFB laser of 3 amplitude at increasing current: 30mA (left), 60mA (center) and 100mA (right). 250nm, 500nm and 1000nm grating amplitudes are respectively associated to b02, b03 and b04

4.3.1 Comparison of the Conventional DFB Lasers

Index-Coupled DFB lasers

Figure 4.7 presents a first set of measurements obtained from index-coupled DFB lasers of different gratings amplitude but similar cavity length, under increasing injection current. Lasers are again referred to under the labeling exposed earlier in Table 4.1. At low current these lasers are monomode, with slight differences in Side Mode Suppressing Ratio (SMSR). With the increase of injection current, the spectrum of 250nm amplitude grating lasers becomes quickly multimode, with a large envelope quite similar to a Fabry-Perot cavity.

The best single-mode operation is attained for the 1 μ m and 500nm amplitudes dielectric DFB laser, which keep their monomodality above 60mA. However, these gratings amplitudes does not seem to be sufficient for high current, as the mode competition modifies the spectrum, which progressively becomes multimode (see figure 4.8).

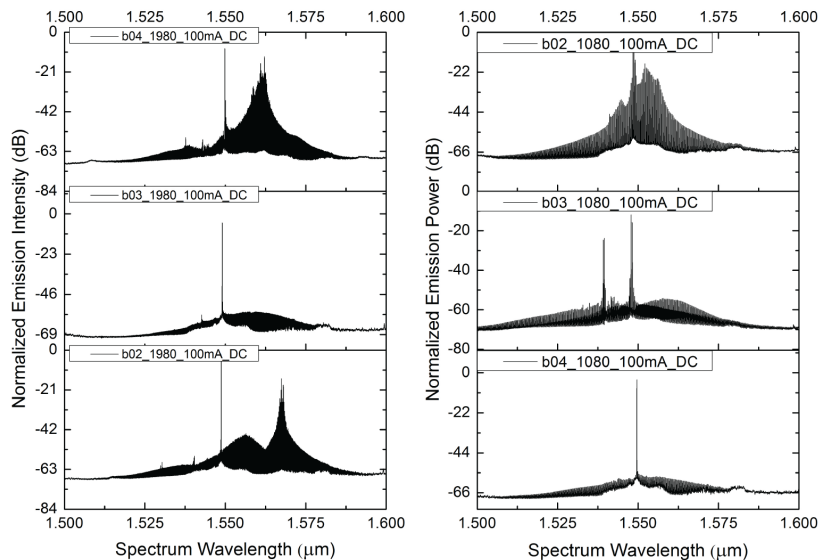


Fig. 4.8. Examples of IC DFB lasers operating at 1.55 microns with increasing grating amplitude (from top to bottom), for 1980 microns (left) and 1080 microns (right) cavity length at 100mA injection current. Gratings amplitudes are: b02: 250nm, b03: 500nm, b04: 1000nm. The monomodality at such current is not systematic.

The mode selection inside the cavity being the consequence of the coupling between the dielectric grating and the propagating modes, the most resistant lasers in their single mode operation should thus have higher coupling. It seems here that an increasing grating amplitude goes together with a greater coupling coefficient. However, one could argue that the difference between 1 μ m and 500nm grating is modest in term of spectral response. This is probably symptomatic of the coupling constant limitation coming from the fabrication process. Indeed, as seen in the previous chapter, the etching process was found to be better realized for low grating amplitudes, as elongated grating trenches could not be etched all the way down. The present example, as well as the observations made on the output power and lasing threshold, tends to prove that 500nm and 1 μ m gratings are of equivalent strength.

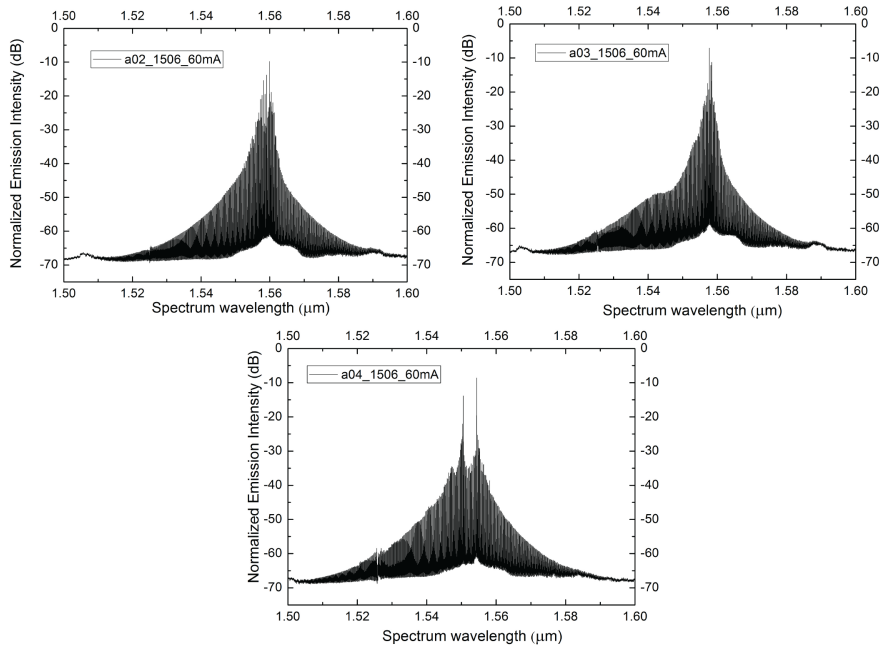


Fig. 4.9. Examples of emission spectra of type-a index-coupled DFB lasers, with Bragg wavelength of 1.53 microns.

Figure 4.9 present the emission spectrum of lasers designed to work at $1.53\mu\text{m}$. For these lasers the spectrum is multimode for each grating amplitude, and the effect of the dielectric grating are in most cases not noticeable. $1\mu\text{m}$ grating amplitude lasers have been witnessed to affect the modes of the cavity in some rare cases, but not enough to get a efficient filtering, hence resulting in Fabry-Perot type multimode laser emission.

Gain-Coupled DFB lasers

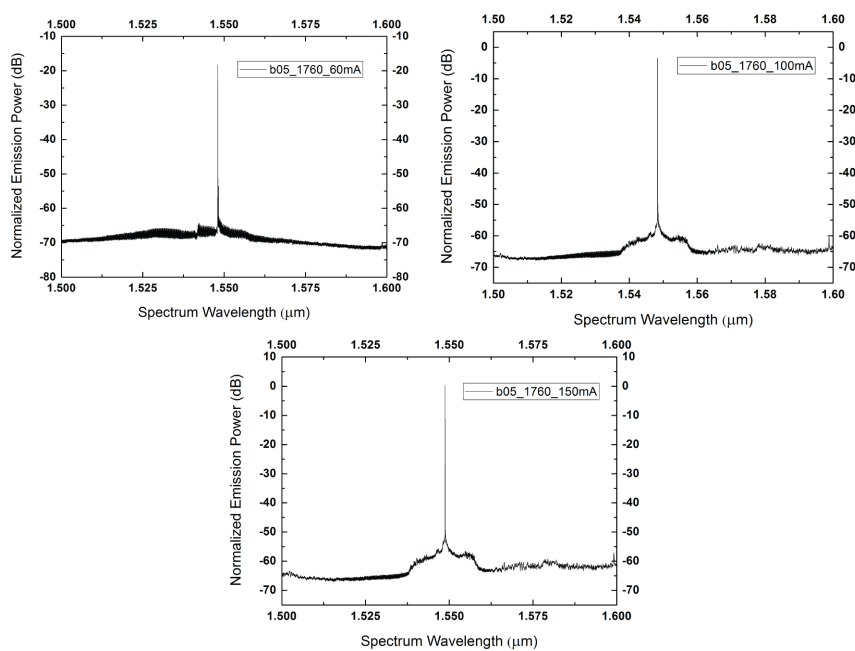


Fig. 4.10. Emission spectra of first order gain-coupled DFB laser at increasing currents.

The emission spectrum of the GC DFB lasers at $1.55\mu\text{m}$ are represented figure 4.10. First order grating lasers have a single mode spectrum, with large SMSR values, above 50dB, and over a large current range.

Third order GC DFB lasers also demonstrate a monomode spectrum over a large current range. However in this case the SMSR is reduced compared to first order, as the grating seems to be less efficient in the filtering of Fabry-Perot cavity modes (see figure 4.11). The measurements on these types of lasers are not homogeneous, and correspondingly, most of them were not working properly.

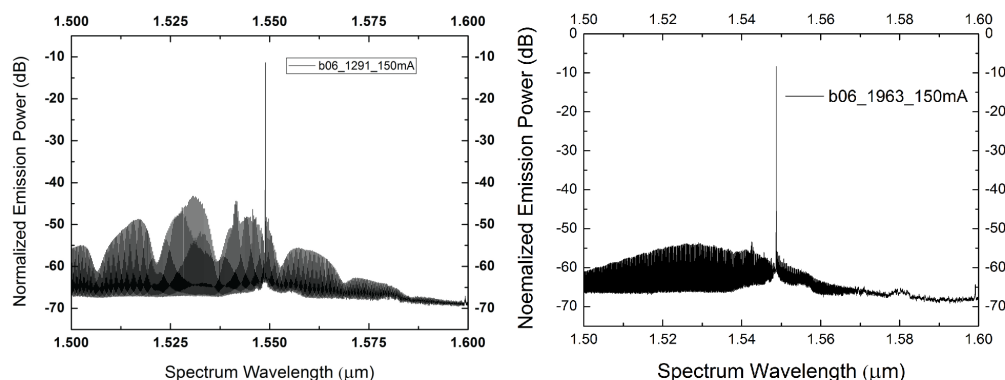


Fig. 4.11. Emission spectra of a third order gain-coupled DFB laser

Gain Coupled DFB lasers with gratings operating at $1.53\mu\text{m}$ also demonstrate an interesting single frequency behavior. If it is risky to conclude on the potential differences between first and third order in that case, as the number of working third order lasers is quite small and their power is low, it is worth noting here that metallic gratings demonstrated much better filtering efficiency than dielectric gratings. Indeed, GC DFB lasers work by increasing the losses inside the cavity for modes not satisfying the Bragg condition. Longitudinal side modes are then attenuated, and the mode at Bragg wavelength will dominate the spectrum. This mechanism of side mode attenuation, not present in IC DFB lasers, explains the differences in monomodality between IC and GC third order DFB lasers operating at $1.53\mu\text{m}$.

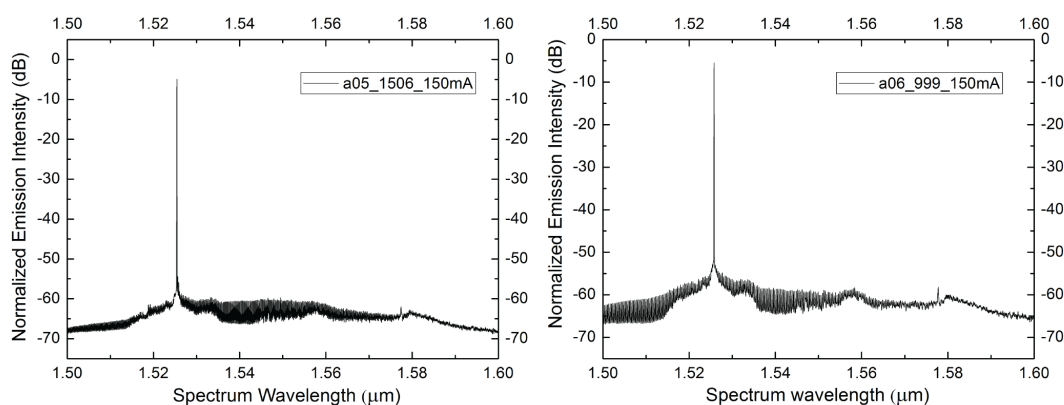


Fig. 4.12. Emission spectra of first (left) and third (right) order gain-coupled DFB lasers operating at 1.53 microns at 100mA injection current

Our observation on the the spectral behavior of IC and GC DFB lasers is in agreement with the discussions reported in the literature [??]. In their article, Lowery et Al. [?]]

mention that the multimode behavior at high power of IC DFB lasers possibly originates from Spatial Hole Burning (SHB). This effect is particularly present in high-coupling IC DFB lasers, in contrast with GC DFB lasers where SHB is attenuated.

4.3.2 Spectrum comparison of the CC DFB Lasers

In the previous sections, the emission spectra of the conventional IC and GC DFB lasers fabricated were discussed. Both IC and GC DFB lasers were found to have single frequency spectrum above threshold. The single frequency behavior was however not similar between different types of lasers. For IC DFB lasers, the single mode operation was observed to be more robust for 500nm and 1 μ m grating amplitudes than for 250nm grating amplitude. Furthermore, IC DFB lasers designed to operate at 1.53 μ m have a multimode spectrum similar to a Fabry-Perot cavity laser when GC DFB lasers of the same type are single mode with high SMSR value. GC DFB lasers were also found to maintain single frequency operation at relatively high injection current, when their IC counterparts become multimode in this current range.

To our knowledge, no experimental investigation on the emission spectrum of complex-coupled DFB lasers can be found in the literature. Theoretical observation made from coupled wave analysis are however available [?], with similar conclusion to the simulation work presented in chapter 2.

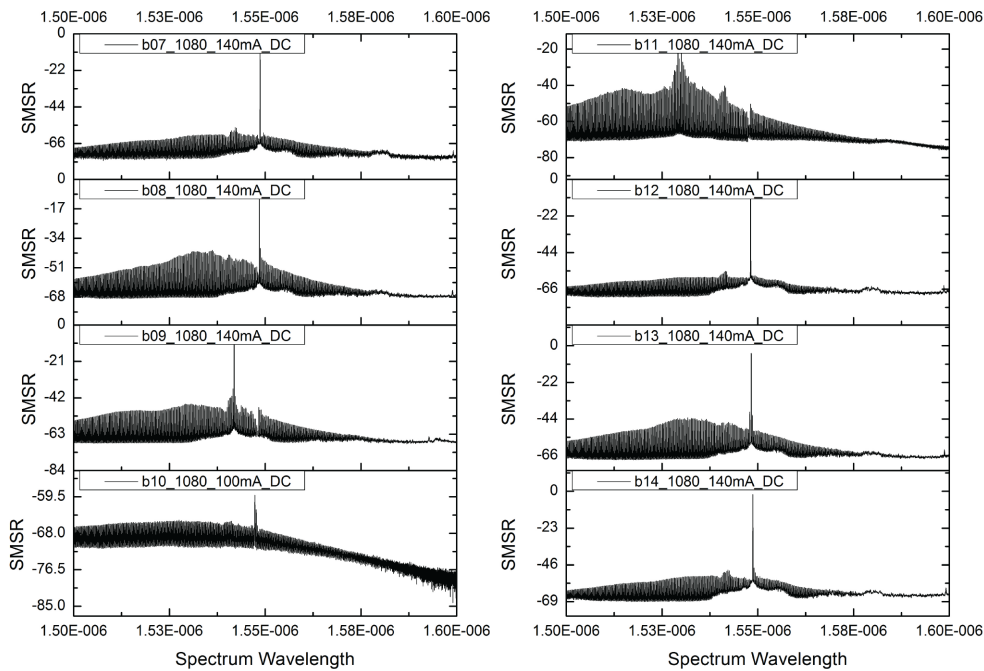


Fig. 4.13. Emission spectra of complex-coupled DFB lasers for different gratings relative phase

An example of emission spectrum evolution of complex-coupled DFB lasers depending on the relative phase between gain and index gratings is presented on figure 4.13, with current of either 100 or 140 mA to attain comparable powers. Here also, the wavelength selectivity seems to be dependent on the relative phase shift between gratings, as the spectrum is not systematically monomode. At first it is hard to see any correlation between the place of the laser on the sample and its monomodality. However, it must be

noted that the lasers showing the purest spectrum and with the highest SMSR, were the one pointed out for their high emission power E.E. b07 and b12.

It is also worth noting here that lasers designed to operate at $1.53\mu\text{m}$ have are found to have a single frequency operation as well, reminding of the case of gain-coupled lasers. Observations here are similar to the case of laser designed to operate at $1.55\mu\text{m}$: it seems that a correlation exist between the gratings relative phase and the filtering of the cavity modes. Again, if we compare those results to the evolution of output power and threshold, we notice that lasers with the purest monomode spectrum tend to have higher output power and lower threshold.

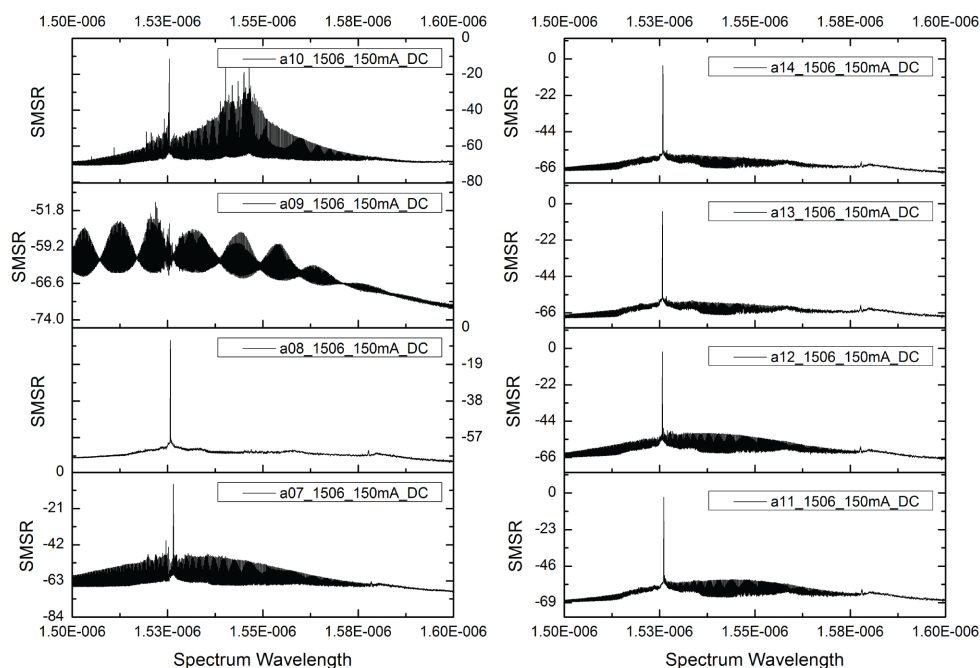


Fig. 4.14. Emission spectra of type-a complex-coupled DFB lasers for different gratings relative phase

To get a representation of effects caused by the relative phase between metallic and dielectric gratings on the spectrum of the lasers we fabricated, it was decided to monitor the SMSR value of CC DFB lasers belonging to the same bar of lasers. This way the performances could be presented similarly to the previous discussion on output power and lasing threshold.

Figure 4.15 is a presentation of the Side Mode Suppressing Ratio, measured for lasers of all grating-types, belonging to the same bar of lasers. Again, each graphic presents results obtained for lasers belonging to the same bar of lasers, as a statistical indicator for the entire population of lasers would be biased, due to potential misalignment during the fabrication process, as previously reported.

The results presented for IC DFB lasers show fluctuations which tends to prove the low efficiency of the spectral filtering. First order GC DFB lasers present very good SMSR values, their evolution has been discussed previously. The variation in SMSR of the monomode laser emission for CC DFB lasers seems to present a repetitive pattern between samples. Indeed for "b" types samples, with Bragg wavelength of $1.55\mu\text{m}$, laser b10 and b11 gave almost systematically no or bad results in SMSR values, when b12 and b07 present high

SMSR values over the whole data set. Results measured for the remaining lasers does not show clear trends however. Similar evolution is found for samples of type-a lasers, designed to operate at $1.53\mu\text{m}$. The particular example of a_999 and a_1506 is shown in figure 4.15, in which lasers a08, a13 and a14 present highest SMSR values, and a07 and a12 present the lowest SMSR values.

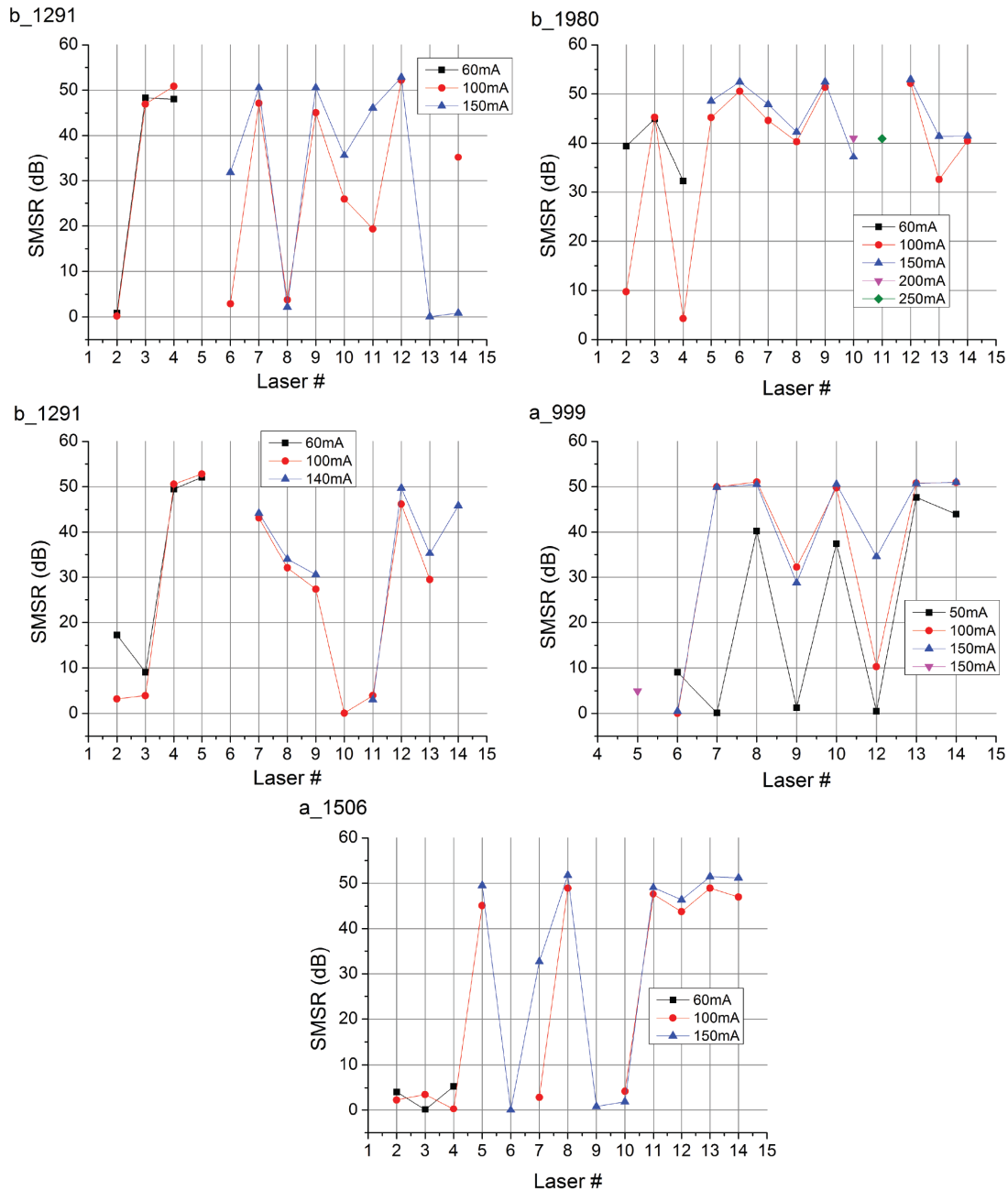


Fig. 4.15. Variation of the Side Mode Suppression Ratio (SMSR) depending for the fabricated laser types. Lasers labelled as "a" operate at 1.53 microns, and as "b" operate at 1.55 microns. Lasers 2 to 4 are IC DFB lasers of increasing grating amplitude, 5 and 6 are respectively first and third order GC DFB lasers, and 7 to 14 are CC DFB lasers with variation of the gratings relative phase.

4.3.3 Conclusion on the spectral performances

The spectrum of the conventional and complex-coupled DFB lasers were measured. Similarly to the discussion on the output power and threshold, a careful attention was brought into the analysis of complex-coupled lasers spectrum, to depict the potential relationship between gratings phase shift and monomodality.

The data show that IC DFB lasers of 500nm and 1 μ m grating amplitude are monomode with SMSR values up to 50dB. For IC lasers with 250nm grating amplitude, the monomodality is not systematic, and associated to much lower SMSR value. Unfortunately the monomodality of IC DFB lasers is not robust, and a threshold current can be found around 80mA-100mA above which many side modes rise up, deteriorating the SMSR.

First and third order GC DFB lasers show monomode operation over a large range of injection current. This observation, expected from chapter 1 simulations, originates from the attenuation of side modes by the metallic grating, and can explain that GC lasers remain monomodes even when designed to work aside from wavelength of maximum spectral gain of the active region (case of "a" type lasers).

Finally, CC DFB lasers present an evolution in their spectral profile, that seems to depend on the relative phase between the metallic and dielectric gratings. Best values were obtained from lasers b07 and b12, or a08, a13 and a14, for which the nominal relative phase expressed in period is respectively 1/4, 1/8, 3/8, 1 and 1/8. These phase shifts were affected through the fabrication process, but the values mentioned here are interestingly clustered around the 1/4 phase shift requirement for PT symmetry. These lasers present a very satisfying spectral operation, often better than first order GC DFB lasers. In the meantime, b10 and b11 show low SMSR values systematically. Specific gratings phase shift values thus seem to impact the spectral emission either for the best, or the worst.

4.4 Conclusion

This chapter was an overview of the general performances of index-coupled, gain-coupled and complex coupled DFB lasers fabricated from the process described in chapter 3. The light current characteristic and spectrum of the laser were looked at, and their evolution in the population of complex-coupled DFB lasers was particularly detailed. The comparison between complex-coupled and conventional DFB lasers revealed that the association of metallic and dielectric gratings leads to the improvement of the lasers characteristics, with higher emission power and enhanced monomode operation.

Within a given sample, indicators such as lasing threshold, output power at 200mA or side mode suppressing ratio were used to monitor the potential impact of the gratings phase shift on complex-coupled DFB laser performances. With this strategy, we observed the mutual evolution of emission indicators, demonstrating optimal performances for specific sets of lasers within a given sample.

These observations led to the conclusions that certain values of the phase between the shifted gain and index gratings gives optimal performances in terms of DFB laser output power and spectrum, based on the triple correlation between the output power, lasing threshold and SMSR value. If the exact value of the optimal phase shift cannot be known precisely, as misalignment was observed on part of the fabricated samples, it is worth noting that best performances in power and spectrum was found for lasers b07 and b12, when the lasers with nominal phase shift corresponding to 1/4 phase PTS condition were b07 and b11.

Whereas these results tend to prove the existence of an optimal shift in gratings components, the observed performances can simply be explained by the repartition of losses in the gratings overlap. Next chapter will be devoted to the probing of Parity-Time symmetry effects, expression on lasers index and loss profiles and feedback resistance.

Chapter 5

In-depth characterization of Complex-Coupled DFB lasers

We previously discussed the power and spectral emission characteristics, of the fabricated DFB lasers. In this chapter, we take a closer look at the interaction between propagating waves inside the laser cavity and the embedded Bragg grating. The first part of this chapter is dedicated to the study of Bragg grating characteristics, by externally probing our lasers with a tunable laser, and acquiring the transmitted and reflected spectral response. Despite their advantageous spectral characteristics, conventional DFB and Fabry-Perot types of lasers can be highly sensitive to a portion of laser light re-entering the laser cavity. The effect of the so-called external feedback may be highly detrimental, as the light is coming from an external cavity at the output of the semiconductor laser. This external cavity can be formed by the reflections of the laser beam on various optical elements such as fiber end-faces, lenses or transparent window from the laser packaging. In many cases the unwanted external feedback is even unavoidable. Using an optical isolator then becomes crucial, and essential, but can severely increase the cost of an opto-electronic equipment as well as its form factor.

5.1 Transmission and reflection response of the lasers

To get a full scope of the performances and characteristics of the Bragg gratings embedded in their cavity, the lasers of all kinds were probed in passive and active configurations. The measurement of transmitted and reflected fields intensity provides an indication on the coupling strength between the grating and the modes propagating inside the cavity, as well as the losses induced by the different types of gratings.

The case of complex-coupling lasers whose gratings relative phase is $\pi/2$ is of great interest here, as this phase shift is required in devices with PTS related effects, characterized by an asymmetric amplification in reflection.

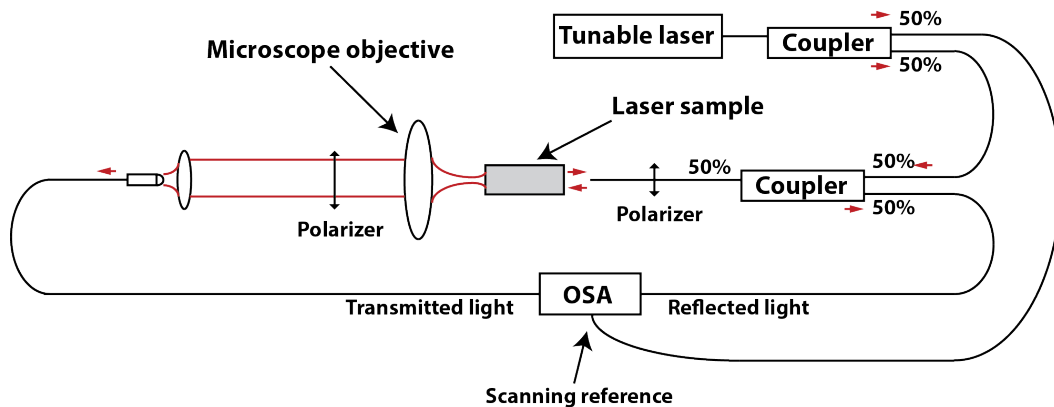


Fig. 5.1. Presentation of the setup used to measure the transmission and reflection characteristics of our lasers

The experimental setup is presented in figure 5.1. The principle is the injection of an incident wave generated by an external tunable laser, into the laser cavity (possibly injected with current as well) and the probing of reflected and transmitted waves. The transmission component is captured by using a microscope objective focusing the light from the end of the laser cavity to a multimode fiber. The reflection component, on the other hand, is captured by the same monomode lensed fiber used to inject the light inside the cavity. The input beam polarization is controlled by a fibered polarizer at the entrance of the setup, and by a second polarizer at the output end of the laser. An optical spectrum analyzer records data coming from transmission and reflection arms, and combines them to

the associated wavelength of the incident beam.

The lasers were measured over a narrow range of injection current while keeping them under threshold, under TE and TM polarization, and in both directions.

The setup bed was partially automated, and results were analyzed using a Matlab code. Figure 5.2 shows the automated generated report constructed by our code for one of the lasers, at a given current, polarization, and for both directions of propagation (labeled as "SU" and "SD" as a convention, and presented on top of each other).

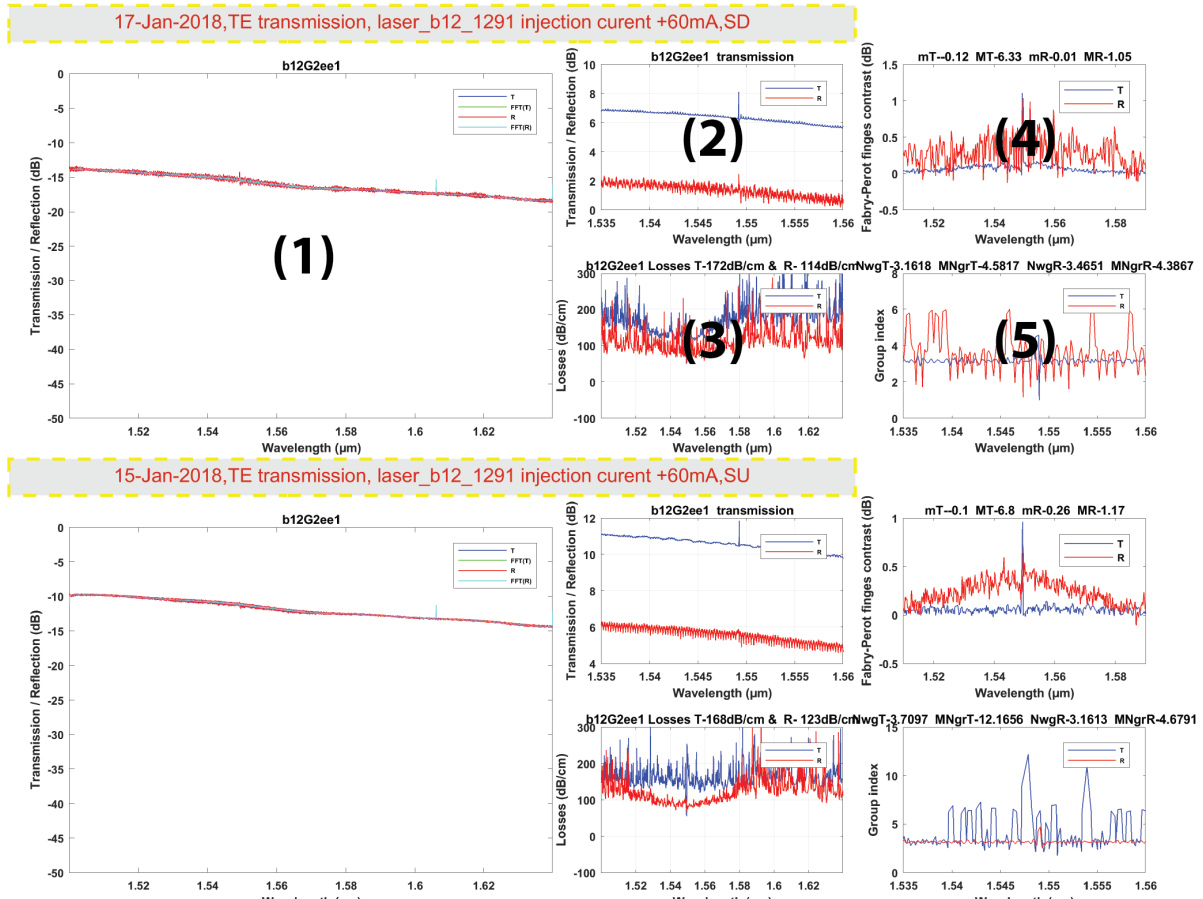


Fig. 5.2. Presentation of the automated report generated from the Matlab code data analyzer. (1) is Transmission and Reflection spectrum acquired, (2) is a zoomed version of this spectrum, (3) is the spectral loss coefficient, (4) is the Fabry-Perot contrast, (5) is the computed group index. Upper and Lower part present equivalent data for opposite directions. SU and SD refer to opposite directions in which the laser is probed.

The analysis of the information acquired from the spectral transmission and reflection of our samples is presenter thereafter.

5.2 Evaluation of the laser losses characteristics

The amount of losses affecting the light injected inside the cavity can teach a lot on the quality of the fabrication process and the way different types of gratings affect the modes inside the cavity. However, as the active region of our material absorbs light in TE mode around the design wavelength, measurements must be performed in TM polarization. Furthermore, as will be discussed in the following section, the calculation of cavity losses

relies on the Fabry-Perot fringes contrast, which is only valid outside of the stop-band, defined by the grating at the Bragg wavelength.

5.2.1 Principle

The losses inside the cavity can be deduced from the transmission data of a TM propagating wave, when the laser is not pumped. The method used here rely on the Fabry-Perot resonances inside the cavity of the laser. The transmitted intensity I_T of a symmetrical monomode Fabry-Perot resonator is given by the standard formula [1]:

$$I_T = \frac{T^2 \exp(-\alpha L)}{(1 - R')^2 + 4R' \sin^2(\Phi/2)} I_0 \eta \quad (5.1)$$

Where I_0 is the laser beam intensity at the entrance of the laser grating or waveguide, η is the coupling efficiency in the fundamental mode of the laser, T is the output facet transmissivity; $\Phi = 2\beta L$ is the phase difference, with β the propagation constant and L the cavity length. R is the reflectivity of the laser facets, and α is the attenuation coefficient of the laser cavity. We note $R' = R \exp(-\alpha L)$. The contrast of the Fabry-Perot cavity resonance H is related to α through the following equation:

$$H = \frac{2R'}{1 + (-R')^2} \quad (5.2)$$

The contrast H is determined by the maximum and minimum values of the intensity of the transmitted wave through the laser cavity:

$$H = \frac{I_{max} - I_{min}}{I_{max} + I_{min}} \quad (5.3)$$

We obtain for R' :

$$R' = \frac{1}{H} (1 - \sqrt{1 - H^2}) \quad (5.4)$$

From the expression of R' , we obtain the following expression for the expression of the attenuation coefficient of our laser cavity:

$$\alpha = \frac{1}{L} \left(\ln R + \ln \left(\frac{H}{1 - \sqrt{1 - H^2}} \right) \right) \quad (5.5)$$

5.2.2 Distribution of losses from grating types

In the discussion on internal optical losses of optical waveguides three contributions must be considered: the scattering resulting from the fabrication process, the free carrier absorption coming from the doping of the waveguide, and the action of the additional absorbing grating present in the case of gain-coupled DFB lasers.

To be able to determine the attenuation induced by the laser grating or cavity, the measurements must be performed in TM polarization. This circumvents absorption of the quantum well structure so the remaining losses are then only due to the absorption of the waveguiding structure. Results of these measurements are presented in figure 5.3.

The measurements presented in figure 5.3 present a similar trend as the emission performances seen in the previous chapter, with an increased amount of losses in presence of metallic grating, corresponding to an decreased output of power (or higher threshold value).

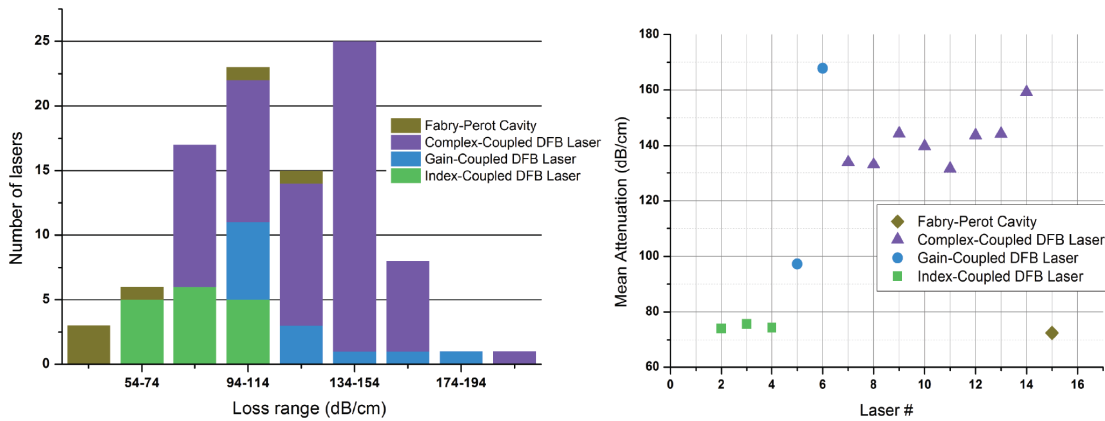


Fig. 5.3. Mean extinction losses measured in transmission: distribution of the lasers depending on their loss range (left) and mean loss by laser type (right), for lasers designed to operate at 1.55 microns (type "b"). Losses are computed from the Fabry-Perot cavity fringes contrast, for a spectral range between 1.5 microns to 1.64 microns.

It is then not surprising to find the Fabry-Perot cavity showing the lowest amount of losses, as the light in these lasers is not affected by any losses coming from either metallic absorption or additional scattering due to the complex geometry of a dielectric grating. Nearly 70% of FP cavities have losses below 54dB/cm. Such substantial propagation losses are slightly higher to what is usually reported for the fabrication of p-doped InP waveguides in absence of post-etch hydrogen passivation of the laser waveguide [2, 3], and is probably due to scattering losses due to higher surface roughness. The mean attenuation of Fabry-Perot cavities and first order GC DFB lasers must be considered carefully, as the distribution presents a large spread, probably due to measurement fluctuations. The mean attenuation of index-coupled DFB lasers is around 80dB/cm. The data gathered through this measurement campaign does not show any trend when discriminating the lasers by dielectric grating amplitude.

A difference exists in linear losses between first and third order Gain-Coupled DFB lasers. Though these lasers have the same mean amount of metallic parts covering each side of the laser cavity, as the duty cycle is similar in both cases, the third order laser demonstrates a much higher amount of loss. This confirms the reason discussed earlier given to explain the high rate of malfunctioning of third order GC DFB lasers.

5.2.3 Index modulation amplitudes

Real part modulation

The wavelength selectivity of a DFB laser reflects its ability to discriminate the mode of the cavity satisfying the Bragg condition and is mainly affected by index and/or gain modulation. This spectral filtering efficiency is better represented through the expression of the coupling constant κ and cavity length L product. It is thus of great interest to have access to this data, as the κL product is the concrete expression of the index and/or gain modulation amplitude in the coupled wave model. However, its ex post determination for a physical device is hardly possible to obtain, as its quantity highly depends on the geometry of the fabricated structure.

For this reason, it was decided to compare the experimental results obtained from the measurements of transmission and reflection spectra, to the simulation results obtained from the model presented in chapter 2. By looking at the stop band width measured experimentally and comparing it to our model, it was possible to find the corresponding values of index modulation amplitudes, for which experimental and simulation results match. Based on the predicted effective index computed in the design process (see chapter 2), we were able to narrow down the research of corresponding index to a range around what was obtained upstream.

Figure 5.4 left presents the transmission spectra of an index-coupled laser with a 500nm grating amplitude and 1506 μm cavity length. The width of the stop band is of the order of 0.2nm. This experimental measurement of the stop-band matches the simulation of the similar structure presented on the right hand side. This plot represent the simulated transmission of a Bragg grating obtained from the model exposed in chapter 2, for a variation of the index real part of $1,25 \cdot 10^{-3}$.

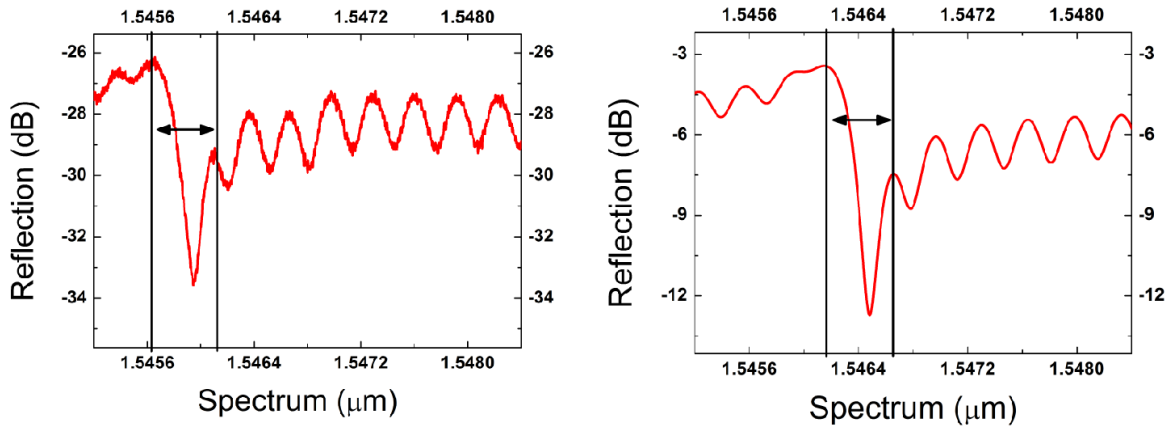


Fig. 5.4. Visualisation of the stop-band in the reflection spectrum of the laser (left), equivalent value of stop-band width obtained from simulation presented in chapter 2(right)

The value obtained from the correlation of transmission and simulation results is slightly different than the one deduced from the initial design steps. From the simulation of the mode structure presented in chapter 3, the results were indeed closer to $\Delta n = 5,3 \cdot 10^{-3}$, against $\Delta n = 1,25 \cdot 10^{-3}$ obtained from the comparison between simulation and experiments. The difference probably results from the fabrication process imperfection, and particularly from the etching of the grating structure. As presented in chapter 2, the complete etching of the corrugations was very hard to achieve, and the etching down inside the grating openings were not perfect. the index modulation is however of the same order of magnitude as the initially computed value.

Imaginary part modulation

The modulation amplitude of the imaginary part of the index was computed from the absorption measurements discussed in the previous section. The relation between the absorption losses and the imaginary part of the material index is exposed in [4] as the following:

$$\chi = \frac{2\omega}{c} n_1 \quad (5.6)$$

Where χ is the absorption coefficient in cm^{-1} , n_i is the imaginary part of the index, c is the light celerity and ω the angular frequency of the wave considered. The imaginary part of the index is thus obtained straight forwardly by simply reversing eq. 5.6. The absorption values displayed in 5.3 cannot be taken as is however. Indeed, the losses measured for the gain-coupled DFB lasers, even at first order, include losses stemming from the roughness and imperfect aspects of the etched waveguide forming the laser cavity. The losses of the metallic grating α_M are thus obtained by subtracting losses obtained from the Fabry-Perot α_{FP} cavity to the GC first order DFB lasers α_{GC} :

$$\Delta\alpha = \alpha_{GC} - \alpha_{FP} \quad (5.7)$$

The quantities are here expressed in dB/cm , the equivalent in linear unit is $\chi = 10^{\alpha_M/10}$. It must however be noticed that the losses measured from our protocol α_M is affected by the duty cycle of the grating of 50%, and is related to the actual losses as can be seen on figure 5.5.

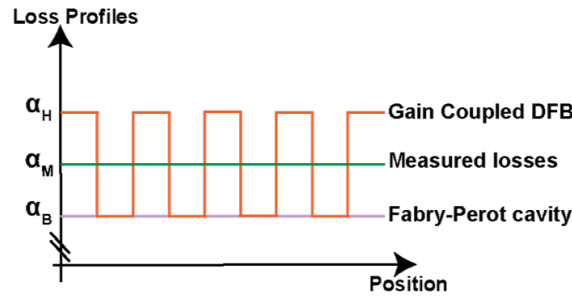


Fig. 5.5. Schematic representation of the loss profile repartition through the cavity of gain coupled, Fabry-Perot lasers and the amount of losses measured with our protocol.

The variation of the imaginary part of the index can thus be deduced from the variation of cavity losses through equation 5.6. The resulting modulation obtained from this method gives a modulation of the imaginary part of the index of $2 \cdot 10^{-4}$. Similarly to the result obtained for the modulation of the real part of the index, the exact value is less relevant than the order of magnitude here also. This order of magnitude is smaller than what was previously obtained for the modulation of the index real part. As a reminder, the goal was to reach a lower coupling from the metallic grating than for the dielectric one to reach lowest losses, inherent to the metal absorption, while still exploiting the side modes attenuation. Unfortunately, having highly unbalanced strength of metallic and dielectric gratings does not promote PTS behavior, as the ideal PTS case requires equal real and imaginary index modulations. On the other hand, complex-coupled DFB lasers resulting from the association of unbalanced imaginary and real index parts modulations demonstrate an improved sustain in monomodality compared to IC DFB lasers, and lower threshold current (see previous chapter).

5.2.4 Evaluation of the coupling constant of index-coupled DFB lasers

Several methods can be found in the literature to express the coupling coefficient from the stop-band width of the laser under threshold. Unfortunately if such methods can have good precision for AR coated lasers [5], or facet with very low reflectivity [6, 7], they are by no means suitable for our cleaved facet lasers. Indeed, the very lineshape of the stop-band has been seen to be impacted by the facet phase and reflectivity [8, 9, 10] of the

index-coupled DFB laser, which is in agreement with our observations. Nevertheless, we decided to apply a method of calculation of the coupling coefficient from the apparent stop-band width, from the following equation at first order [3]:

$$\kappa_{O1} = \sqrt{\left(\frac{\pi n_g \Delta \lambda_S}{\lambda_B^2}\right)^2 - \left(\frac{\pi}{L}\right)^2} \quad (5.8)$$

Where κ_{O1} is the coupling coefficient at first order, n_g the group index, $\Delta \lambda_S$ the stop-band width, λ_B the Bragg wavelength and L the laser cavity length. From the definition of the free spectral range and considering that we are at the Bragg wavelength we have $n_g = \lambda_B^2 / (2\Delta \lambda_{FP} L)$; $\Delta \lambda_{FP}$ being the Fabry-Perot mode spacing. Furthermore, the Fourier series decomposition lead to the relation $\kappa_{O3} = \kappa_{O1} / 3$, where κ_{O3} is the coupling coefficient at third order. By substitution into equation 5.8, we have:

$$\kappa_{O3} = \frac{\pi}{3L} \sqrt{\left(\frac{\Delta \lambda_S}{\Delta \lambda_{FP}}\right)^2 - 1} \quad (5.9)$$

To evaluate the reliability of this method, the results were compared to the following equation approximation obtained at third order from the coupling wave analysis [11, 12]:

$$\kappa_{O3} = \frac{\Delta n}{3n_m \Lambda} \quad (5.10)$$

Δn being the index modulation amplitude, n_m the mean of the high and low index present in the grating, and Λ the Bragg period of the grating. With this approach, we evaluate the coupling coefficient from the real part of the index modulation Δn , obtained from the comparison with the simulation results presented before.

Figure 5.6 presents the results obtained from the method involving the stop-band width (black crosses), compared to the average coupling coefficient obtained from the variation of the real part of the index (red line). The two approaches are in good agreement, both showing a coupling constant between 4cm^{-1} to 10cm^{-1} . The relatively low magnitude of the coupling constant comes from the higher order of the grating involved.

5.2.5 Expression of non-reciprocal effects

As introduced in the first chapter of this manuscript, the expression of PT symmetry beyond exceptional point can lead to unidirectional behavior in the light propagation. In particular, for the case of Parity-Time symmetric Bragg reflector such as our lasers, theoretical works proved that periodic gain or loss could affect the reflected light in one direction of the grating only. This characteristic can possibly improve the resistance of lasers integrating PTS Bragg gratings to external optical feedback. This last point will be discussed in the next section of this chapter.

As the setup described at the beginning of this section is able to probe reflection and transmission spectral characteristics of our lasers for a wide range of parameters, PT symmetric behavior should in theory be observable from the data we acquired.

The spectra comparison, however, can only be valid for equal or equivalent level of signal, and equal or equivalent contrast of Fabry-Perot fringes, otherwise the amplification can be considered as an artifact, all the more because we operate at the edge of threshold, just below. In the case where these conditions are met, the amplification or attenuation levels of the incident wave in transmission or reflection can be discussed fairly. 5 laser

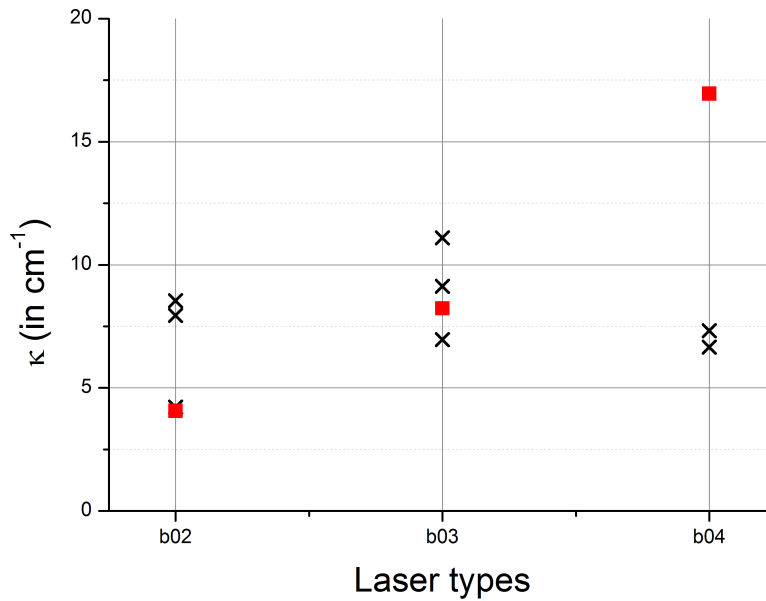


Fig. 5.6. Coupling coefficient evaluated using two different approach: from the stop-band width (cross) and from the index modulation (red dot)

bars, each with 7 lasers of different phase shift between metallic and dielectric gratings were probed. Pure gain-coupled and index-coupled DFB lasers were also measured for comparison.

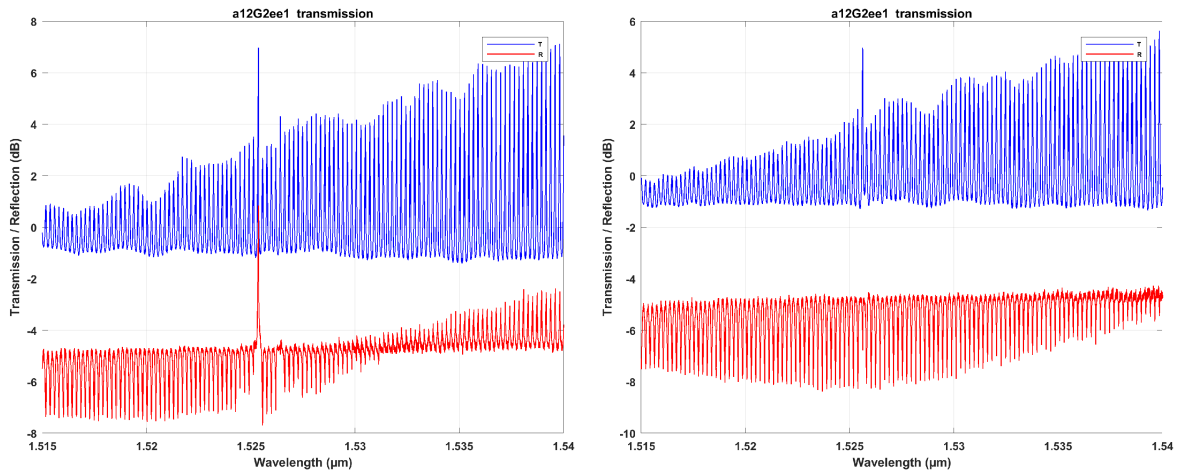


Fig. 5.7. Example of transmission (blue) and reflection (red) spectrum showing asymmetric amplification. On left the reflection is amplified at a Bragg wavelength, while the reflection spectrum in the opposite direction (right) is not.

Among the lasers tested under the protocol monitoring laser's transmission and reflection spectrum, a few results displaying unidirectional amplification or attenuation of the probe wave were observed. Figure 5.7 is a comparison reflected (blue) and transmitted (red) waves amplitude in opposite directions (left and right figures). In this example, we observe that a mode is amplified in reflection in one direction (left) when in the opposite direction the reflection remains constant.

On the global set of data acquired during this campaign, a total of 20 lasers presented asymmetric amplification of light in reflection. Among this population, 17 were complex-coupled DFB lasers, 2 were gain-coupled DFB, and 1 was an index-coupled DFB laser. Though an apparent predominance of asymmetric behavior in the population of complex-coupled DFB lasers, such a conclusion must be discussed. Indeed, a given bar of lasers (also referred here as sample) gathers 3 index-coupled, 2 gain-coupled and 8 complex-coupled DFB lasers. The fraction of CC DFB lasers showing asymmetric reflection with regards to the total number of lasers having this effect is then almost strictly equal to the proportion of these lasers among the total population. An accurate conclusion on the asymmetric amplification is thus hard to find, other than saying that complex-coupled and gain-coupled DFB lasers present equivalent asymmetric characteristics.

It is however interesting to note that a higher proportion of GC and CC DFB lasers present a higher fraction of lasers with asymmetric amplification of reflection than IC ones. It must furthermore be noted that purely gain or index coupled DFB lasers represent a particular case of parity-time symmetry, for which either the real or the imaginary part of the index is modulated. One of the two components remaining equal to zero, the condition of PT symmetry can be considered as fulfilled albeit trivially. One hypothesis to be considered is also the potential impact of the facet phase of metallic grating on the reflected portion of the incident wave.

5.3 Conclusion on external probing of DFB lasers

Index-coupled, gain-coupled and complex-coupled DFB lasers were probed in passive mode and at increasing current under threshold using an external tunable laser. The data collected were the reflected and transmitted wave intensity over a wide spectrum, in TE and TM mode.

From these measurements, we were first able to extract the absorption of the laser cavity, given by the Fabry-Perot fringes amplitude, the real and imaginary part of index modulation. These last two parameters were computed respectively by comparing the stop-band width obtained from simulations and measurements, and by the total absorption of the third order metallic grating. Results present a much higher real index modulation compared to the imaginary part, with a difference of one order of magnitude. Whereas reaching equal modulation of real and imaginary parts of index would foster PT symmetric related behavior, having a stronger index modulation is beneficial to the laser operation, as it reduces absorption along the cavity thus increasing the output power.

We were also very interested in probing our laser from an external source in order to exhibit potential PT-symmetric effects. In particular, we were here looking for an asymmetric amplification of the light in reflection, as expected by the theory. From the available data set, the only viable observation that could be made was that similar proportion of complex-coupled and gain-coupled DFB lasers presented desired asymmetric amplification. It then remains unclear whether this observation originates from the PT-symmetry, as GC DFB are a specific case of index-gain modulation, or from potential effects of facet phase.

5.4 Effect of external feedback on semiconductor lasers

5.4.1 Modeling of laser emission under external optical feedback

External feedback occurs when a laser is situated inside of a larger cavity, leading to the presence of reflected wave entering the laser cavity itself. This situation can be seen as a feedback loop on an amplifier type of engineering system. The amplification of the reflected wave of different oscillating frequency has drastic effect and often results in fluctuations in the laser emission up to chaos.

In 1980, Lang and Kobayashi presented a model of the laser dynamics in the presence of an external cavity [13]. Their model is based on the standard laser rate equation, and includes the presence of an additional external feedback term corresponding to the action of the external cavity.

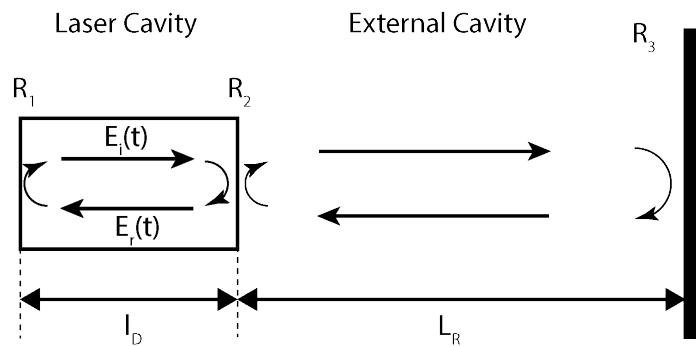


Fig. 5.8. Presentation of the laser inside the external cavity, and the reflected waves at each interface

5.4.2 Regimes of external feedback for long external cavities

When the length of the external cavity is inferior to the laser coherence length, the effects of external optical feedback are rather weak. If the external cavity length is greater than the coherence length of the laser however, optical external feedback can highly affect the operation of semiconductor lasers. In this case of incoherent feedback, the major effects are observed on the emission spectrum through the broadening of the laser linewidth and the increase in the number of modes due to the presence of the external cavity. Depending on the injection current, laser structure or feedback level, mode hopping, intensity fluctuation and excess noise generation can be observed, deteriorating information transport inside the optical communication system.

Intensity fluctuations have drastic impact on the operation of semiconductor lasers, as it damages their modulation response, and external feedback is playing an important role in the apparition of such fluctuations [14, 15, 16, 17, 18]. The presence of an external cavity also very much impact the spectral response of the laser, and can result in the narrowing of the emission [19, 20, 21, 22, 23, 24, 25], or on the contrary its broadening [22, 23], and can even lead to coherence collapse of the laser radiation [26, 27, 28, 29, 30, 31].

Among the effects of external feedback on the emission of our DFB lasers, we will be particularly interested in the spectral characteristic modifications and intensity fluctuations that can occur in their output, which effects have been studied both experimentally and theoretically. The particular analysis of Tkach and Chraplyvy [32], gives details of five

regimes of feedback affecting the laser operation in different ways. The five regimes they relate are:

- Regime I: For low levels of feedback, narrowing or broadening of the emission line is observed. In this regime, the feedback sensitivity is dependent on the emission return polarization.
- Regime II: For levels of feedback depending on the external cavity length, the broadening observed at low level of feedback rate mutates into line splitting and mode hopping. The magnitude of the splitting and hops depends on the strength of the feedback and distance to the reflector.
- Regime III: With increasing feedback rate, its effects become independent of the external cavity length, mode hopping is suppressed and the laser operates on a single narrow line. The laser stability of this regime is balanced with its low range in term of feedback level. In case of fluctuations in feedback power, the laser finds itself oscillating around this regime.
- Regime IV: This regime is also independent on the external cavity length. We here observe the rise of satellite modes whose separation from one another and from the main mode is equal to the relaxation frequency. The increase in feedback rate leads a drastic increase in the laser linewidth. This regime, also called "coherent collapse", is associated to a drastic reduction of the coherence length of the laser.
- Regime V: Among a certain level of feedback (typically -10dB), the laser operates in external cavity configuration. The laser cavity is here considered to be composed of the short active region together with the cavity created by the external reflector. The laser is stable, and can reach a narrow linewidth. Because of the high amount of feedback, this regime is often only reachable through the addition of an anti-reflection coating to the laser facet.

This section is dedicated to the discussion around feedback resistance of the DFB lasers fabricated under external feedback. This resistance will be evaluated from the point of view of coherence collapse, the hallmark the fourth regime of feedback previously exposed, whose effects are independent on the external cavity length, happening for a feedback rate from -50dB to -10dB and is characterized by a sudden and important broadening of the laser linewidth.

5.4.3 Coherence collapse

Among the different regimes of feedback, the Coherence Collapse (CCL) is the most hazardous for laser operation. The drastic broadening of the laser linewidth associated to this regime can be up to several gigahertz, and can be very detrimental to optical communication applications. In addition to the broadening of its linewidth, the optical link also undergoes a strong degradation in its bit error rate [33]. This general effect of external reflections on the laser dynamics is particularly not compatible with applications requiring low level of noise and/or proper control of the laser coherence.

Under the assumption of a long external cavity it was demonstrated that the emergence of CCL under external feedback is independent of the external cavity length [34, 32], as well as the feedback phase [35].

The theoretical and experimental study of Lenstra et al. in 1985 [30] is very informative on the subject of coherence collapse. In their rigorous work, the case of non coherent feedback is exposed, and analytically modeled. The mathematical description relies on the consideration that the coherence time in this case is not greater than the external roundtrip time inside the cavity τ_f . As a consequence, the phase difference $\Phi(t) - \Phi(t - \tau_f)$ cannot be considered as small enough to be linearized. This is a key point of coherence collapse, nonlinearities ought to play a large role.

5.4.4 Requirements for isolator-free operation

Before presenting the tolerances of optical network to external feedback, a semantic foreword must be told regarding the terms referring to light reentering the laser cavity. The Optical Return Loss designated the light reflected inside the optical fiber system, at the end-point of the coupling fiber. The optical feedback is defined as the light power injected inside the cavity, taking into account the coupling losses between the lens and the laser emission. These two quantities are represented on figure 5.9 and should not be confused. Indeed, the optical return loss (ORL) as will be referred here is not representative of the total amount of light that will interact in the laser cavity, as it does not take into account the facet reflectivity or coupling between the fiber and the emission mode. Similarly, the feedback rate referred to here, represents the fraction of light injected inside the cavity, divided by the initial emission power.

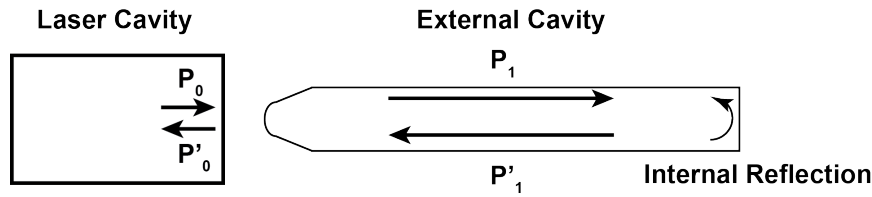


Fig. 5.9. Emitted (P_0), transmitted (P_1) and reflected (P'_1) Power in fiber optical network

The feedback rate γ and ORL ζ are defined as:

$$\gamma = \frac{P_0}{P'_0} \quad (5.11a)$$

$$\zeta = \frac{P_1}{P'_1} \quad (5.11b)$$

Their logarithm versions, in dB, are related to each other to the coupling coefficient of the mode into the fiber C , and to the facet reflectivity R_2 as:

$$\gamma(dB) = \zeta(dB) - 2 \cdot C - 2 \cdot 10 \log \left(\frac{1}{R_2} \right) \quad (5.12)$$

As stated in the introduction of this chapter, the presence of feedback in optical networks is very often unavoidable and constitute a major problem. The effects which occur when a fraction of light is injected back into the laser, and which have been described above, can be dramatic as regards the intensity and spectral stability of the laser.

The IEEE 802.3 standard for 10 Gbps transmission [36] impose the maximum return loss tolerated through the optical path, and is very similar to its counterpart for 40Gbps [37]:

- 10GBASE-L standard: for optical section from 2m to 10km at $\lambda=1300\text{nm}$. This case is limited to -12dB optical return losses.

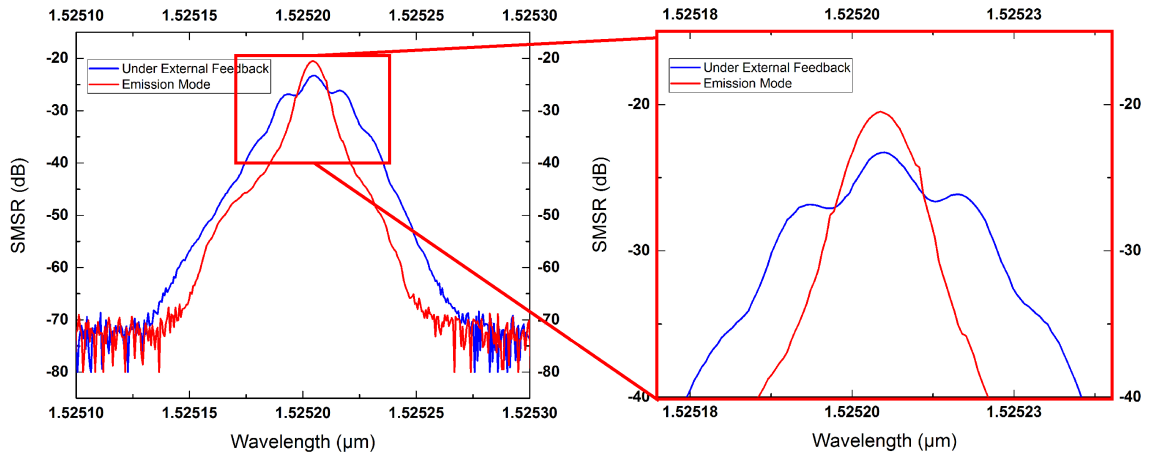


Fig. 5.10. Laser spectrum under coherence collapse. The blue curve is the mode at the onset of coherence collapse due to external feedback destabilisation, the red curve is the original lasing mode spectral power density. Figure on the right hand side is a zoomed version of the initial mode representation, the relaxation oscillation is visible in the blue curve

- 10GBASE-E standard: for optical section from 2m to 40km at $\lambda=1550\text{nm}$. This case is limited to -21dB optical return losses.

The case of the Bragg wavelength corresponding to our design, 10GBASE-E, demands the resistance to optical return loss of our laser to reach a minimum of -21dB for them to be included in a long haul optical network without the use of isolator. This requirement represents the target to reach for external feedback resistant lasers.

5.5 Experimental study of DFB lasers operation under external feedback

5.5.1 Experimental setup and configuration

The resistance of our lasers to external optical feedback was tested using the setup presented in figure 5.11. To best fit the working conditions of this type of devices, it was chosen to couple the output emission inside fibers, and generate feedback internally as would be the case for an optical network. In our setup, thanks to the fiber optic retro-reflector and an optical attenuator, the amount of feedback injected back to the laser was controlled. The power density spectrum of the main emission mode was monitored using a very high resolution (10pm) optical spectrum analyzer, cascaded with an isolator to avoid the generation of unwanted feedback. The polarization of the feedback loop was controlled using a manual fiber polarization controller, to find the most unstable configuration. The feedback power was measured using a powermeter in the weak coupler branch, as presented on the setup layout in figure 5.11.

Only single-longitudinal-mode lasers were tested under optical external feedback. The protocol used to measure the resistance to external optical feedback was to capture the main mode spectrum without any feedback with an OSA, and gradually increase the amount of power fed back into the laser cavity. By monitoring the mode spectrum and comparing it to the original measurement, we were able to detect the regime of coherence collapse. Although it was not possible to measure the polarization of the light returning into the

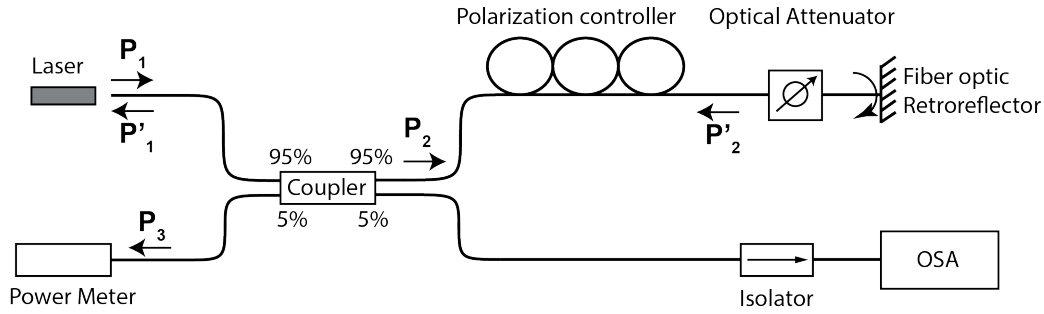


Fig. 5.11. Presentation of the setup used to test our lasers under external optical feedback

cavity, it remained possible to tune it for a given amount of feedback using the polarization controller.

5.5.2 Results and discussion

The resistance to external feedback of conventional and complex-coupled DFB lasers was measured using the setup presented earlier. The lasers seem to be more resistant to external optical feedback as the injection current increases, as was previously reported for bulk lasers [32]. Specifically, the feedback rate at the onset of coherence collapse increases linearly with the current, and therefore with the emission power.

Index-Coupled DFB lasers

Figure 5.12 presents the feedback resistance of the fabricated 3rd order index-coupled DFB lasers. Among the available samples, only few IC DFB lasers were in proper condition to be measured, as the monomode operation was not present over a wide enough current range for all of them. The results obtained for the few remaining working lasers are however very good, with resistance to Optical Return Losses above -20dB at almost every injection current. This good resistance makes them compatible with the IEEE 802.3 standard for isolator free operation. Such good resistance can be surprising, but is in good agreement with results reported in the literature [38]. Lowery [39] reported the appearance of coherence collapse in index-coupled DFB lasers with coupling constants of $\kappa L = 3.0$, for feedback rate of -27dB. This suggests that our kappa is high, although we acknowledged that the comparison may be risky.

The variation of dielectric grating amplitude does not seem to impact the resistance of IC DFB lasers to external feedback, as the data are quite similar along the associated laser design number.

Gain-Coupled DFB lasers

In his theoretical study on the resistance to external feedback of gain-coupled DFB lasers, Favre comes to the conclusion that the feedback sensitivity of GC DFB lasers is comparable to that of IC DFB lasers for weak feedback ratio [40]. The conclusions of Alam et al. on the subject are a somehow more contrasted [41], as they found that IC DFB lasers with high coupling strength and $\lambda/4$ phase shift were less sensitive to external optical feedback than GC DFB lasers.

Figure 5.13 presents the feedback sensitivity measured from GC DFB lasers working at first (left) and third (right) order. The relative position between curves gives an insight of the

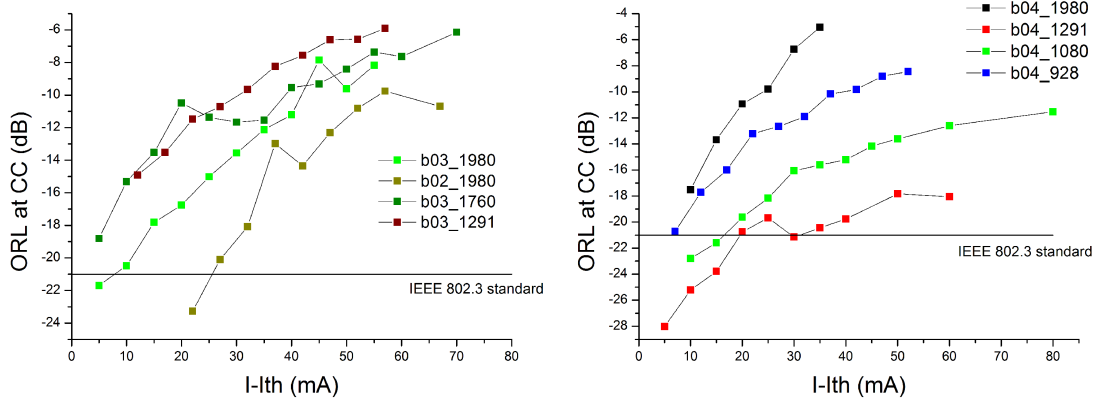


Fig. 5.12. Resistance to external feedback of 250nm (b02), 500nm (b03) and 1 micron (b04) grating amplitude IC DFB lasers

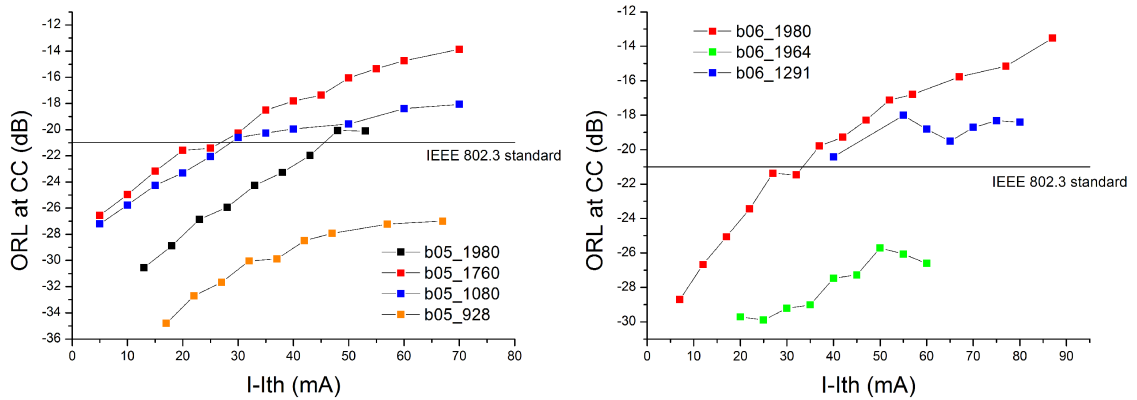


Fig. 5.13. Resistance to external feedback of first (b05) and third (b06) order GC DFB lasers

comparative feedback resistance between the lasers. The most resistant lasers have the highest Optical Return Losses at Coherence Collapse. Results are comparable between the two cases, although third order gratings tend to have less stability, and chaotic behavior under external feedback. To our knowledge, no consistent study has been reported on the resistance to external feedback of third order GC DFB lasers. As third order GC DFB lasers were underperforming in terms of emission power and spectrum, they can not be well represented here. The graphic on the right hand side shows that lasers tend to be more resistant to external feedback as their cavity length is longer, which is consistent with observation made in literature [35, 42]. The data presented in figure 5.12 and 5.13 show a much better feedback immunity for IC DFB lasers compared to their GC counterpart, with typical increase in feedback resistance of 6dB to 12dB for IC DFB lasers for similar cavity length.

Complex-Coupled DFB lasers

The resistance of Complex-Coupled DFB lasers to external optical feedback was tested under the same protocol as conventional DFB lasers. We are here interested in observing the added value of both gain and index coupling combination to the resistance to external feedback, and potential asymmetry in this resistance depending on the gratings relative

phase. Indeed, such behavior could be the expression of PT symmetric behavior of the grating action, resulting from the difference in coupling between forward-to-backward and backward-to-forward waves.

In their recent study, Ke et al. evaluate the effects of external optical feedback on a PT symmetric DFB laser from the induced change in lasing wavelength, reduction in SMSR and eye-diagram performances [43]. From the comparison with conventional IC, GC and phase shifted IC DFB lasers, they found that PTS DFB lasers have an improved operation under external optical feedback, judging by the three aforementioned criteria. One reason argued to explained this improved resistance is that the asymmetry brought by the shift between real and imaginary parts of index induces a weaker reflection, expected to have less impact on the steady-state lasing condition.

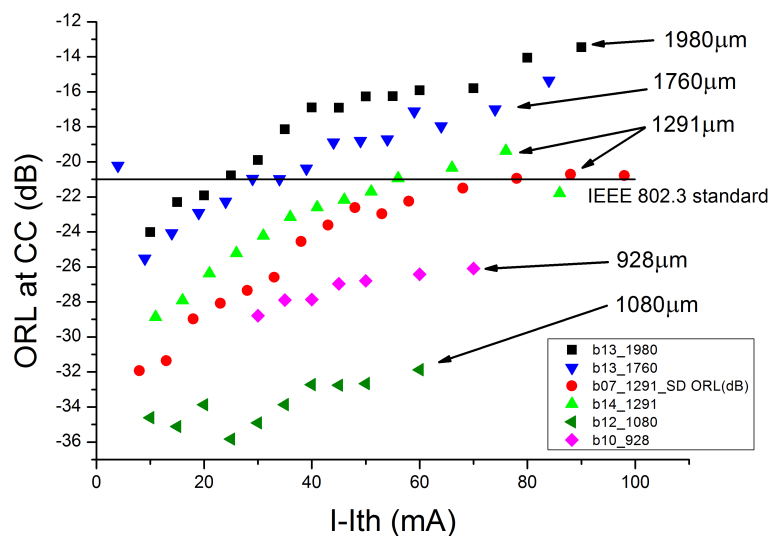


Fig. 5.14. Resistance to external feedback of CC DFB lasers of difference cavity length

The global feedback rate tolerated by the CC DFB lasers is in the range of what was observed previously on GC DFB lasers. However, the variation of feedback resistance among the population of these lasers is quite high, few of them being poorly resistant with average ORL at CCL of around -35dB, when others are in good agreement with the isolator free IEEE 802.3 standard, with ORL at CCL over -21dB.

Figure 5.14 is a good example of several samples showing a wide range of performances of CC DFB lasers under external optical feedback, depending on their cavity length. The tolerated amount of returning light inside the cavity seems to increase with the cavity length of the lasers. Such observation on the effect of cavity length on the tolerance of DFB and FP lasers were already reported in the literature [35, 42, 44].

Some lasers could be identified for their good resistance to external optical feedback. Indeed, the bars measured within this work presented one or two lasers outperforming the others in terms of feedback resistance, depending on the nominal phase shift between gratings. A specific phase shift value between grating types thus seems to increase the immunity to external reflections. This observation underpins the idea of Ke et al. for which one direction of external feedback propagation should be less detrimental for the laser operation, due to the difference in reflection of the asymmetric grating. For those lasers, the operation remains stable and coherent at higher feedback ratio values compared to

GC DFB lasers. The isolator free requirement of -21 dB ORL resistance is achieved for most of them, throughout a large current range.

To test the hypothesis of feedback resistance due to the expression of PT-symmetry, the lasers were tested with external reflection in both directions. The denominations "SU" and "SD" refers to measurements performed on opposite facets, therefore corresponding to external feedback propagation taking place in opposite directions.

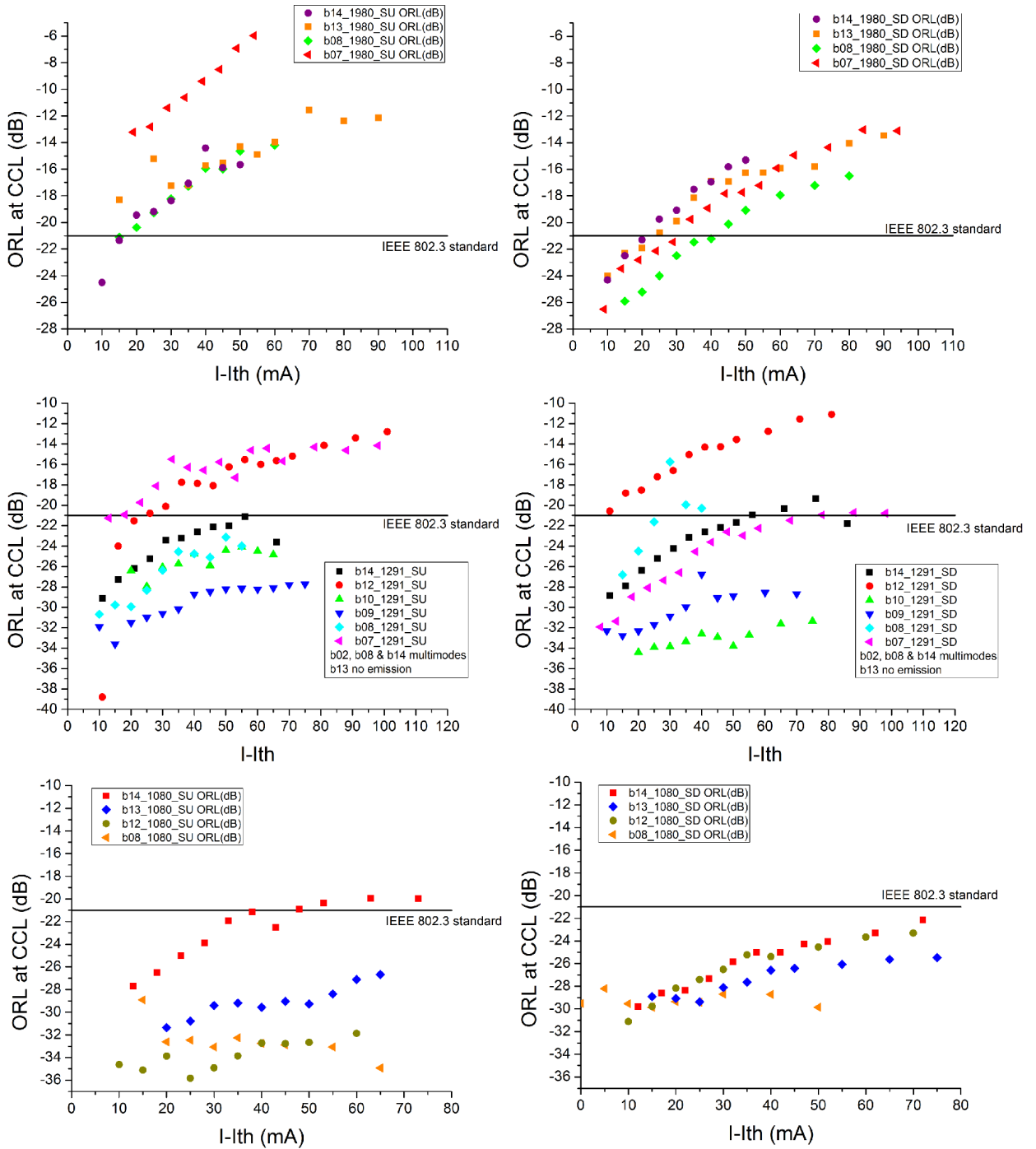


Fig. 5.15. Resistance to external feedback of CC DFB lasers in opposite directions

Similarly to the discussion on spectral emission or its intensity, we were particularly interested here in forming an indicator presenting the feedback resistance of our lasers, to compare CC DFB lasers belonging to the same sample. As figure 5.16 shows, the linear

representation of the ORL rate at the onset of coherence collapse of our lasers forms a straight line vs $(I-I_{th})$, as previously observed on conventional GC DFB lasers [44]. As steepest slopes are associated with better feedback resistance, it is thus a good indicator to evaluate the resistance of our lasers to external optical feedback. We will thereafter consider the slope as a figure of merit, and discuss the potential influence of the nominal phase shift on the feedback resistance of the CC DFB lasers.

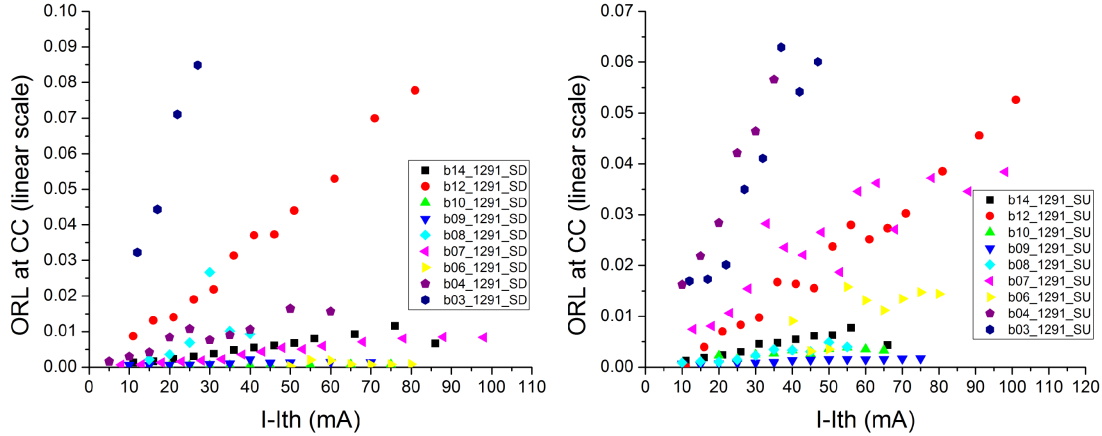


Fig. 5.16. Resistance to external feedback of first CC DFB lasers in opposite directions on linear scale

Unfortunately, from the repetition of measurements, manipulation and continuous operation, a substantial number of lasers were damaged in the process of data acquisition. To this can be added the fact that the resistance to external feedback of multimode lasers were very often not measured, as these lasers were considered as not performing well enough.

Consequently 4 devices remained for feedback resistance comparison: a_999, b_1980, b_1291 and b_1080. If lasers of a_999 do not demonstrate any laser outperforming others, with a good resistance of lasers to external feedback of 3 lasers, we observe that the cases of b_1980, b_1291 and b_1080 are different. For these samples, one laser is much more resistant to external feedback than its neighbors, with a slope of its ORL versus intensity curve at least twice steeper than the rest of lasers belonging to the same sample. Furthermore, the best performing lasers show an apparent unidirectional behavior, with asymmetric feedback resistance.

The observed asymmetry possibly originates from the expression of Parity-Time symmetry, as the difference in mode propagation impacts the amount of loss and gain seen by the propagating mode. This hypothesis must however be nuanced as it was found that DFB lasers can demonstrate variations in their resistance to external optical feedback depending on their facet phase [45].

Figure 5.17 presents the evolution of the figure of merit discussed previously. The missing laser numbers are associated with lasers that either stopped working or shown multimode spectrum and/or low emission power. In the present case, b13_1291, a09_999, b09_1080, b10_1080 and b11_1080 were multimode, and a11_999, b11_1980 were not working or with very low output power. Here also, "SU" and "SD" denominations are labels corresponding to the emission facet, and is similar for the entire data set.

Lasers b14_1080, b12_1291, and b07_1980 are the lasers most resistant to external feedback, with ORL slope twice as big as their neighbors. The difference of SU and SD emis-

sion facets of the outperforming lasers impacts the ORL slope by a factor two. Laser b07_-1980 is the most resistant laser measured, with ORL rate above -14dB at coherence collapse.

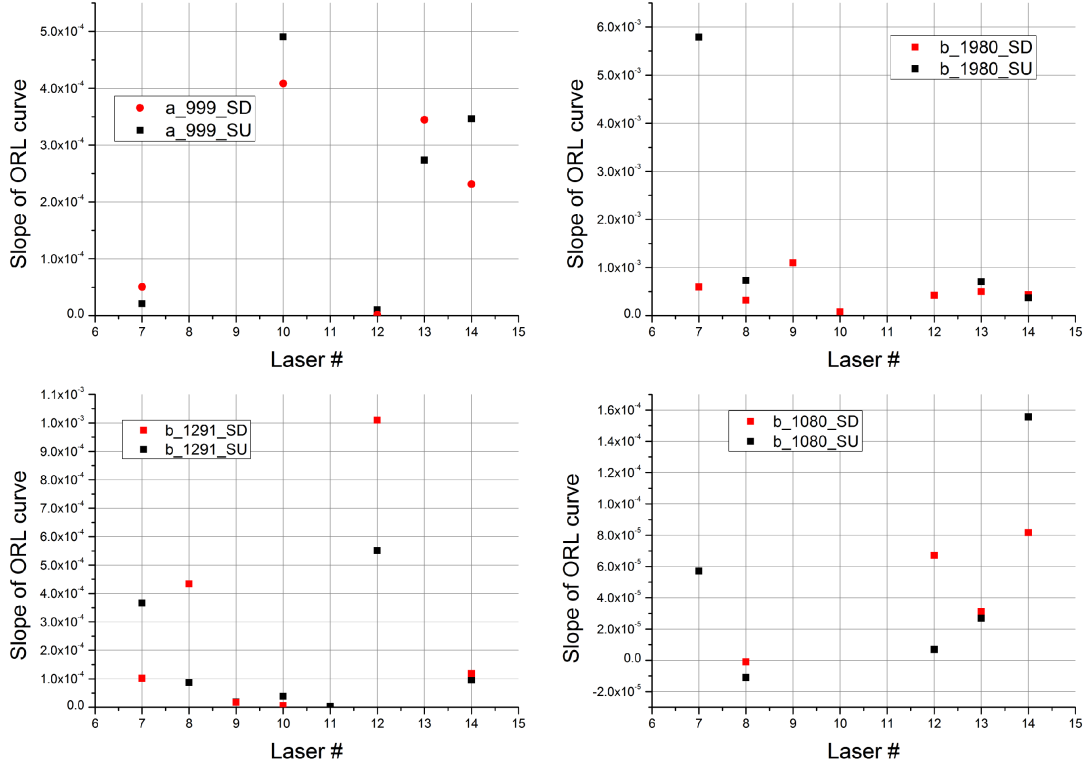


Fig. 5.17. Figure of merit of feedback versus current characteristic for several samples of complex-coupled DFB lasers

To evaluate the natural asymmetry of the feedback tolerance of CC DFB lasers, we compare them to the corresponding conventional DFB lasers. Figure 5.18 presents the slope value of the feedback versus current characteristic for IC (lasers 3 and 4), first (laser 5) and third (laser 6) GC DFB. Samples of 1080 μm , 1291 μm and 1980 μm cavity length are presented.

The 1980 μm cavity length lasers present important differences between feedback directions with factor of up to 40 in linear scale, proving that asymmetry can be found in DFB lasers with metallic or dielectric modulations alone. However, samples 1080 and 1291, of shorter cavity length, show symmetric feedback performances with similar slope values in both SU and SD cases.

Considering the small number of data, results should be considered carefully. Indeed, we could on one hand consider that sample 1980 demonstrate systematic asymmetry, possibly arising from the cleaving of the sample, which could disqualify the sample of study. In the meantime, b04_1291 and b03_1291 show relative asymmetry in their feedback resistance as well. The symmetry in feedback resistance is then only found for b04_1080, b05_1080, b06_1291 and b06_1291. The last two lasers being not tolerant to feedback, they can also be disqualified.

Finally, in the light of our experiments, the asymmetry in feedback tolerance should not be considered as the unambiguous expression of PT symmetry arising from the association of metallic and index gratings. Further investigation should however be able to deter-

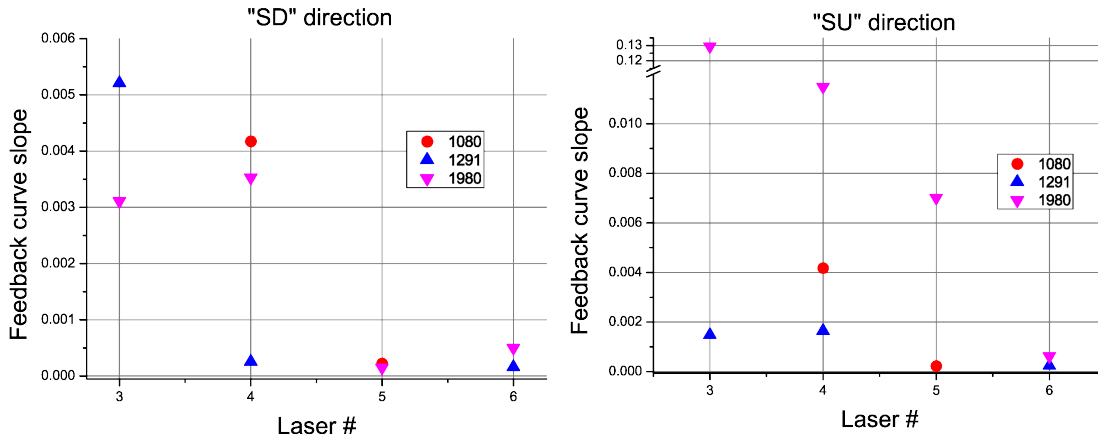


Fig. 5.18. Comparison of slope values of feedback versus current characteristic for several samples of index and gain-coupled DFB lasers depending on the direction

mine whether this unidirectional resistance can be attributed to PTS expression present in all kinds of DFB lasers, or to asymmetric facet phases increasing the resistance in only one direction.

5.6 Conclusion on the resistance to external feedback

External feedback can have a major impact on the operation of semiconductor lasers. Among the large variety of potential effects, whose presence depends on external cavity length and strength, coherence collapse is the most penalizing for the stability and purity of the laser operation. When entering this regime of external feedback, the laser linewidth broadens suddenly and drastically, and satellite modes emerge. We measured the resistance to external optical feedback of the lasers previously fabricated, by evaluating the amount of feedback requested to enter the regime of coherence collapse thanks to a dedicated setup.

From the data accumulated from our study, we observe that index-coupled DFB lasers are very resistant to external optical feedback, withstanding feedback rates above the requirement for isolator free operation, dictated by standard IEEE 802.3. This can stem from a the relatively high coupling coefficient coming from the magnitude of index modulation, determined in the first part of this chapter. Gain-coupled DFB laser were found to be less resistant to external feedback, and were in most cases unable to attain the requirements for isolator-free operation. This observation can be explained by the difference in real and imaginary parts of the index modulation, impacting the coupling coefficient. This discussion finds echo in the literature, as it was reported that IC DFB lasers with high coupling coefficient can be found to be more resistant to external feedback than their gain-coupled counterparts [39].

Complex-coupled DFB lasers were demonstrated to operate under external optical feedback compared similarly to their conventional gain-coupled counterpart. The association of real and imaginary parts of the material index does not seem to improve the feedback resistance of such lasers above that of IC DFB lasers performances though.

The study the feedback resistance evolution versus the relative phase between metallic and dielectric gratings shows that some lasers demonstrate a much higher resistance to

externally originated light than others. For several bars, between one and three lasers were found to have improved and asymmetric external feedback resistance, two potential signatures of the expression of Parity-Time symmetry. However, such differences of resistance to feedback were also observed for both index-coupled and gain-coupled DFB lasers. It is thus hard to conclude on an unambiguous relationship between the asymmetric feedback resistance of our lasers and the expression of PT symmetry.

5.7 Conclusion of the chapter

In this chapter, in-depth measurements conducted on conventional and complex-coupled DFB lasers were related. These measurements consisted in the probing of laser cavities with external coherent light source and in the study of the external feedback resistance of the lasers.

The external probing of laser cavities consisted in the measurement of the reflected and transmitted wave intensity, under the illumination of our lasers by an external tunable laser and with electrical injection a little below threshold. From these measurements, it was found that real and imaginary parts of index modulations differed from one another by an order of magnitude. If this difference does not improve the chance to witness PT symmetry effects, it is however suitable for the fabrication of practical devices, for which the amount of losses must be kept as low as possible, to show interesting operation. This investigation was also a good opportunity to exhibit potential PT symmetric unidirectional amplification in the reflection of our gratings. Lasers with metallic grating were found to show asymmetric reflection amplification. Unfortunately, the available data set is not consistent enough to conclude on the predominance of this effect in complex-coupled DFB lasers with certainty. Further investigations integrating facet phase, or the exact relative phase between gratings real and imaginary components are required to avoid misreadings of the results.

Our lasers were then tested under external feedback, to measure their tolerance under the action of returning light inside the cavity. It was observed that the resistance to external optical feedback is improved with longer cavity length, and index-coupled DFB lasers were much more resistant than their gain-coupled equivalent. Though this might seem surprising, similar observations are reported in the literature for IC DFB lasers with high coupling constant.

By studying the resistance to external feedback of CC DFB lasers belonging to the same laser bar, substantial differences were observed in the amount of feedback tolerated by the lasers depending on their grating relative phase. CC DFB lasers with enhanced tolerance to external optical feedback were measured, with coherence collapse appearing for feedback ratio higher than 6dB above GC DFB lasers values. Beside this variation in feedback resistance, the most resistant lasers were also found to be more tolerant in a given direction. Although, it was again not possible to attribute this signature to the simultaneous presence of metallic and dielectric gratings, as similar results could be found on IC and GC DFB lasers.

with respect to our general target and to the rationale of this thesis work, few complex-coupled DFB lasers were found to operate with both an increased resistance to external feedback, as well as an asymmetric amplification of the light in reflection. These two signatures can be thought to originate from the expression of Parity-Time symmetry, for specific gratings relative phase. This result is particularly interesting, as we previously

found that specific relative phase shift could be associated to a higher emission power and improved SMSR value. In particular, lasers previously reported for their remarkable performances showed good feedback resistance and asymmetry.

However, similar asymmetry in feedback tolerance could be found in so-called purely index or gain-coupled DFB lasers. Though these observations are not in contradiction with the involvement of PTS -as such gratings represent specific cases of PT-symmetry for which one of the index modulation component is equal to zero-, facet phases can also impact the effects of external radiation on the laser cavity. To dismiss this argument or otherwise clarify the situation, further in-depth study needs to be performed, with either known or suppressed facet phases.

5.8 Références

- [1] R. Regener and W. Sohler. Loss in low-finesse Ti:LiNbO_3 optical waveguide resonators. *Applied Physics B*, 36(3):143–147, Mar 1985. ISSN 1432-0649. doi: 10.1007/BF00691779. URL <https://doi.org/10.1007/BF00691779>. 93
- [2] E. V. K. Rao, Y. Gottesman, M. Allovon, E. Vergnol, D. Sigogne, A. Talneau, H. Sik, S. Slempek, B. Theys, and J. Chevallier. A significant reduction of propagation losses in ingaasp-inp buried-stripe waveguides by hydrogenation. *IEEE Photonics Technology Letters*, 10(3):370–372, March 1998. ISSN 1041-1135. doi: 10.1109/68.661413. 94
- [3] Gonghai Liu, Gongyuan Zhao, Junqiang Sun, Dingshan Gao, Qiaoyin Lu, and Weihua Guo. Experimental demonstration of dfb lasers with active distributed reflector. *Opt. Express*, 26(23):29784–29795, Nov 2018. doi: 10.1364/OE.26.029784. URL <http://www.opticsexpress.org/abstract.cfm?URI=oe-26-23-29784>. 94, 97
- [4] Max Born, Emil Wolf, A. B. Bhatia, P. C. Clemmow, D. Gabor, A. R. Stokes, A. M. Taylor, P. A. Wayman, and W. L. Wilcock. *Principles of Optics: Electromagnetic Theory of Propagation, Interference and Diffraction of Light*. Cambridge University Press, 7 edition, 1999. doi: 10.1017/CBO9781139644181. 95
- [5] H. Kogelnik and C. V. Shank. Stimulated emission in a periodic structure. *Applied Physics Letters*, 18(4):152–154, 1971. doi: <http://dx.doi.org/10.1063/1.1653605>. URL <http://scitation.aip.org/content/aip/journal/apl/18/4/10.1063/1.1653605>. 96
- [6] Y. Hirayama, H. Okuda, H. Furuyama, J. Kinoshita, and M. Nakamura. Determination of coupling coefficient of dfb lasers by a newly proposed method. *Electronics Letters*, 23(3):101–103, January 1987. ISSN 0013-5194. doi: 10.1049/el:19870072. 96
- [7] K. Kihara, H. Soda, H. Ishikawa, and H. Imai. Evaluation of the coupling coefficient of a distributed feedback laser with residual facet reflectivity. *Journal of Applied Physics*, 62(4):1526–1527, 1987. doi: 10.1063/1.339618. URL <https://doi.org/10.1063/1.339618>. 96
- [8] G. B. Morrison, D. T. Cassidy, and D. M. Bruce. Facet phases and sub-threshold spectra of dfb lasers: spectral extraction, features, explanations and verification. *IEEE Journal of Quantum Electronics*, 37(6):762–769, June 2001. ISSN 0018-9197. doi: 10.1109/3.922773. 96
- [9] G. B. Morrison and D. T. Cassidy. Improving the ability of a distributed feedback laser transfer-matrix model to fit to spectra from distributed-feedback lasers. *IEEE Photonics Technology Letters*, 12(7):768–770, July 2000. ISSN 1041-1135. doi: 10.1109/68.853494. 96
- [10] C. Henry. Performance of distributed feedback lasers designed to favor the energy gap mode. *IEEE Journal of Quantum Electronics*, 21(12):1913–1918, December 1985. ISSN 0018-9197. doi: 10.1109/JQE.1985.1072611. 96
- [11] N. Matuschek, F. X. Kartner, and U. Keller. Exact coupled-mode theories for multilayer interference coatings with arbitrary strong index modulations. *IEEE Journal of Quantum Electronics*, 33(3):295–302, March 1997. ISSN 0018-9197. doi: 10.1109/3.555995. 97

- [12] Kamal Muhieddine, Anatole Lupu, Eric Cassan, and Jean-Michel Lourtioz. Proposal and analysis of narrow band transmission asymmetric directional couplers with bragg grating induced phase matching. *Opt. Express*, 18(22):23183–23195, Oct 2010. doi: 10.1364/OE.18.023183. URL <http://www.opticsexpress.org/abstract.cfm?URI=oe-18-22-23183>. 97
- [13] Roy Lang and Kohroh Kobayashi. External optical feedback effects on semiconductor injection laser properties. *IEEE Journal of Quantum Electronics*, 16(3):347–355, 1980. 100
- [14] R. Broom, E. Mohn, C. Risch, and R. Salathe. Microwave self-modulation of a diode laser coupled to an external cavity. *IEEE Journal of Quantum Electronics*, 6(6):328–334, June 1970. ISSN 0018-9197. doi: 10.1109/JQE.1970.1076461. 100
- [15] T. Morikawa, Y. Mitsuhashi, J. Shimada, and Y. Kojima. Return-beam-induced oscillations in self-coupled semiconductor lasers. *Electronics Letters*, 12(17):435–436, August 1976. ISSN 0013-5194. doi: 10.1049/el:19760331. 100
- [16] Ch. Risch and C. Voumard. Self-pulsation in the output intensity and spectrum of gaas-algaas cw diode lasers coupled to a frequency-selective external optical cavity. *Journal of Applied Physics*, 48(5):2083–2085, 1977. doi: 10.1063/1.323922. URL <https://doi.org/10.1063/1.323922>. 100
- [17] N. Chinone, K. Aiki, and R. Ito. Stabilization of semiconductor laser outputs by a mirror close to a laser facet. *Applied Physics Letters*, 33(12):990–992, 1978. doi: 10.1063/1.90264. URL <https://doi.org/10.1063/1.90264>. 100
- [18] O. Hirota and Y. Suematsu. Noise properties of injection lasers due to reflected waves. *IEEE Journal of Quantum Electronics*, 15(3):142–149, March 1979. ISSN 0018-9197. doi: 10.1109/JQE.1979.1069975. 100
- [19] K. Kikuchi and T. Okoshi. Simple formula giving spectrum-narrowing ratio of semiconductor-laser output obtained by optical feedback. *Electronics Letters*, 18(1): 10–12, January 1982. ISSN 0013-5194. doi: 10.1049/el:19820008. 100
- [20] G. Agrawal. Line narrowing in a single-mode injection laser due to external optical feedback. *IEEE Journal of Quantum Electronics*, 20(5):468–471, May 1984. ISSN 0018-9197. doi: 10.1109/JQE.1984.1072420. 100
- [21] E. Patzak, H. Olesen, A. Sugimura, S. Saito, and T. Mukai. Spectral linewidth reduction in semiconductor lasers by an external cavity with weak optical feedback. *Electronics Letters*, 19(22):938–940, October 1983. ISSN 0013-5194. doi: 10.1049/el:19830640. 100
- [22] R. O. Miles, A Dandridge, A. B. Tveten, H. F. Taylor, and T. G. Giallorenzi. Feedback-induced line broadening in cw channel-substrate planar laser diodes. *Applied Physics Letters*, 37(11):990–992, 1980. doi: 10.1063/1.91744. URL <https://doi.org/10.1063/1.91744>. 100
- [23] L. Goldberg, H. F. Taylor, A. Dandridge, J. F. Weller, and R. O. Miles. Spectral characteristics of semiconductor lasers with optical feedback. *IEEE Transactions on Microwave Theory and Techniques*, 30(4):401–410, Apr 1982. ISSN 0018-9480. doi: 10.1109/TMTT.1982.1131081. 100

- [24] G. Acket, D. Lenstra, A. Den Boef, and B. Verbeek. The influence of feedback intensity on longitudinal mode properties and optical noise in index-guided semiconductor lasers. *IEEE Journal of Quantum Electronics*, 20(10):1163–1169, October 1984. ISSN 0018-9197. doi: 10.1109/JQE.1984.1072281. 100
- [25] J. H. Osmundsen, B. Tromborg, and H. Olesen. Experimental investigation of stability properties for a semiconductor laser with optical feedback. *Electronics Letters*, 19(25):1068–1070, December 1983. ISSN 0013-5194. doi: 10.1049/el:19830725. 100
- [26] H. Li, J. Ye, and J. G. McInerney. Detailed analysis of coherence collapse in semiconductor lasers. *IEEE Journal of Quantum Electronics*, 29(9):2421–2432, Sept 1993. ISSN 0018-9197. doi: 10.1109/3.247700. 100
- [27] Takaaki Mukai and Kenju Otsuka. New route to optical chaos: Successive-subharmonic-oscillation cascade in a semiconductor laser coupled to an external cavity. *Phys. Rev. Lett.*, 55:1711–1714, Oct 1985. doi: 10.1103/PhysRevLett.55.1711. URL <https://link.aps.org/doi/10.1103/PhysRevLett.55.1711>. 100
- [28] Joachim Sacher, Wolfgang Elsässer, and Ernst O. Göbel. Intermittency in the coherence collapse of a semiconductor laser with external feedback. *Phys. Rev. Lett.*, 63:2224–2227, Nov 1989. doi: 10.1103/PhysRevLett.63.2224. URL <https://link.aps.org/doi/10.1103/PhysRevLett.63.2224>. 100
- [29] C. Henry and R. Kazarinov. Instability of semiconductor lasers due to optical feedback from distant reflectors. *IEEE Journal of Quantum Electronics*, 22(2):294–301, February 1986. ISSN 0018-9197. doi: 10.1109/JQE.1986.1072959. 100
- [30] D. Lenstra, B. Verbeek, and A. Den Boef. Coherence collapse in single-mode semiconductor lasers due to optical feedback. *IEEE Journal of Quantum Electronics*, 21(6):674–679, June 1985. ISSN 0018-9197. doi: 10.1109/JQE.1985.1072725. 100, 102
- [31] S. L. Woodward, T. L. Koch, and U. Koren. The onset of coherence collapse in dbr lasers. *IEEE Photonics Technology Letters*, 2(6):391–394, June 1990. ISSN 1041-1135. doi: 10.1109/68.56596. 100
- [32] R Tkach and AR Chraplyvy. Regimes of feedback effects in 1.5- μm distributed feedback lasers. *Journal of Lightwave technology*, 4(11):1655–1661, 1986. 100, 101, 104
- [33] B. R. Clarke. The effect of reflections on the system performance of intensity modulated laser diodes. *Journal of Lightwave Technology*, 9(6):741–749, June 1991. ISSN 0733-8724. doi: 10.1109/50.81977. 101
- [34] N. Schunk and K. Petermann. Stability analysis for laser diodes with short external cavities. *IEEE Photonics Technology Letters*, 1(3):49–51, March 1989. ISSN 1041-1135. doi: 10.1109/68.87893. 101
- [35] N. Schunk and K. Petermann. Numerical analysis of the feedback regimes for a single-mode semiconductor laser with external feedback. *IEEE Journal of Quantum Electronics*, 24(7):1242–1247, July 1988. ISSN 0018-9197. doi: 10.1109/3.960. 101, 105, 106

- [36] IEEE. Ieee standard for information technology- telecommunications and information exchange between systems- local and metropolitan area networks- specific requirements part 3: Carrier sense multiple access with collision detection (csma/cd) access method and physical layer specifications amendment: Media access control (mac) parameters, physical layers, and management parameters for 10 gb/s operation. *IEEE Std 802.3ae;2002 (Amendment to IEEE Std 802.3-2002)*, pages 1–516, 2002. doi: 10.1109/IEEESTD.2002.94131. 102
- [37] IEEE. Ieee standard for information technology- local and metropolitan area networks- specific requirements- part 3: Csma/cd access method and physical layer specifications amendment 4: Media access control parameters, physical layers, and management parameters for 40 gb/s and 100 gb/s operation. *IEEE Std 802.3ba-2010 (Amendment to IEEE Standard 802.3-2008)*, pages 1–457, June 2010. doi: 10.1109/IEEESTD.2010.5501740. 102
- [38] F. Favre. Theoretical analysis of external optical feedback on dfb semiconductor lasers. *IEEE Journal of Quantum Electronics*, 23(1):81–88, January 1987. ISSN 0018-9197. doi: 10.1109/JQE.1987.1073195. 104
- [39] A. J. Lowery and D. Novak. Performance comparison of gain-coupled and index-coupled dfb semiconductor lasers. *IEEE Journal of Quantum Electronics*, 30(9):2051–2063, Sept 1994. ISSN 0018-9197. doi: 10.1109/3.309864. 104, 110
- [40] F. Favre. Sensitivity to external feedback for gain-coupled dfb semiconductor lasers. *Electronics Letters*, 27(5):433–435, Feb 1991. ISSN 0013-5194. doi: 10.1049/el:19910274. 104
- [41] M. F. Alam, M. A. Karim, and S. Islam. Effects of structural parameters on the external optical feedback sensitivity in dfb semiconductor lasers. *IEEE Journal of Quantum Electronics*, 33(3):424–433, March 1997. ISSN 0018-9197. doi: 10.1109/3.556012. 104
- [42] O. Carroll, S. P. Hegarty, G. Huyet, B. Corbett, and D. O’Brien. Length dependance of feedback sensitivity of inas/gaas quantum dot lasers. In *EQEC '05. European Quantum Electronics Conference, 2005.*, pages 23–, June 2005. doi: 10.1109/EQEC.2005.1567195. 105, 106
- [43] Cheng Ke, Xun Li, and Yanping Xi. Parity-time symmetric complex-coupled distributed feedback laser with excellent immunity to external optical feedback. *AIP Advances*, 7(3):035010, 2017. doi: 10.1063/1.4978447. URL <http://dx.doi.org/10.1063/1.4978447>. 106
- [44] S. Azouigui, B. Dagens, F. Lelarge, J. Provost, D. Make, O. Le Gouezigou, A. Accard, A. Martinez, K. Merghem, F. Grillot, O. Dehaese, R. Piron, S. Loualiche, Q. Zou, and A. Ramdane. Optical feedback tolerance of quantum-dot- and quantum-dash-based semiconductor lasers operating at 1.55 μ m. *IEEE Journal of Selected Topics in Quantum Electronics*, 15(3):764–773, May 2009. ISSN 1077-260X. doi: 10.1109/JSTQE.2009.2013870. 106, 108
- [45] F. Grillot. On the effects of an antireflection coating impairment on the sensitivity to optical feedback of ar/hr semiconductor dfb lasers. *IEEE Journal of Quantum Electronics*, 45(6):720–729, June 2009. ISSN 0018-9197. doi: 10.1109/JQE.2009.2013155. 108

Conclusions and perspectives

During this work, we investigated the design, fabrication and characterization of complex-coupled (CC) distributed feedback (DFB) lasers, with the ambition to apply the concept of Parity-Time symmetry for practical devices. Because of fabrication constraints, the lasers were designed to operate at third order and for different wavelengths covering the optical gain spectrum in the $1.55\mu\text{m}$ fiber optic window. The index modulation was brought for the real part by the corrugation of the laser waveguide, and for its imaginary part by an absorbing metallic grating.

The effective indices, determining the Bragg period, were calculated using a modal approach. A simple model built from successive layers inducing the real and imaginary part of the index periodic variation was simulated using Ables matrix method. The mode evolution of conventional index and gain coupled (IC and GC respectively), as well as complex-coupled (CC) DFB lasers were simulated using this formalism, showing the mode selection inside the laser cavity. The study of the effects the relative phase between real and imaginary parts of the material index (supposedly corresponding to the phase difference between the two gratings) has on the modes inside the laser cavity revealed the existence of an asymmetric response in the case both indices components are not in or out of phase. The particular phase shift of a quarter of a grating period is of great interest, as the asymmetry is strongest. In absence of facet reflections, coherent unidirectional amplification is even possible. Despite the interest raised by this rigorous application of PT-symmetry, the choice was made to focus on the objective to realize a high performing laser. Throughout this work we had to deal with laser facet reflections and unbalanced real and imaginary parts of the index because of the high absorption brought by the metallic grating.

It was hence decided to achieve complex-coupled DFB lasers with stronger dielectric grating and limited loss induced metallic grating. Series of 8 CC DFB lasers with $1/8$ grating phase shift increment were fabricated, to ease fabrication tolerances and monitor the effect of the relative phase on laser emission. A set of conventional index and gain coupled DFB lasers was appended to the fabrication process, to serve as control samples and help determine the gratings characteristics.

The fabrication process was carried out at C2N, and involved standard building blocks for Photonic Integrated Circuits (PIC) fabrication, relying mainly on electron-beam lithography, Induced Coupled Plasma (ICP) etching and optical lithography to name but a few. The main challenge of the fabrication process was the development of an ICP etching process optimized for the definition of a corrugated waveguide. The issue was then to achieve low roughness vertical sidewalls inside narrow trenches of opening width down to 360nm . Two processes gave good results with Cl_2 and HBr based etching chemistry. For gas availability reasons, the HBr process was used to etch the final sample.

The light current (LI) characteristic and optical spectrum of the devices was investigated.

Index-coupled DFB lasers gave the lower threshold and higher output power, with threshold currents ranging from 20mA to 25mA, and output power at 200mA over 15mW. Third order gain-coupled lasers were found to be comparatively less performant than their first order counterpart, owing to the increased absorption brought by the interaction of third order loss grating with the cavity standing wave. A significant amount of the third order GC DFB lasers were not able to reach laser emission due to this increase in cavity losses. Interestingly, despite this high absorption, the third order complex-coupled DFB laser demonstrated light current characteristics comparable to first order gain-coupled DFB laser, with typical threshold currents of 50mA to 70mA, and output power at 200mA ranging from 7mW to 12mW. The variation of the light current characteristics of CC DFB lasers follows a pattern, which can be linked to the variation of the overlap between the metallic and dielectric grating.

The laser spectrum was measured in continuous wave operation, for injection currents ranging from 20mA to 250mA and above. The best single frequency operation was obtained from first order GC and third order CC DFB lasers, where the monomodality was maintained for current above 250mA, with very high Side Mode Suppression Ratio (SMSR) exceeding 50dB. The nominal gratings relative phase seemed to impact the SMSR value of the lasers, as a pattern emerged in the CC DFB lasers population. On the other hand, IC DFB lasers could not stand injection current above 150mA while maintaining a single frequency operation.

From our observations, the combination of gain and index grating results in the improvement of light current characteristic, reaching lower threshold and higher output power compared to standard third order GC DFB lasers, as well as single-frequency operation, with higher monomode stability in terms of injection current range compared to third order IC DFB lasers.

The transmission and reflection response of the fabricated lasers were probed under an external tunable laser. From these sub-threshold measurements, the cavity losses could be computed, from which the modulation magnitude of the imaginary part of the index Δn_{Im} could be deduced. From the comparison with the simulations results, the width of the stop band led to the determination of the modulation magnitude of the real part of the index Δn_{Re} . The difference between modulation of index components reached one order of magnitude with values of $2 \cdot 10^{-3}$ and $2 \cdot 10^{-4}$ for respectively Δn_{Re} and Δn_{Im} . The same experimental setup was used to monitor the reflection and transmission characteristics of the laser cavities in both propagation directions. Unidirectional amplification of reflection was observed for GC and CC DFB lasers in equal proportions. This effect can be the signature of PT-symmetry in CC and GC DFB lasers, though facet phase reflection can interfere with the measurements. Furthermore, simulation results showed the possibility of relative asymmetric amplification as soon as metallic and index gratings are neither in nor out of phase, which hence should not be attributed to PT-symmetry alone.

One of the assets of PT-symmetry in its application to DFB lasers is the asymmetric loss profile seen by a contra-propagative wave. This property can be seen as a powerful tool to avoid the dramatic impact of external feedback reflections, causing drastic degradation of the laser coherence and stability. The robustness of gain, index and complex-coupled DFB lasers with varying phase shift between grating types was tested against external optical feedback in both propagation directions, by determination of the onset of Coherence Collapse (CCL). If the feedback resistance of CC DFB lasers was improved with regards to their gain-coupled counterparts, index-coupled DFB lasers were found to be the most re-

sistant lasers under external feedback, with onset of CCL above the -21 dB IEEE standard requirement for isolator-free operation. From our observations, the combination of loss and index gratings does not improve the resistance of DFB lasers to external optical feedback with regards to the performances obtained from IC DFB lasers. However, our data show that the nominal relative phase between metallic and dielectric gratings impacts the onset of CCL, as one or two feedback tolerant lasers emerged from the CC DFB lasers of a same bar. Further investigation must be conducted to determine the importance of the role played by facet reflections and facet phase on the resistance of our lasers to external optical feedback, and the asymmetry of this resistance.

The perspective of this work would consist in fabricating complex-coupled DFB lasers operating at first order. This idea is motivated by the difference observed in emission characteristics of first and third order GC DFB lasers, as higher output power, lower threshold, and stable single frequency operation was observed at first order and unsatisfactory at third order. The main challenge remains technological, in particular for the etching of short period index grating. To avoid such complications, index and loss grating of respectively first and third orders can be fabricated, hence avoiding technological complication. An additional work can be conducted on the observation of PT-symmetric effects in absence of facet reflections. The laser operation would not be possible due to insufficient internal feedback but asymmetric amplification in reflection could be demonstrated.

Appendix A

Abeles Matric model for the simulation of modes inside the laser cavity

A.1 Abeles Matrix Formalism

To introduce Abeles formalism we start with the example of a plane wave falling on a single layer i of index n_i . The geometry is presented figure A.1, the layer is situated at z between 0 and z_{max} , and considered as infinite along x and y axis. The plane wave of pulsation ω is falling at normal incidence, traveling along Oz .

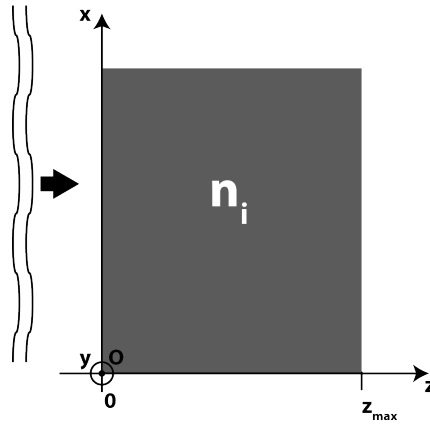


Fig. A.1. Presentation of the system geometry

Inside the layer, electric and magnetic fields \vec{E} and \vec{H} are parallel to Ox and Oy respectively and can be written as:

$$\vec{E} = E_x(z)e^{-j\omega t}\vec{i} \quad (\text{A.1})$$

$$\vec{H} = H_y(z)e^{-j\omega t}\vec{j} \quad (\text{A.2})$$

Where \vec{i} and \vec{j} are the unitary vectors along Ox and Oy respectively. Maxwell's equations inside the layer give:

$$\frac{dE_x}{dz} = j\mu_i\omega H_y \quad (\text{A.3})$$

$$\frac{dH_y}{dz} = j\epsilon_i\omega E_x \quad (\text{A.4})$$

Where ϵ_i and μ_i are the permittivity and permeability of the medium of layer i. By noting $k_i = n_i\omega/c$ where c is the speed of light, we can write the differential equation satisfied by $E_x(z)$ inside layer i:

$$\frac{d^2E_x}{dz^2} + k_i^2 E_x = 0 \quad (\text{A.5})$$

The general solution of the differential equation is of the following kind:

$$\vec{E}_x(z, t) = (Ae^{-j(\omega t - k_i z)} + Be^{-j(\omega t + k_i z)})\vec{i} \quad (\text{A.6})$$

This represent the superposition of two plane waves propagating in opposite directions along Oz. The derivation of this solution and its injection in Maxwell's equation gives:

$$\vec{H}_y(z, t) = \eta_i(Ae^{-j(\omega t - k_i z)} - Be^{-j(\omega t + k_i z)})\vec{j} \quad (\text{A.7})$$

With $\eta_i = k_i / \mu_0\omega$, μ_0 being the vacuum permeability. Particularly, by looking at initial condition at $z=0$:

$$E_x(0) = A + B \quad (\text{A.8})$$

$$H_y(0) = \eta_i(A - B) \quad (\text{A.9})$$

The association of equation A.6 and A.7 gives:

$$\begin{cases} \eta_i E_x(z) + H_y(z) = 2\eta_i A e^{jk_i z} \\ \eta_i E_x(z) - H_y(z) = 2\eta_i B e^{-jk_i z} \end{cases} \quad (\text{A.10})$$

Which leads to the formulation of A and B as:

$$\begin{cases} A = \frac{1}{2}(E_x(z) + \frac{H_y(z)}{\eta_i})e^{-jk_i z} \\ B = \frac{1}{2}(E_x(z) - \frac{H_y(z)}{\eta_i})e^{jk_i z} \end{cases} \quad (\text{A.11})$$

By replacing the expression of A and B in equation A.8, we obtain:

$$\begin{cases} E_x(0) = \frac{1}{2}E_x(z)(e^{-jk_i z} + e^{jk_i z}) + \frac{1}{2}\frac{H_y(z)}{\eta_i}(e^{-jk_i z} - e^{jk_i z}) \\ H_y(0) = \frac{\eta_i}{2}E_x(z)(e^{-jk_i z} - e^{jk_i z}) + \frac{1}{2}H_y(z)(e^{-jk_i z} + e^{jk_i z}) \end{cases} \quad (\text{A.12})$$

Which can be expressed as:

$$\begin{cases} E_x(0) = \frac{1}{2}E_x(z)\cos(k_i z) - j\frac{H_y(z)}{\eta_i}\sin(k_i z) \\ H_y(0) = -j\eta_i E_x(z)\sin(k_i z) + H_y(z)\cos(k_i z) \end{cases} \quad (\text{A.13})$$

The matrix formulation linking $(E_x(0), H_y(0))$ and $(E_x(z), H_y(z))$ is then:

$$\begin{pmatrix} E_x(0) \\ H_y(0) \end{pmatrix} = \begin{pmatrix} \cos(k_i z) & -j\frac{\sin(k_i z)}{\eta_i} \\ -j\eta_i \sin(k_i z) & \cos(k_i z) \end{pmatrix} \begin{pmatrix} E_x(z) \\ H_y(z) \end{pmatrix} = M_i(z) \begin{pmatrix} E_x(z) \\ H_y(z) \end{pmatrix} \quad (\text{A.14})$$

Similarly, at any point z' of the layer i as $0 < z' < z_{max}$ and $z' \neq z$, we obtain:

$$\begin{pmatrix} E_x(0) \\ H_y(0) \end{pmatrix} = M_i(z') \begin{pmatrix} E_x(z') \\ H_y(z') \end{pmatrix} \quad (\text{A.15})$$

$$M_i(z) \begin{pmatrix} E_x(z) \\ H_y(z) \end{pmatrix} = M_i(z') \begin{pmatrix} E_x(z') \\ H_y(z') \end{pmatrix} \quad (\text{A.16})$$

$$M_i(z) \begin{pmatrix} E_x(z) \\ H_y(z) \end{pmatrix} = M_i(z') \begin{pmatrix} E_x(z') \\ H_y(z') \end{pmatrix} \quad (\text{A.17})$$

Both matrix can then be associated:

$$\begin{pmatrix} E_x(z) \\ H_y(z) \end{pmatrix} = M_i^{-1}(z) M_i(z') \begin{pmatrix} E_x(z') \\ H_y(z') \end{pmatrix} \quad (\text{A.18})$$

As $M_i^{-1}(z) = \begin{pmatrix} \cos(k_i z) & \frac{j}{\eta_i} \sin(k_i z) \\ j\eta_i \sin(k_i z) & \cos(k_i z) \end{pmatrix} = M_i(-z)$, by replacing in the previous equation we obtain:

$$\begin{pmatrix} E_x(z) \\ H_y(z) \end{pmatrix} = \begin{pmatrix} \cos(k_i z) & \frac{j}{\eta_i} \sin(k_i z) \\ j\eta_i \sin(k_i z) & \cos(k_i z) \end{pmatrix} \begin{pmatrix} \cos(k_i z') & -\frac{j}{\eta_i} \sin(k_i z') \\ -j\eta_i \sin(k_i z') & \cos(k_i z') \end{pmatrix} \begin{pmatrix} E_x(z') \\ H_y(z') \end{pmatrix} \quad (\text{A.19})$$

We finally obtain:

$$\begin{pmatrix} E_x(z) \\ H_y(z) \end{pmatrix} = \begin{pmatrix} \cos(k_i(z' - z)) & -\frac{j}{\eta_i} \sin(k_i(z' - z)) \\ -j\eta_i \sin(k_i(z' - z)) & \cos(k_i(z' - z)) \end{pmatrix} \begin{pmatrix} E_x(z') \\ H_y(z') \end{pmatrix} \quad (\text{A.20})$$

And gives us the transfer matrix formulation of electric and magnetic fields, for the propagation of a plane wave inside a medium i :

$$\begin{pmatrix} E_x(z) \\ H_y(z) \end{pmatrix} = M_i(z' - z) \begin{pmatrix} E_x(z') \\ H_y(z') \end{pmatrix} \quad (\text{A.21})$$

A.1.1 Application of Abeles matrix method to PT-symmetric structure

The formulation presented in the appendix gives access to the field at any point of a layer, knowing the medium and incident wave characteristics. We can now apply the same principle to a stack of multiple layers, each of different index but of similar width, as presented figure A.2.

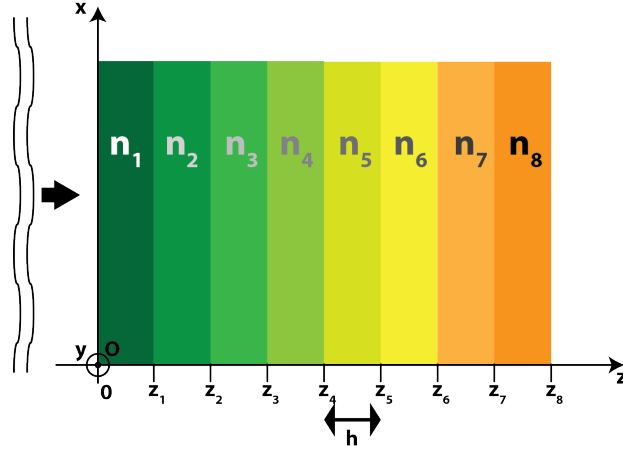


Fig. A.2. Presentation of the system of stacked layers

In this case, we can write:

$$\begin{pmatrix} E_x(0) \\ H_y(0) \end{pmatrix} = M_1(z_1) \begin{pmatrix} E_x(z_1) \\ H_y(z_1) \end{pmatrix} \quad (\text{A.22})$$

$$\begin{pmatrix} E_x(z_1) \\ H_y(z_1) \end{pmatrix} = M_2(z_2 - z_1) \begin{pmatrix} E_x(z_2) \\ H_y(z_2) \end{pmatrix} \quad (\text{A.23})$$

Consequently:

$$\begin{pmatrix} E_x(0) \\ H_y(0) \end{pmatrix} = M_1(z_1) M_1(z_2 - z_1) \begin{pmatrix} E_x(z_2) \\ H_y(z_2) \end{pmatrix} \quad (\text{A.24})$$

As result, the expression of the field at any interface of layer N at point z_N satisfies the condition:

$$\begin{pmatrix} E_x(0) \\ H_y(0) \end{pmatrix} = \prod_{i=1}^N M_i(h) \begin{pmatrix} E_x(z_N) \\ H_y(z_N) \end{pmatrix} \quad (\text{A.25})$$

Where N is an integer, $N \in [1, 4]$, and h is the layer width.

Similarly, applying the concept in equation A.22, the field inside a given layer N at position z, where $z_{N-1} < z < z_N$, satisfies the condition:

$$\begin{pmatrix} E_x(z_{N-1}) \\ H_y(z_{N-1}) \end{pmatrix} = M_N(z - z_{N-1}) \begin{pmatrix} E_x(z) \\ H_y(z) \end{pmatrix} \quad (\text{A.26})$$

$$\begin{pmatrix} E_x(0) \\ H_y(0) \end{pmatrix} = \prod_{i=1}^{N-1} M_i(h) \begin{pmatrix} E_x(z_{N-1}) \\ H_y(z_{N-1}) \end{pmatrix} \quad (\text{A.27})$$

We now have:

$$\begin{pmatrix} E_x(0) \\ H_y(0) \end{pmatrix} = \left(\prod_{i=1}^{N-1} M_i(h) \right) M_N(z - z_{N-1}) \begin{pmatrix} E_x(z) \\ H_y(z) \end{pmatrix} \quad (\text{A.28})$$

We can interestingly obtain the field at position z by reversing the expression:

$$\begin{pmatrix} E_x(z) \\ H_y(z) \end{pmatrix} = M_N(z_{N-1} - z) \left(\prod_{i=1}^{N-1} M_{N-i}(-h) \right) \begin{pmatrix} E_x(0) \\ H_y(0) \end{pmatrix} \quad (\text{A.29})$$

With $M_i(z) = \begin{pmatrix} \cos(k_i z) & -\frac{j}{\eta_i} \sin(k_i z) \\ -j\eta_i \sin(k_i z) & \cos(k_i z) \end{pmatrix}$; $k_i = n_i / (\omega c)$ and $\eta_i = k_i / (\mu_0 \omega)$.

The electric and magnetic fields in $z < 0$ are a superposition of incident and reflected waves, and for $z > 8h$, only the transmission remains. We thus have:

$$\begin{cases} E_x(0) = I + R ; H_y(0) = \eta_0(I - R) \\ E_x(4h) = T ; H_y(4h) = \eta_0 T \end{cases} \quad (\text{A.30})$$

We consider here that the stack of layers is in vacuum, initial and final medium are then characterized by $\eta = 1 / (\mu_0 c)$. We can then write the following equation for a stack of 8 layers:

$$\begin{pmatrix} I + R \\ \eta_0(I - R) \end{pmatrix} = \prod_{i=1}^8 M_i(h) \begin{pmatrix} T \\ \eta_0 T \end{pmatrix} \quad (\text{A.31})$$

From this formulation, and by noting that product of the transfer matrices of the 8 layers will be a matrix composed of coefficient m_{ij} with $(i,j) \in \{1,2\}^2$, we thus have the following set of equation connecting the incident, reflected and transmitted waves:

$$\begin{cases} I + R = m_{11}T + m_{12}\eta_0T \\ \eta_0(I - R) = m_{21}T + m_{22}\eta_0T \end{cases} \quad (\text{A.32})$$

A.1.2 Simulation of plane waves propagation through PT-symmetric stack of layers

In the previous section we were able to express a relation between incident, reflected and transmitted component of a plane wave traveling through a stack of 8 layers. In this section, we use this demonstration to simulate the propagation of a plane wave through a photonic crystal presenting a modulation of both real and imaginary parts of the index. The previous 8 layers stack is considered to be a single period of the grating, and each of these layers parameters can be tuned independently.

This way, a grating composed of the modulation of the refractive index as well as a modulation of gain and loss can be implemented through the real part and imaginary part of the material index. As one period is composed of 8 layers, 8 phase shifts between the real and imaginary index modulations can be built. Figure A.3 present the grating geometry, and examples of index components modulations that can be implemented.

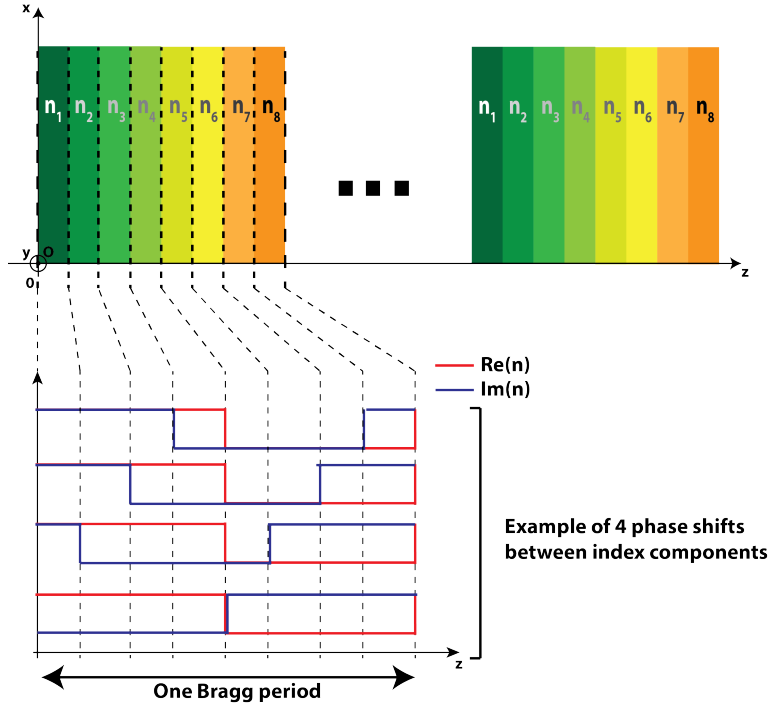


Fig. A.3. Presentation of the structure used for the simulation of transmitted and reflected waves. The grating is composed of a repetition 8 layers of the same width in which the index magnitude can be tuned independently.

The structure described above can be used to simulate the transmission and reflection properties of a grating composed of a modulation of both real and imaginary parts of the index of a material. Being able to simulate 8 phase shifts is of great interest for us as it is related to the design we decided to fabricate, and that will be dealt with in the next chapter. In order for these simulation to fit with the condition in which such Parity-Time Symmetric Distributed FeedBack (PTS DFB) lasers would be measured, it is also important to take into account the effects the cleaving will have on the transmitted and reflected waves.

The final model, presented figure A.4, is then decomposed in 3 parts: one is the core of the grating, having a whole number of grating periods, surrounded by two complementary pieces representing the laser facets. The width of facet pieces can be tuned from 0 to a full period length, each facet will therefore be potentially composed of an incomplete structure. This way any case of cleaving can be presented, and the grating can be asymmetric.

In this model, the dimensions of the core and facet is computed from the total length and the facet fraction, representing the length of the facet zones in unit of a grating period. The resulting transfer matrix of our model is:

$$M_G = M_L(h_{in}) \left(\prod_{i=1}^{N_G} M_C(h_C) \right) M_R(h_{out}) \quad (A.33)$$

M_L , M_R , h_{in} and h_{out} are here the matrix and width of the left and right facets respectively, M_C and h_C are the the matrix and width of the grating core. The transfer matrix of the left and right facet can be decomposed as following:

$$\begin{cases} M_L(h_{in}) = M_\alpha(h_{in} - (8 - \alpha)h) \left(\prod_{i=\alpha+1}^8 M_i(h) \right) & \text{if } h_{in} > h \\ M_L(h_{in}) = M_8(h_{in}) & \text{if } h_{in} < h \end{cases} \quad (A.34)$$

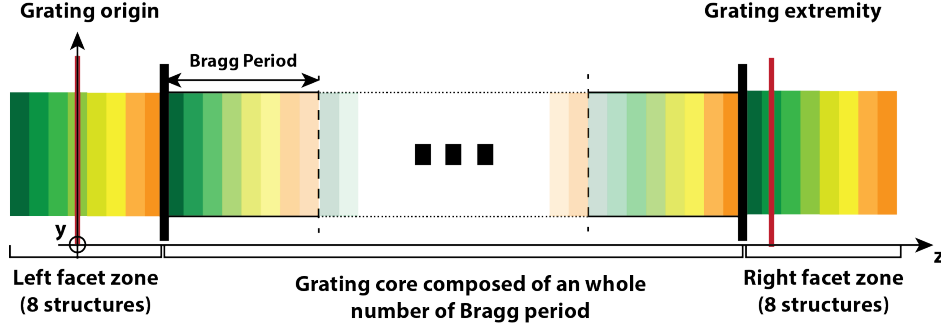


Fig. A.4. Architecture of the model used to simulate the PT-symmetric grating. Left and right facet are composed of an array of the 8 structures in which lies the origin and extremity of the grating. The core is composed of an whole number of Bragg periods composed of the 8 structures entirely.

$$\begin{cases} M_R(h_{out}) = \left(\prod_{i=1}^{\Omega-1} M_i(h)\right) M_{\Omega}(h_{out} - (8 - \Omega)h) & \text{if } h_{out} > h \\ M_R(h_{out}) = M_1(h_{out}) & \text{if } h_{out} < h \end{cases} \quad (\text{A.35})$$

Where α and Ω are the number label of input and output structures, with $(\alpha, \Omega) \in \{1, 8\}^2$. They can be mathematically determined using:

$$\begin{cases} \alpha = 8 - \left\lfloor \frac{h_{in}}{h} \right\rfloor \\ \Omega = \left\lfloor \frac{h_{out}}{h} \right\rfloor + 1 \end{cases} \quad (\text{A.36})$$

Reflection and transmission coefficient of our grating are defined as:

$$\begin{cases} r = \frac{R}{I} \\ t = \frac{T}{I} \end{cases} \quad (\text{A.37})$$

I, R T are the amplitudes of respectively the incident, reflected and transmitted waves, r and t are the reflection and transmission coefficient of the grating. M_G being a 2*2 matrix, we can label its components as m_{ij} , with $(i, j) \in \{1, 2\}^2$. We can now compute the reflection and transmission coefficient r and t using equation A.32, we obtain:

$$r = \frac{2}{m_{11} + m_{12}\eta_0 + \frac{m_{21}}{\eta_0} + m_{22}} \quad (\text{A.38})$$

$$t = \frac{m_{11} + m_{12}\eta_0 - \frac{m_{21}}{\eta_0} - m_{22}}{m_{11} + m_{12}\eta_0 + \frac{m_{21}}{\eta_0} + m_{22}} \quad (\text{A.39})$$

Where $\eta_0 = n_0 / \mu_0 c$, with n_0 as the refractive index of the external medium. In terms of r and t, the reflectivity and transmissivity are:

$$\mathcal{R} = |r|^2 \quad (\text{A.40})$$

$$\mathcal{T} = |t|^2 \quad (\text{A.41})$$

The phases δ_r and δ_t are respectively the phase change in reflection and the phase change in transmission. They are expressed as:

$$\delta_r = \tan(\arg r) \quad (\text{A.42})$$

$$\delta_t = \tan(\arg t) \quad (\text{A.43})$$

Appendix B

Emission characteristics of lasers operating at 1.55 μm and 1.53 μm

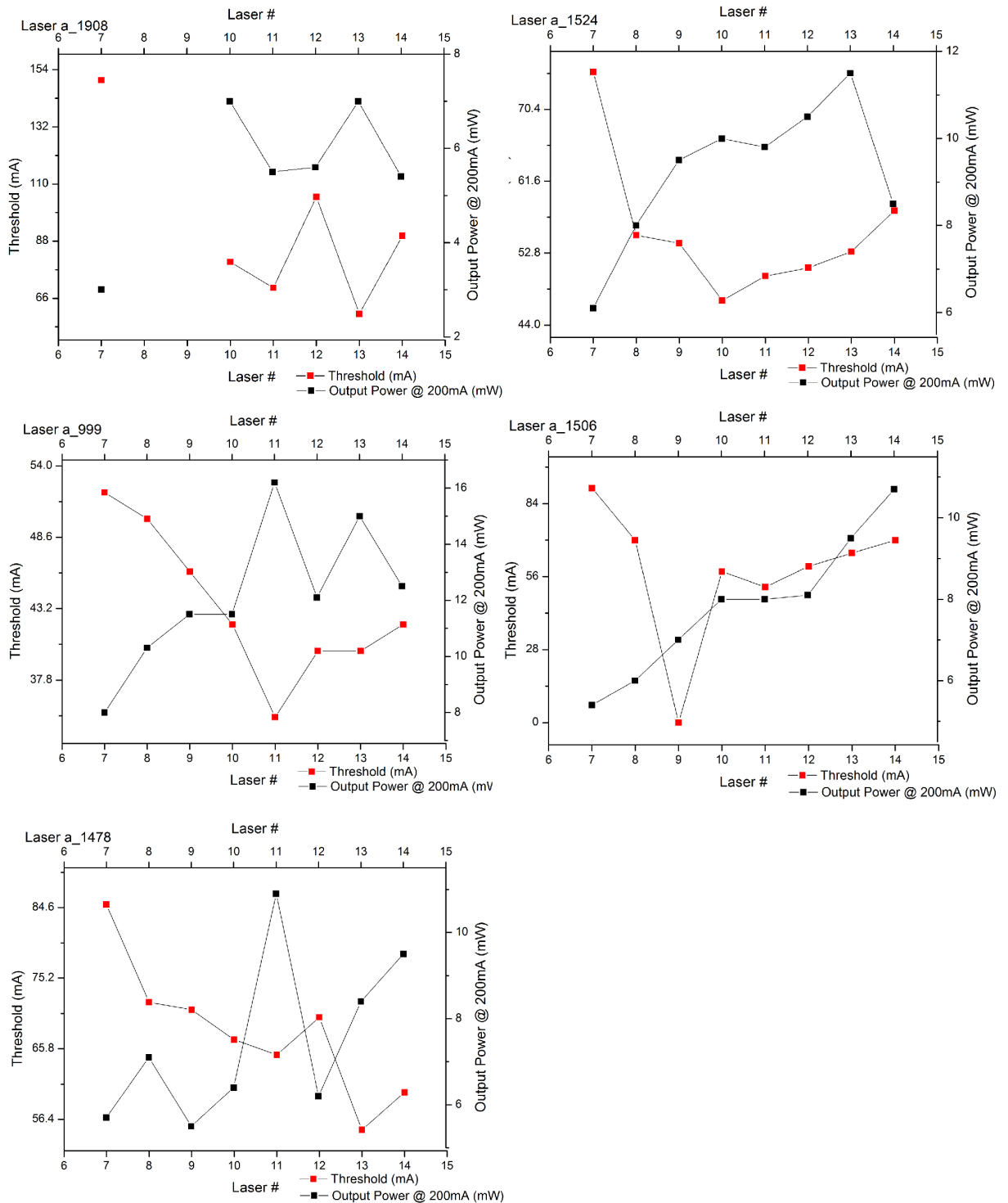


Fig. B.1. Threshold current and output power at 200mA of complex-coupled DFB lasers designed to operate at 1.53 microns versus the nominal gratings phase shift.

APPENDIX B. EMISSION CHARACTERISTICS OF LASERS OPERATING AT 1.55 μ M AND 1.53 μ M

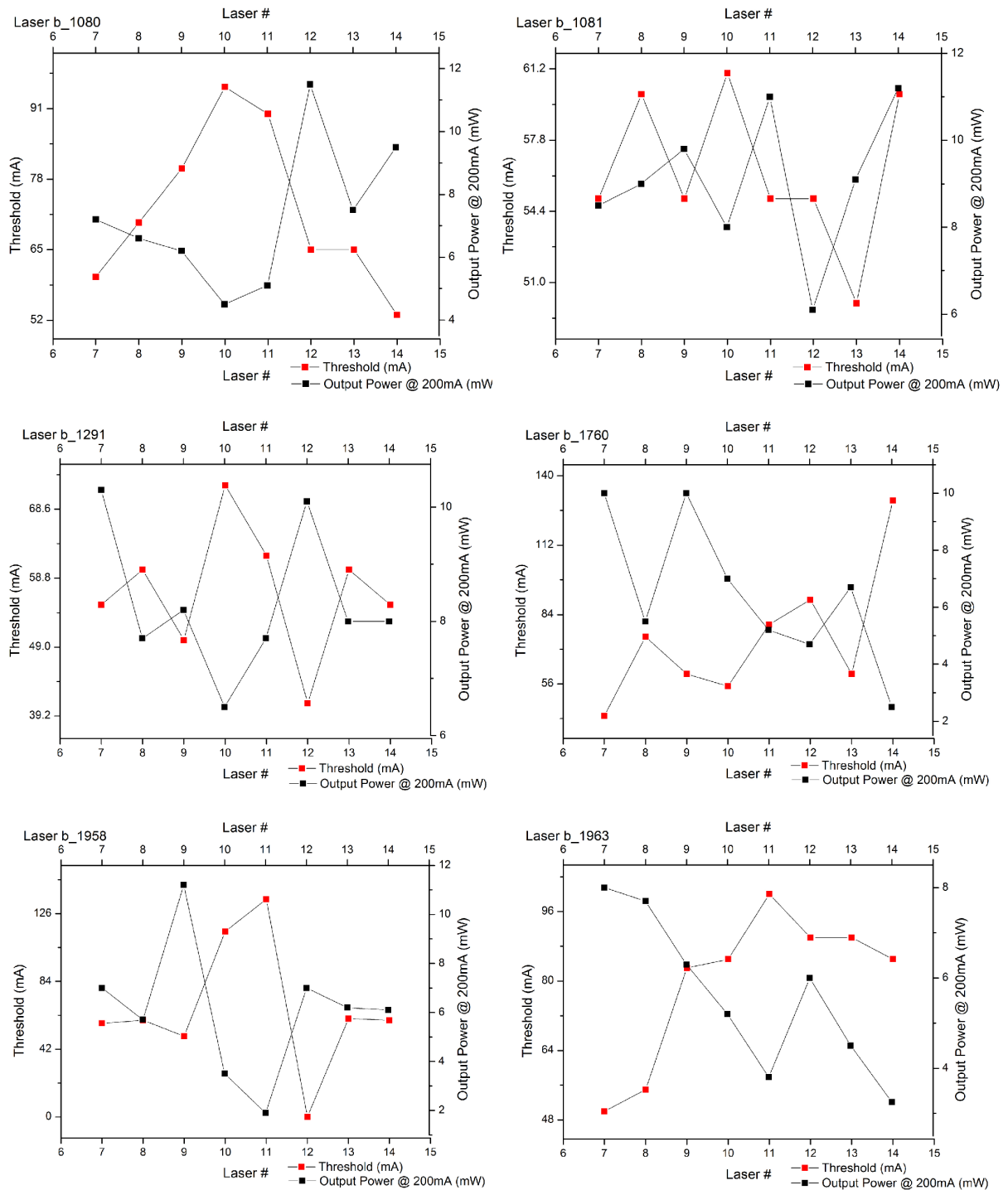


Fig. B.2. Threshold current and output power at 200mA of complex-coupled DFB lasers designed to operate at 1.55 microns versus the nominal gratings phase shift.

Appendix C

Résumé long en français

Ce manuscrit de thèse décrit mon travail, effectué de 2015 à 2018 au sein des groupes CRIME et PHODEV, du département photonique du Centre de Nanosciences et de Nanotechnologie (C2N). Durant cette période, j'ai travaillé à la conception, fabrication ainsi qu'à l'étude de lasers à rétroaction distribuée (appelés aussi lasers DFB) par un couplage complexe (CC). Du fait de contraintes de fabrications, ces lasers ont été conçus pour fonctionner au troisième ordre et pour quatre longueurs d'onde différentes dont la fenêtre est centrée autour de $1.55\mu\text{m}$. La modulation de la partie réelle de l'indice est apportée par la structuration en corrugations du guide d'onde des lasers, et la modulation de la partie imaginaire est apportée par un réseau métallique absorbant.

Les indices effectifs, permettant le calcul de la période de Bragg, ont été déterminés par une méthode modale. Le comportement des modes dans la cavité a été étudié grâce à la méthode matricielle dite d'Ables, reposant sur une succession de couches modulant les parties réelle et imaginaire de l'indice du matériau. Les conséquences du déphasage entre les deux composantes de l'indice, lié au déphasage des deux réseaux mentionnés plus haut, ont été particulièrement étudiées à cette occasion. Les résultats montrent une asymétrie dans la réponse du réseau à couplage complexe dès lors que les deux réseaux de perte et d'indice ne sont ni en phase ni hors phase. Le cas particulier d'un déphasage de $\pi/2$ entre ces deux réseaux démontre une asymétrie maximale voire même une amplification unidirectionnelle cohérente en réflexion en l'absence de réflexion aux facettes. Ce cas très intéressant de symétrie Parité-Temps (PT) étant très compliqué à obtenir, je me suis focalisé sur la réalisation de lasers à couplage complexe les plus performants possibles. Pour cette raison, il fût décidé de travailler avec un minimum de pertes et des facettes clivées. Les lasers produits ont alors une amplitude de modulation d'indice réelle plus élevée que pour la partie imaginaire.

Des séries de 8 lasers DFB à couplage complexe ont été fabriquées, différenciées par un incrément de phase de $1/8$ de période entre deux lasers consécutifs. Cet incrément de phase permet de s'affranchir en partie des contraintes de fabrication, ainsi que d'étudier l'influence de la phase relative entre les réseaux sur les performances des lasers. Des lasers DFB à couplage par l'indice et à couplage par le gain ont été ajoutés au processus de fabrication, de façon à pouvoir extraire les caractéristiques des deux réseaux impliqués, ainsi que pour en comparer les performances.

Les lasers furent fabriqués au C2N, grâce aux techniques de fabrications classiques du domaine de la photonique intégrée, en particulier la lithographie par faisceaux d'électrons, la gravure sèche et la lithographie optique pour n'en citer que quelques-unes. La principale difficulté rencontrée lors de la fabrication a été le développement d'un processus

de gravure permettant d'obtenir un réseau d'indice à corrugation avec une géométrie contrôlée. En particulier, il a été difficile d'atteindre une faible rugosité de gravure, ainsi que des flancs de gravures verticaux à l'intérieur des corrugations rectangulaires, celles-ci ayant une ouverture réduite autour de 320nm. Deux recettes de gravure à base Chlorée ou de Bromure d'Hydrogène donnèrent de bons résultats. Pour des raisons de disponibilité de gaz, la gravure à base HBr a été utilisée pour la gravure des lasers étudiés ici.

Dans un premier temps, la caractéristique courant/puissance ainsi que le spectre optique des lasers fabriqués ont été mesurés. Les meilleurs résultats en terme de puissance et de courant de seuil sont obtenus pour des lasers DFB à réseau d'indice classiques, avec des courants de seuil compris entre 20mA et 25mA, et une puissance à 200mA supérieure à 15mW. Les lasers DFB troisième ordre à couplage par les pertes sont moins performants que leur équivalent fonctionnant au premier ordre, du fait de l'interaction du mode avec le réseau de pertes dans la cavité, qui accroît les pertes lorsqu'il est au 3ème ordre. Une part significative des lasers DFB 3ème ordre à réseau de pertes ne montrent pas de régime laser, et ne purent donc pas être mesurés plus en profondeur. De façon intéressante, en dépit d'une forte absorption par le réseau métallique, les lasers DFB 3ème ordre à couplage complexe ont des performances courant/puissance similaires aux lasers DFB 1er ordre à couplage par les pertes, avec des courants de seuil de l'ordre de 50mA à 70mA, et une puissance à 200mA variant de 7mW à 12mW. L'évolution des caractéristiques courant/puissance laisse penser que les performances des lasers sont corrélées à la phase relative entre les réseaux. Cette observation se justifie par l'émergence de lasers ayant un seuil plus faible et une puissance plus élevée à courant égal. De plus, l'évolution des performances de ces lasers en fonction du déphasage nominal entre les réseaux semble se faire suivant un motif précis. Ce motif est semblable à celui suivi par le recouvrement des réseaux d'indice et de pertes, lui-même corrélé à l'absorption du mode.

Le spectre des lasers fut mesuré sous courant continu, pour des courants variant de 20mA à 250mA et au-delà. Les lasers DFB 1er ordre à couplage par les pertes et 3ème ordre à couplage complexe ont un fonctionnement monomode robuste, restant monomode au-delà de 250mA, avec un taux de réjection des modes secondaires supérieur à 50dB. La phase relative nominale semble également jouer un rôle sur les performances spectrales, puisqu'un motif est également visible au sein de la population des lasers à couplage complexe. Les lasers à couplage par l'indice, bien que monomodes, résistent moins bien à des courants plus élevés et deviennent multimodes pour des courants d'injection dépassant 150mA.

Ce premier travail a permis de démontrer que la combinaison d'un réseau à couplage par l'indice et d'un réseau à couplage par les pertes améliore la caractéristique courant/puissance par rapport aux lasers à couplage par les pertes seul, ainsi qu'un fonctionnement monomode à des courants d'injection plus élevés.

Dans un second temps, les lasers ont été sondés par un laser accordable externe, pour extraire les profils de transmission et réflexion des différents types de cavité. Les pertes des différentes cavités ont ainsi été mesurées à partir de ces mesures sous le seuil. La variation de la partie imaginaire de l'indice Δn_{Im} a été évaluée à partir de la mesure de pertes établie pour les lasers DFB 1er ordre à couplage par les pertes. La variation de la partie réelle de l'indice Δn_{Re} a quant à elle été déterminée en confrontant les mesures de la largeur de stop-band les résultats obtenus par simulation. Les résultats obtenus pour chacune de ces amplitudes de modulation diffèrent d'un ordre de grandeur, avec respectivement $2 \cdot 10^{-3}$ et $2 \cdot 10^{-4}$ pour Δn_{Re} et Δn_{Im} . Utilisant ce protocole expérimental,

il a également été possible de comparer les spectres d'amplification de chacun des lasers dans les deux directions de propagation. Malheureusement, les résultats n'ont pas permis de mettre en évidence un phénomène important d'amplification unidirectionnelle en réflexion, signature de la symétrie PT. Plus exactement, ce phénomène d'amplification en réflexion a pu être observé dans les populations de lasers DFB à couplage par les pertes et à couplage complexe en proportions égales. Il est donc possible que le couplage par les pertes, cas particulier de symétrie PT, puisse engendrer cette amplification unidirectionnelle en réflexion. Il est possible également que les réflexions et phases aux facettes interfèrent dans la mesure.

Un des avantages de la symétrie PT appliquée aux laser DFB est le profil de pertes asymétrique vue par deux ondes contra-propagatives. Ce principe représente un outil puissant permettant d'atténuer l'impact dévastateur que peut avoir le retour optique dans la cavité laser, cause d'une dégradation importante de la cohérence et de la stabilité du laser. Les résistances au retour optique des lasers à couplage par l'indice, par les pertes et à couplage complexe ont été évaluées dans chacune des directions de propagation, suivant le critère de l'effondrement de la cohérence. Les meilleurs résultats sont obtenus pour les lasers à couplage par l'indice, avec une résistance au retour optique supérieur à celle édictée dans la norme IEEE établie à -21dB de taux de retour optique. Les lasers à couplage complexe n'ont donc pas permis d'obtenir une amélioration de la résistance au retour optique de nos lasers DFB. En revanche, une évolution est visible dans la résistance au feedback des lasers à couplage complexe en fonction de la phase relative nominale existant entre leurs deux réseaux. Cette différence s'établit tant en terme de performance qu'en terme de dissymétrie. Certains lasers présentent une résistance au retour optique accrue dans une direction. Toutefois, cette dissymétrie dans la résistance au retour optique est également visible pour des lasers DFB à couplage par l'indice, laissant également penser à un effet de phase aux facettes.

Les perspectives à venir de ce travail consistent principalement à étudier des lasers à couplage complexe similaires fonctionnant au premier ordre. Les simulations montrent en effet que les résultats attendus au premier ordre permettent une meilleure discrimination de mode que ceux du 3ème ordre. De ce fait, le principal défi reste technologique, et repose principalement sur la gravure d'un réseau d'indice à période encore plus courte. Pour réduire cette contrainte, le réseau 3ème ordre peut être conservé et associé à un réseau métallique qui lui serait conçu au 1er ordre. Le problème de la phase aux facettes doit être également traité. Une première étape pourrait consister en un traitement spécifique des facettes.

Titre : Application du concept de symétrie Parité-Temps à l'optique intégrée.

Mots clés : Nanophotonique, photonique, nanotechnologies, optique intégrée, symétrie Parité-Temps, lasers DFB

Résumé : Le développement des systèmes photoniques au cours des dernières décennies, rendu possible par l'évolution des technologies de nanofabrication, a vu l'apparition de nouveaux matériaux synthétiques tels que les cristaux photoniques, les métamatériaux, les plasmons de surface, et plus récemment les structures dites « à symétrie Parité-Temps ». La caractéristique de ces derniers matériaux synthétiques est que bien qu'ils soient décrits par un Hamiltonien non-Hermitien, leurs valeurs propres peuvent toutefois être réelles. En optique plusieurs phénomènes physiques sont connus pour la ressemblance des équations les décrivant, avec l'expression de ce type d'Hamiltonien en mécanique quantique. C'est le cas des équations de modes couplés dans les lasers DFB.

Ce travail de thèse a porté sur la conception, fabrication et étude de lasers DFB à couplage complexe, dans l'optique d'appliquer le principe de symétrie Parité Temps (PT) à un composant fonctionnel. Ces lasers sont combinent un réseau par l'indice et par les pertes, avec un déphasage spécifique. La simulation des modes dans la cavité, effectuée par méthode matricielle de Ables, a dévoilé l'avantageux filtrage apporté par les lasers DFB à couplage complexe, en gardant un seuil faible. Le cas spécifique d'un déphasage d'un quart de période entre les deux réseaux, correspondant à une condition de symétrie PT, induit des effets unidirectionnels d'amplification en réflexion.

Des lasers DFB à couplage par l'indice, par les pertes et à couplage complexe avec différentes phases entre les réseaux ont été fabriqués selon les techniques courantes de réalisation de circuits photonique intégrés : lithographie électronique et gravure ICP notamment.

Les mesures de caractéristiques courant /puissance montrent une diminution du courant de seuil des lasers à couplage complexe en comparaison de leur équivalent à couplage par les pertes, et un comportement monomode plus robuste et plus systématique en comparaison de leur équivalent à couplage par l'indice.

Les variations d'indice réelle et imaginaire dans les cavités ont été mesurés à l'aide d'un laser externe.

La résistance au retour optique de nos lasers a également été étudiée. Les résultats montrent une corrélation entre la tolérance au retour optique et le déphasage des réseaux d'indice et de pertes, sans montrer d'amélioration significative de cette résistance par rapport aux lasers DFB à couplage par l'indice.

Ce premier « véhicule test » sur l'application de la symétrie PT aux lasers à contre réaction répartie a permis d'obtenir des perspectives encourageantes quant à l'amélioration des performances des technologies existantes. Ce travail conforte l'intérêt de ce concept pour la conception de lasers DFB tolérant au feedback et leur intégration dans un système laser-modulateur fonctionnant sur la même base.

Title : Application of the concept of Parity-Time symmetry to integrated optics.

Keywords : Nanophotonics, photonics, nanotechnology, integrated optics, parity-Time symmetry, DFB lasers.

Abstract : The development of photonics during the past decades, enabled by the advent of nanofabrication technologies, witnessed the appearance of new types of artificial materials such as photonic crystals, metamaterials, plasmonic circuits, and more recently the so called "PT symmetry" structures. The characteristic feature of this new type of artificial structures is that though they are described by non-Hermitian Hamiltonians their eigenvalues can still be real. In optics, several physical phenomena are known to obey equations that are formally equivalent to that of Hamiltonians in quantum mechanics. During this work, we investigated the design, fabrication and characterization of complex-coupled DFB lasers, with the intent to apply Parity-Time (PT) symmetry to a practical device. The mode selectivity inside the cavity is brought by the combination of a gain-coupled and index-coupled Bragg grating, under the form of respectively a corrugated waveguide and a metallic absorbing surface grating.

Through the simulation of the mode evolution inside conventional DFB lasers and complexe-coupled DFB lasers using Ables matrix method, the advantages of efficient mode filtering while keeping a low threshold current was observed. The specific phase shift of a quarter period, matching the PT-symmetric configuration, is found to show highly asymmetric mode selection, with unidirectional amplification in reflection.

Index, gain and complex-coupled DFB lasers with different phase shifts between loss and index grating profiles were fabricated, using photonics integrated circuits fabrication building blocks: electron beam lithography and induced coupled plasma dry etching to name but a few.

The characterization of the fabricated lasers shows a reduction in threshold compared to equivalent third order gain-coupled DFB lasers, and improved monomode operation and yield compared to third order index-coupled DFB lasers.

Real and imaginary parts of the index modulation as well as reflection spectral response was investigated by external optical probing of the laser cavities.

The resistance of the CC DFB lasers to external optical feedback was studied. If results show an apparent correlation between the gratings phase shift and the feedback resistance, but no significant improvement was found with regards to IC DFB lasers.

This first milestone on the application of PT-symmetry to the design and fabrication of DFB lasers provide interesting prospects on the improvement of existing technologies. This work reinforces the interest of this concept for the design of feedback tolerant DFB lasers, and their integration in an all PT-symmetric laser-modulator system.

